Forschungszentrum Jülich
in der Helmholtz-Gemeinschaft

Institut für Plasmaphysik

Mitigation of disruptions in a tokamak by means of large gas injection

Alexei Savtchkov

Jül-4122

Mitigation of disruptions in a tokamak by means of large gas injection

Alexei Savtchkov

Berichte des Forschungszentrums Jülich ; 4122
ISSN 0944-2952
Institut für Plasmaphysik Jül-4122
D 61 (Diss., Düsseldorf, Univ., 2004)

Zu beziehen durch: Forschungszentrum Jülich GmbH · Zentralbibliothek
D-52425 Jülich · Bundesrepublik Deutschland
☎ 02461 61-5220 · Telefax: 02461 61-6103 · e-mail: zb-publikation@fz-juelich.de

A.Savtchkov

"Mitigation of major disruptions in a tokamak by means of a gas injection"

ABSTRACT

In a tokamak, the poloidal magnetic field provided by the toroidal plasma current forms an essential part of the magnetic field confining the plasma. However, instabilities of the magnetohydrodynamic equilibrium can lead to an uncontrolled sudden loss of the plasma current and energy, which is called a disruption.

During disruptions the plasma energy is typically deposited on the vessel walls within 0.1 ms resulting in high heat loads and possible melting or evaporating of in-vessel components. The interaction of halo currents caused by displacements of the plasma column with the magnetic field results in $j \times B$-forces which can lead to structural damages. The increased loop voltage can give rise to the appearance of multi-MeV electron beams, so-called runaway electrons, which cause local damage when hitting the vessel wall.

In order to avoid these detrimental consequences, disruption mitigation is an essential part of tokamak research. In these thesis, mitigation of disruptions by a fast gas injection is investigated. A special gas valve has been developed by us with one of the fastest reaction times available (0.5 – 1 ms at $p = 1$ – 30 bar). In contrast to other valves, it contains no ferromagnetic materials and can be operated in the full magnetic field close to the plasma. If a sufficient amount of gas is injected into the tokamak discharge prior to an uncontrolled disruption, a substantial amount of the thermal plasma energy is radiated, resulting in a more uniform distribution of the power density over the vessel walls, minimizing possible excessive localized heat loads. The use of non-reactive gases for mitigation ensures their fast removal from the vessel after the termination of a tokamak discharge. A series of experiments on the tokamak ASDEX Upgrade with different amounts and kinds of gases shows a reduction of the plasma current decay time and a suppression of halo currents.

To study the basic physical processes of a disruption, a one-dimensional numerical model of particle and energy transport has been developed. Calculations for neon show that a fast penetration of the neutral gas can occur owing to the cooling of the plasma at the front of the neutral particle cloud. Assuming a large inward transport of the injected impurity of the order of 100 m^2/s, the radiated energy becomes equal to the thermal plasma energy prior to the disruption. After the thermal collapse, the plasma reaches an equilibrium temperature of several eV as a balance between ohmic heating, radiation and heat conduction losses.

Contents

1 INTRODUCTION

Nuclear fusion is considered a potential energy source for the growing needs of the world population [1, 2, 3]. The most promising reaction for fusion energy production is the fusion of deuterium and tritium:

$$ {}^{2}_{1}D + {}^{3}_{1}T = {}^{4}_{2}He(3.5MeV) + {}^{1}_{0}n(14.1MeV), $$

where the mass deficit of the reaction products is transformed into energy (numbers in brackets). To start the reaction it is necessary that both atoms approach each other close enough such that the nuclear attractive forces dominate over the Coulomb repulsion. For a positive power balance of an electricity producing reactor, a minimum value of the product 'plasma density×plasma confinement time' must be exceeded. Two methods for the realization of fusion are pursued on large experimental facilities world wide. One is based on the fast compression of a DT pellet by high power lasers or heavy ion beams, which leads to a significant increase of the density of the reacting particles. Confinement is provided by the natural inertia of the fuel mass. In the second method, a magnetic field is used to confine the fuel at moderate densities of about $10^{20}\ m^{-3}$ and at temperatures of about 100 Million $°C$ (about 10 keV).

1.1 The tokamak — a tool for nuclear fusion

Two main magnetic confinement concepts which have proved successful are the stellarator and the tokamak. Both generate a magnetohydrodynamic (MHD) equilibrium by superimposing poloidal and toroidal magnetic fields in a toroidal configuration. In stellarators, the required magnetic fields are produced by external field coils only.

In a tokamak, the toroidal magnetic field is generated by external coils and has a typical value of several (2 – 5) Tesla. A plasma current induced by the flux swing in the central solenoid flows in the toroidal direction and produces the poloidal magnetic field B_θ (Fig.1). Due to the toroidal geometry, the magnetic pressure is higher at smaller major radii than at larger ones. Additionally, the current in a torus is oriented such that a repulsive force exists on the circumference. To correct this, a vertical component of a magnetic field is required, which is produced by external coils. By the superposition of the two fields, an equilibrium state can be reached.

The plasma current in a tokamak is induced inductively, like in a usual transformer, with the plasma loop serving as a secondary winding. This, however, makes it difficult to obtain long pulses due to the limited value of magnetic flux in the transformer yoke. So, non-inductive methods of current drive have to be applied later in a fusion reactor.

The poloidal component B_θ is normally of the order of one tenth of the toroidal field, and the slope of the magnetic lines in Fig.1 is strongly exaggerated. The superposition

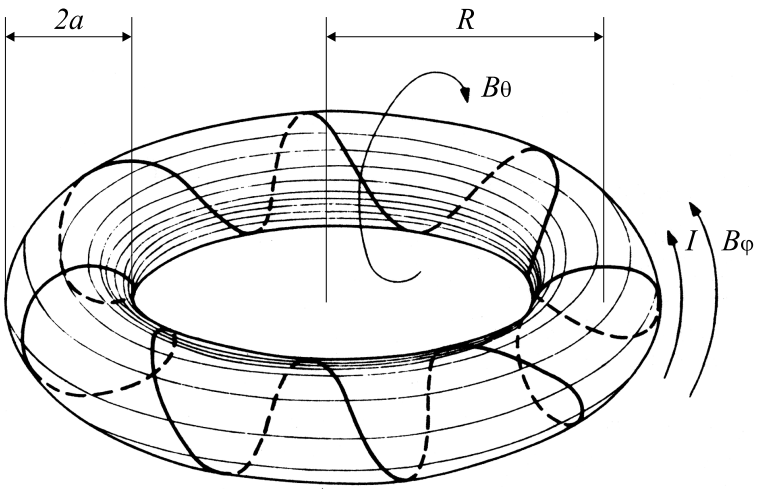

Figure 1: *Helical structure of the magnetic field in a tokamak. Depicted are: a — minor radius, R — major radius, B_θ — poloidal field, B_ϕ — toroidal field, I — plasma current. The picture is reproduced from [4], one of the pioneer works on tokamaks.*

of B_ϕ and B_θ forms a set of nested magnetic flux surfaces. A characteristic value of such a surface is the safety factor q describing the pitch angle of the resulting magnetic field line on the surface. In the cylindrical approximation ($R \gg a$) it can be written as

$$q(r) = \frac{rB_\phi}{RB_\theta}, \tag{1}$$

giving the number of toroidal turns of a magnetic line on a chosen surface (and, therefore, it is a function of radius) needed for a poloidal turn. Early tokamaks had a circular cross-section while nowadays plasmas elongated in the vertical direction are produced, allowing better performance.

Different techniques may be applied to heat a plasma, once it is confined. Natural ohmic heating is always present, though its efficiency decreases with increasing temperature because of the drop in plasma resistivity. RF-methods (electron cyclotron resonance heating, ECRH, and ion cyclotron resonance heating, ICRH) and injection of energetic neutral beams (NBI) are conventional ways of plasma heating. A characteristic value of how effective the magnetic field confines plasma at a given temperature is the parameter β which is the ratio of the plasma kinetic pressure to the pressure of the total magnetic field:

$$\beta = \frac{p}{B^2/2\mu_0}, \; B^2 = B_\phi^2 + B_\theta^2. \tag{2}$$

1.2 Problem of disruptions

A disruption is an abrupt termination of a tokamak discharge in which the magnetic and thermal energies stored in the plasma are rapidly lost [5]. Such events are highly unde-

sirable. Firstly, they limit the stable operation of a machine. Secondly, the consequences of disruptions may be dangerous for a tokamak because all stored energy is deposited immediately on the walls creating enormous heat fluxes. During the phase of the plasma current decay currents are induced in the vessel and in-vessel components. Strong $j \times B$-forces associated with them stress the vessel and may cause a deformation or breakage of the internal components. Also the acceleration of electrons to energies of several tens of MeV (runaway electrons) is possible, which may damage the wall.

Not every tokamak suffers from disruptions in the same way. The situation becomes more delicate with increasing machine size [6, 7]. Estimations of the incident energy loading made for the next step device ITER (International Thermonuclear Experimental Reactor) [7] show that the loading on the divertor targets should be expected to exceed 10 GW/m^2 causing significant melting and/or sublimation of the plasma-wetted surfaces. Up to $\sim$ 70% of the initial plasma current is predicted for ITER to be taken over by runaway electrons by the avalanche mechanism [8]. That is why the problem of disruptions becomes of growing importance and special techniques for mitigating disruptions in a tokamak have to be worked out.

1.3 Techniques of mitigation of disruptions

A technique of mitigation of disruptions must provide:
– a quick termination of the plasma current,
– a distribution of the stored magnetic and thermal plasma energy over a large area to avoid peak heat loads,
– a minimization of the halo currents and a reduction of the mechanical stresses of the vessel and in-vessel mountings,
– avoidance of generation of runaway electrons,
– conditions for the reliable start of subsequent discharges.
This can be realized by a fast and heavy injection of an impurity. Due to the injection the plasma cools quickly due to the distribution of the thermal energy over the increased number of particles in the plasma (thermal dilution), due to ionization of the impurity and due to enhanced impurity line radiation. In contrast to conducted/convected energy the radiation is distributed over a large surface. Due to the high resistivity of the impurity contaminated plasma the discharge current decays rapidly. The use of a non-reactive noble gas allows one to pump it out easily after the puff. Three types of impurity injection have been considered.

– *Solid state pellet injection ("killer pellet").* Killer pellet is an efficient tool in terminating a plasma discharge and it possesses the advantage of a deep penetration into a plasma. In order to obtain a sufficient ablation rate, a minimum plasma

temperature is required. Therefore a pellet works efficiently only before the collapse of the plasma thermal energy. For the production of pellets frozen from gases (D_2, Ne, Ar) a complicated technical equipment is needed. In addition, high runaway currents are observed with pellets due to reasons which will be discussed later.

– *Liquid jets.* An injection of jets of liquid deuterium, also capable of penetrating the plasma core, is proposed for ITER to overcome problems with runaway production.

– *Gas injection ("killer gas").* Along with killer pellets it presents a simple and effective technique of for disruptions mitigation. It can be performed under any plasma condition and is more flexible in choosing an appropriate amount and kind of the impurity species. Given enough gas pressure, the plasma center is reachable for impurities. In addition, injecting gas represents a simpler technical task.

1.4 Scope of this work

The investigation of disruption mitigation based on killer gas injection is the subject chosen for this work. A special fast valve with a high gas throughput [9, 10] was designed by us and used for this goal. To our knowledge, this valve has worldwide the fastest response time from a trigger signal to the start of the opening (0.5 ms) and to the full open state (1 ms). It can release gas from a reservoir at pressures of 1 – 30 bar. An important feature of the valve is that it is built without ferromagnetic materials and is not affected by magnetic fields. This feature allows one to install the valve with a minimal separation from the vacuum vessel, which results in a faster reaction time. Because the TEXTOR tokamak in Jülich was shut down, we brought the valve to the ASDEX Upgrade tokamak in Garching. There it was mounted and taken into operation. After optimizing the gas injection parameters, the valve was applied both to study induced disruptions in "normal" discharges and later in a feedback loop in discharges with a strong MHD activity which were on the way to disrupt.

In order to describe the development of a disruption following a large gas puff, a new time dependent 1-D transport model was developed. Previous simulations are either fully 0-dimensional [11, 12], or quasi 1-dimensional, with the calculation being carried out only at a given (fixed) radius [13]. Compared to this the modeling performed in this work is improved by treating both the particle and heat transport. The inclusion of the radial transport is important for the explanation of the thermal collapse in the plasma center.

The model shows the importance of impurity radiation for the explanation of the rapid energy quench both for naturally developing disruptions and for disruptions provoked by a gas injection. If the outward heat conduction is the only energy sink, the electron temperature remains at around 300 eV at the end of the energy quench, in contradiction

to the observations.

The structure of the thesis is as follows. In the next section the characteristics of disruptions are introduced in detail. In section 3, an overview of existing experiments dealing with the same topic is given. In section 4, the design and characteristics of the fast gas valve are described. It is then followed in section 5 by the description of the experiments with the gas valve on ASDEX Upgrade. Motivation, scheme of the experiments, main results and their interpretation are given. In section 6, the 1-D numerical simulation of a disruption provoked by a gas injection is presented. The set of basic equations used in the model, solution method, tests and results of the code's runs as well as a discussion of the output of the modeling are given. Conclusions and plans for the future work are described in section 6.

2 CHARACTERISTICS OF DISRUPTIONS

2.1 MHD instabilities and modes

Disruptions occur due to MHD instabilities. The basic MHD instabilities in a tokamak can be driven by plasma current gradients or plasma pressure gradients [2]. If a plasma is supposed to be ideally conducting one speaks about an *ideal* instability. A *resistive* instability can occur assuming a finite resistivity of the plasma.

Instabilities lead to a perturbation of values (temperature, density, potential, magnetic field, ...) which can be described by an infinite spectrum of possible modes. In the case of a circular, large aspect-ratio ($R \gg a$) tokamak the modes take the form $e^{i(m\theta - n\phi)}$, where θ, ϕ are the poloidal and toroidal angles, respectively. The numbers m and n are the mode numbers. In a tokamak, modes with a rational m/n are resonant to the equilibrium magnetic field at the radial positions where the safety factor has the value $q = m/n$. Due to the perturbation the original structure of the magnetic field is changed such that *magnetic islands* are produced. The contour plot of the surfaces of constant magnetic flux in Fig.2 shows an example of a $m = 2$ island in the poloidal cross-section of a tokamak. Islands appear at different radial locations (in particular $q = 3/2,\ 2,\ 3$). They may grow,

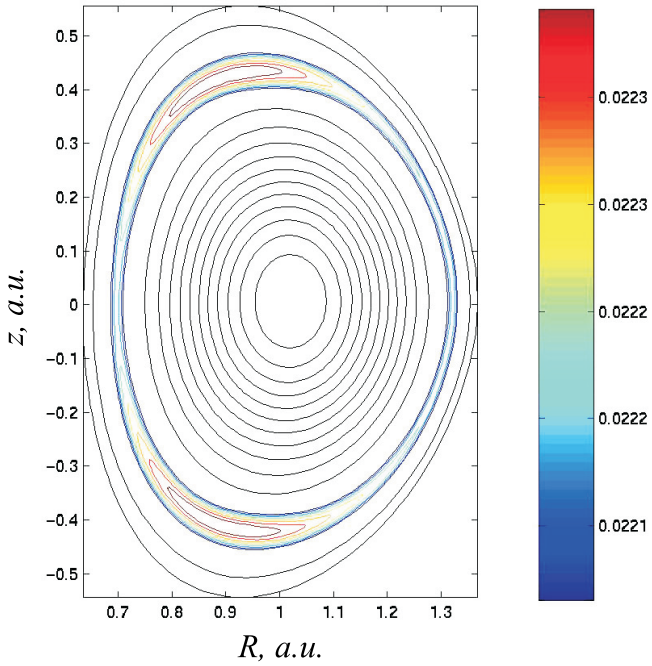

Figure 2: *The contour plot of the surfaces of constant magnetic flux in the poloidal cross-section of a tokamak [14]. Due to a perturbation of the magnetic field an $m = 2$ island appears.*

overlap and interact with each other. Magnetic field lines do not lie on a surface but follow a space filling trajectory. This changes the confinement properties of the magnetic

field and leads to enhanced energy and particle transport. When the disturbance becomes too large a disruption occurs.

2.2 Causes of instabilities leading to disruptions

Plasma current-driven instabilities and plasma pressure-driven instabilities can lead to several types of disruptions in a tokamak: low-q disruptions, density limit disruptions, β-limits, vertical displacement events (VDE's) and disruptions due to mode locking. Low-q disruptions occur when q at the plasma edge, q_a, approaches the value of 2 [15]. A large current density gradient inside the $q = 2$ surface is thought to destabilize the $m/n = 2/1$ mode. The interaction with the cold outer plasma leads to a rapid fall in electron temperature and the consequent loss of plasma current. Sometimes other minor disruptions, from which the plasma usually recovers, are observed when q_a passes through other integer values, in particular $q_a = 3$.

The density limit disruption is one of the most important disruption types for the context of these thesis. When the plasma density n rises, the power radiated from the plasma edge increases proportional to n^2 which leads to enhanced cooling of the edge, to a shrinking of the plasma current cross-section and to a peaking of the current density profile. The increased current density gradient at the $q_a = 2$ surface destabilizes the $m/n = 2/1$ mode. The development of MHD modes and growth of magnetic islands results in the enhanced radial diffusion of the plasma current. The current density profile undergoes some degree of flattening expulsing the poloidal magnetic flux from the plasma [40]. At this time a negative spike is observed in the loop voltage which increases the plasma current to conserve the magnetic flux.

VDE is the second important disruption type which will be often referred to in the thesis. It takes place only in elongated plasmas. Such plasmas are produced by a set of shaping coils elongating the plasma in the vertical direction to obtain a higher plasma current at a given q_a. A point exists where all vertical forces acting on the plasma column are balanced (*neutral* point) and the plasma is kept at this point by a feedback control. A VDE occurs when the vertical plasma positioning is lost. In this case the plasma column moves rapidly as a whole in the vertical direction, either up- or downwards [16]. Almost every disruption in an elongated plasma ends with a VDE. Failure in a position control can also initiate it. Then the $q = 2$ surface moves together with the plasma column to the edge, leading to the low-q disruption described above.

The β-limit is caused by a high local pressure gradient giving rise to a growth of kink and ballooning modes [17]. If at the same time the value of q_a is low (≤ 3), a major disruption occurs. Otherwise, the β-limit manifests itself as a deterioration of energy and particle confinement which does not lead to the current quench. Experimentally it is

observed that β is limited to $\beta < \beta_N I_p/aB_\phi$ (β is in percent, plasma current I_p is in MA, minor plasma radius a is in m, toroidal field B_ϕ is in T). β_N is a characteristic feature of a tokamak and amounts to 6.5 on DIII-D, although values of 2.8 – 4 are more normal.

Locked mode disruptions happen when a plasma has magnetic perturbations initially, for example because of a not optimal current ramp-up. The mode induces image currents in the vessel wall which decrease the mode torque by $j_w \times \tilde{B}$-force, where j_w is the image current in the wall and $\tilde{B}$ is the magnetic field of the mode. If, in addition, small errors in the symmetry of the magnetic field of a tokamak (error fields) are present, the interaction of the perturbation with the error fields can lead to an additional mode slowing down in a similar way. In this case a $j \times B$-force acts between the correspondent component of the perturbation current and the error field. It is observed that if a mode stops rotating (that is locks to the wall), it results in a destruction of the equilibrium magnetic configuration and a disruption.

2.3 Time structure of a disruption

The process of a disruption can be divided into three time stages. As an illustration, an overview of several signals during a density limit disruption in TEXTOR is shown in Fig.3. At the first step, events preceding a coming disruption (called *precursors*) occur. This may be a development of various MHD modes producing, in particular, $m/n = 1/1$, $3/2$ and $2/1$ islands. Precursors are well visible as oscillations of the poloidal and radial magnetic field or electron temperature. Particle and energy transport along the field lines inside a magnetic island results in an almost constant plasma temperature across the island which differs from the bulk plasma temperature. Rotation of the island leads to the oscillations of the electron temperature seen in Fig.3 c) from $t \approx 0.585\ s$. Precursors may be absent for disruptions due to instabilities with a high growth rate, for instance, for vertical displacement instabilities. At some moment, when the mode amplitude becomes large, the second phase of a disruption begins and a rapid loss of the plasma's thermal energy happens (Fig.3 c) at $t \approx 0.684\ s$). This event is referred to as the *energy quench*. The energy quench happens in a very short time scale of some hundred microseconds. A model for the beginning of the energy quench assumes a nonlinear interaction between $m = 1$ and $m = 2$ modes which can lead to a destabilization of other modes in between, in particular the $m/n = 3/2$ mode. When the width of the islands becomes equal to the distance between them, the magnetic field lines begin to be stochastic destroying the magnetic flux surfaces. The main danger for a tokamak at this stage is that the whole thermal plasma energy is deposited within $\sim 100\ \mu s$ on the machine's walls, resulting in high heat loads, in particular in the case of a local heat deposition. The excessive heat loads may lead to melting or sputtering components inside the vessel. A peak in the

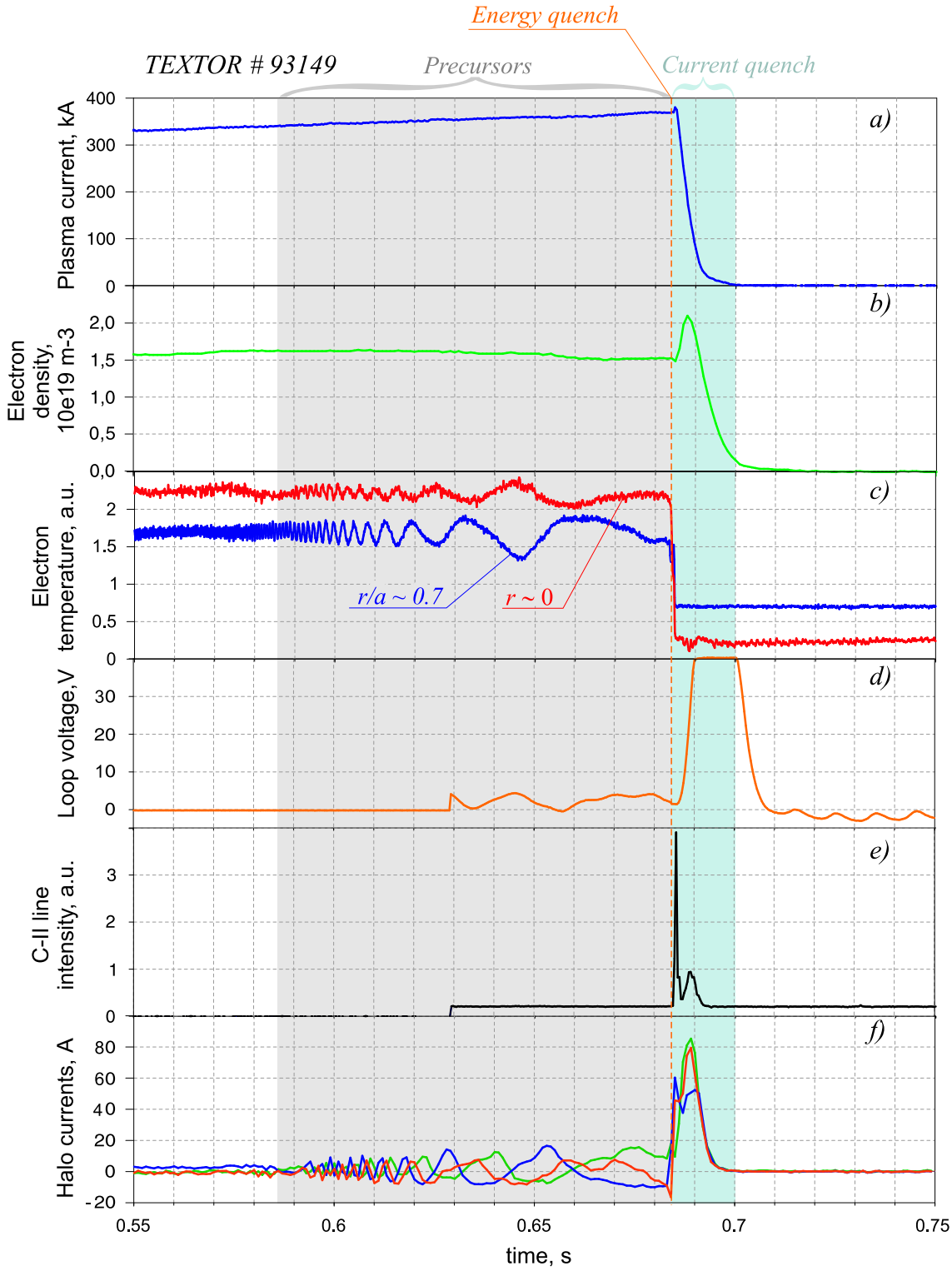

Figure 3: *An overview of a density limit disruption discharge in TEXTOR #93149.*

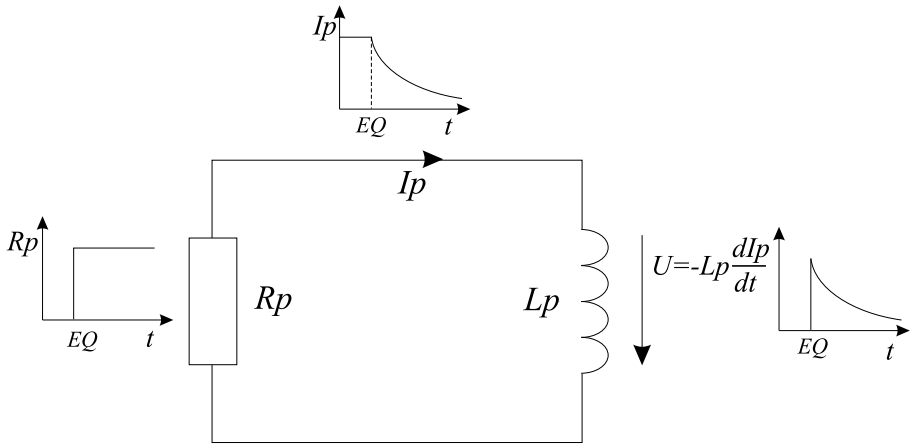

Figure 4: *An analogy between the decay of the plasma current after the energy quench (EQ) and the behaviour of the current in the equivalent R-L circuit.*

intensity of the *C-II* line on the upper side of the torus (Fig.3 e) indicates the appearance of carbon impurities in the plasma volume during the energy quench. Eroded particles are redeposited again such that the following discharges can also disrupt because of the release of the redeposited particles.

The third and the final stage of a disruption describes the decay of the plasma current (*current quench*), which lasts for 10 – 100 ms depending, in particular, on the impurity level. The decay of the plasma current in Fig.3 a) starts at $t \approx 0.684\ s$ with the current spike described above. This phase is characterized by a low-temperature plasma with a large amount of intrinsic impurities such as carbon or oxygen. The influx of these impurities occurs partially during the energy quench and partially during the current quench. The impurity content in a plasma is described by the effective plasma charge

$$Z_{eff} = \frac{\sum n_j j^2}{\sum n_j j}, \tag{3}$$

where the summation is performed over all impurity species including the main plasma ions. The plasma resistivity which is proportional to $Z_{eff} T_e^{-3/2}$ is strongly increased. As an example, a drop from a typical tokamak electron temperature of 1 keV to the post-energy quench value of the order of 10 eV causes to the increase of the resistivity by a factor of 1000. The decay of the plasma current can be described by the equivalent *R-L* circuit as it is shown in Fig.4 where R_p is the plasma resistance and L_p is the plasma inductance. After the energy quench marked in Fig.4 by "EQ" the resistanse R_p increases and the current starts to decrease. The reduction of the magnetic flux associated with the current through the inductance L_p drives the inductive voltage $U = -L_p \frac{dI_p}{dt}$. According to the Lenz rule, the voltage is induced such as to minimize the change of the magnetic flux. It drives a current in the same direction as the initial current I_p. In the case of the circuit in Fig.4 with the consant R_p and L_p, this results in an exponential decay of the

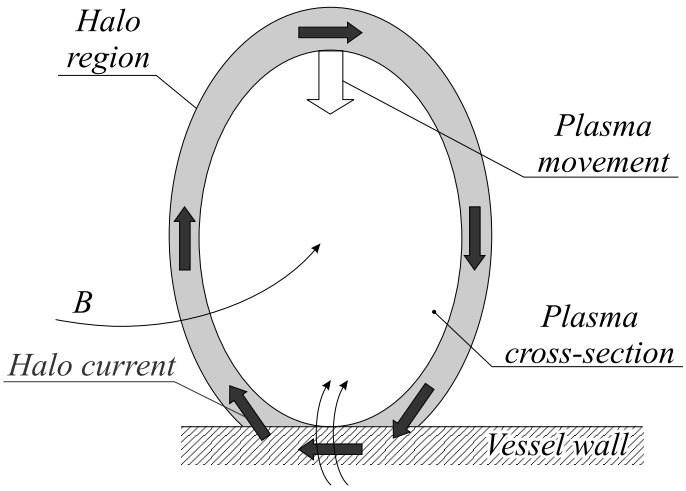

Figure 5: *Induction of a poloidal halo current by a change of the plasma cross-section as a result of the limitation of the plasma by the vessel's wall.*

current with the resistive time constant

$$\tau = \frac{L_p}{R_p}. \tag{4}$$

In the case of the plasma, R_p and L_p are not constant in time and the behaviour of the plasma current differs from the pure exponential one. However, the order of magnitude of the plasma current decay can be estimated from Eq.4.

During a disruption, the plasma column may be displaced from its original position. In the poloidal view given in Fig.5 the plasma moves towards the wall and the lower plasma edge is limited by the wall. The resulting change of the plasma cross-section decreases the flux of the toroidal magnetic field B enclosed by the plasma. Poloidal currents are induced which produce a toroidal field component (two black arrows in Fig.5) and try to compensate the change of the magnetic flux. Also toroidal currents are induced as the result of a change of the poloidal magnetic flux in a similar way. Full currents flow helically partially in the vessel and in-vessel structures and partially in the plasma outside the last closed magnetic surface and are called *halo currents*. In the vessel's wall the current path is not restricted by the direction of the magnetic field such that large $j \times B$-forces are generated. In Fig.3 f), halo currents measured at the plasma limiting surface are shown, reaching a peak during the current decay phase. An induction of halo currents is strongly undesirable, because wall elements experiences a large electromagnetic stress which may result in a mechanical damage or shaking of the vessel.

Besides the problems of high heat flows during the energy quench and an induction of halo currents in the current quench, there is one more serious problem. Due to a sudden increase of plasma resistivity after the energy quench a strong toroidal electric field may be generated. Normally the inductive voltage of one turn around the torus (*loop voltage*)

amounts to about 1 V. During a disruption, the loop voltage can exceed 100 V (Fig.3 d). The energy gained by electrons from the electric field is lost in Coulomb collisions between them. If the electric field is sufficiently high, an electron in the tail of the distribution function can receive more energy than the collisional drag can dissipate, and thus enters a regime of acceleration (*runaway electron*). Since the collisional cross-section drops with the electron energy, the process becomes unstable and beams of electrons of several MeV can be produced [19, 20]. Capable of a high penetration in the wall, they can cause erosion damage even behind the first shielding of the vacuum vessel.

3 STATUS OF THE EXPERIMENTS ON MITIGATION OF DISRUPTIONS

3.1 Mitigation of disruptions by a pellet injection

Injection of pellets presents a useful and valuable practice in plasma research. Pellets of various materials or compositions, as well as of different sizes, may be used depending on the purpose. They are taken, for instance, for fuelling or for diagnostic tasks. Utilization of pellets in experiments on disruption mitigation has been tried so far on ASDEX-Upgrade [21], DIII-D [22], JET [23], JT-60U [24], T-10 [25].

3.1.1 ASDEX-Upgrade

On the divertor tokamak ASDEX Upgrade in Garching, Germany, frozen neon pellets of the size of $1.65 \times 1.65 \times 1.75\ mm^3$ containing about $1.7 \cdot 10^{20}$ neon atoms at an injection speed of 560 m/s were successfully applied [21]. Large pellets and moderate speeds were chosen for the pellets to penetrate up to the plasma center.

In disruptions without impurity pellets it was observed that up to 100% of the plasma thermal energy could be deposited on the divertor plates. After the injection of a neon pellet a suppression of the energy flux onto the divertor was seen. Table 1 gives the energy balance for a natural disruption (discharge #5864), the disruption after the injection of a pellet into an ohmic plasma (discharge #5698), and the disruption after the injection of a pellet into an neutral beam heated plasma with a higher thermal energy (discharge #6090).

Discharge Nr.	P_{NBI}, *MW*	*Neon pellet*	E_{th}, *MJ*	E_{mag}, *MJ*	E_{div}^{EQ}/E_{th}, %	E_{div}^{CQ}/E_{mag}, %
5864	0	No	0.040	0.65	100	14
5698	0	Yes	0.055	0.61	~ 0	6
6090	9	Yes	0.5	1.5	12	5

Table 1: *Energy balance during disruptions in ASDEX Upgrade.* P_{NBI} *is the neutral beam heating power,* E_{th} *is the thermal energy of the plasma before the disruption,* E_{mag} *is the magnetic energy of the plasma before the disruption,* E_{div}^{EQ} *is the energy deposited on the divertor plates during the energy quench,* E_{div}^{CQ} *is the energy deposited on the divertor plates during the current quench [21].*

Bolometric measurements confirmed that the amount of energy equivalent to the total plasma thermal energy was radiated within 2 ms after the pellet injection, and that 90%

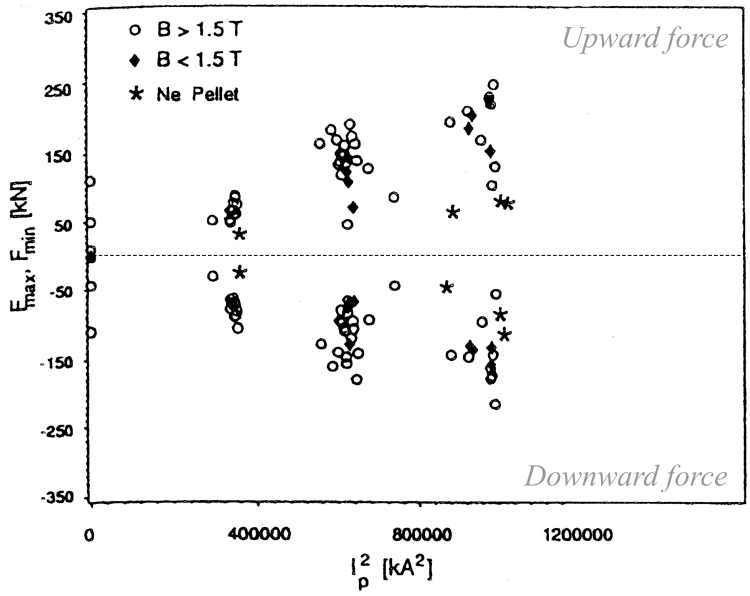

Figure 6: *Maximal upward and downward vertical forces at the ASDEX Upgrade vessel suspension rods in disruptions with and without an injection of neon pellets [21].*

of the full (thermal and magnetic) energy was radiated over the whole disruption such that thermal loads due to heat conduction were small. Only 6% of the total magnetic energy reached the plates during the current quench.

In all discharges terminated by an injection of a neon pellet maximal vertical forces acting on the vessel were in average by 50% lower than in normal disruptions. Fig.6 summarizes the values of the maximal upward and downward forces measured at the vessel suspension rods during the disruptions with the full plasma current. The reduction of the vertical force is attributed to the change of the plasma current decay time after the pellet injection. In normal disruptions, the decay is longer and during this time the plasma column with the full current moves by tens of centimeters in the vertical direction. This vertical displacement induces large halo currents. In disruptions following a pellet injection, the plasma current starts to drop with a higher rate immediately after the injection. The vertical movement of the smaller I_p leads to the induction of smaller halo currents. The higher decay rate results from the increased plasma resistivity both due a drop in the electron temperature and to an increase of the contents of impurities in the plasma described by the effective plasma charge.

Production of runaways was not investigated in [21].

3.1.2 DIII-D

Generation of halo currents in VDE's was explored on the divertor tokamak DIII-D in San Diego, USA [22]. There, cylindrical pellets 2.7 *mm* in diameter by 2.75 *mm* long with

$\sim 4.5 \cdot 10^{20}$ neon atoms, or smaller versions, 1.8 mm diameter and 2.75 mm long consisting of either pure neon or deuterium mixed with 2% neon, were found to be sufficient to terminate the plasma. Pellet penetration of $r/a \sim 0.4$ was then reported. The duration of VDE in this case was shortened by as much as ~ 10 ms for some discharges.

The toroidal asymmetry of the halo currents was characterized by the toroidal peaking factor (TPF). A higher TPF results in a greater vessel response to $j \times B$-forces induced by the halo currents. TPF was defined as the ratio of the toroidal peak in the halo current distribution to its toroidally averaged value. It was observed to lie around 3 in non-pellet discharges and lower than 1.8 for all discharges with a pellet injection. About $\sim$ 10% of the initial plasma current was converted into the halo current at its maximum both for 2.7 mm and for 1.8 mm neon pellets, compared to $\sim$ 30% in reference VDE's. The vertical vessel motion was reduced by $\sim$ 30 – 40%.

A negative feature of the experiments was that short, less than 0.5 ms, bursts of runaway electrons were observed on ECE, soft and hard X-ray signals after some of the injections of pure neon killer pellets. The spike in hard X-ray signals indicated that a burst of runaways was lost immediately after the pellet ablation. The runaways were not confined long enough to sustain a significant current component.

3.1.3 JT-60U

In the Japanese tokamak JT-60, neon ice pellets, 3(4) mm in diameter and 3(4) mm thick, were injected into ohmic and neutral beam heated plasmas and could penetrate up to the plasma core [24]. As in the case of DIII-D, production of runaways was observed after the pellet injections. The runaways were confined in the current quench phase for ~ 50 ms. The existence of the long-living runaway current was attributed to a low level of magnetic fluctuations in the plasma. The generation of runaways was not observed if the magnitude of the fluctuation of the radial magnetic field $\tilde{B}_r$ was large at the time of the energy quench after the pellet injection (solid circles in Fig.7). It was also not observed in disruptions because of a strong gas puff with a low fluctuation magnitude (crosses in Fig.7). Runaways appeared if the fluctuation amplitude < 0.1 T/s for the $n = 1$ mode and < 0.05 T/s for the $n = 2$ mode (open circles in Fig.7). These observations suggest that MHD fluctuations play an important role in determining the generation of runaways.

3.2 Mitigation of disruptions by a gas injection

Mitigation of disruptions based on a pellet injection may not be acceptable for ITER because of the problem of runaway production which present damage for ITER in-vessel inventory (see Section 2.3. An alternative technique of mitigation of disruptions by an injection of a gaseous impurity into a plasma have been investigated.

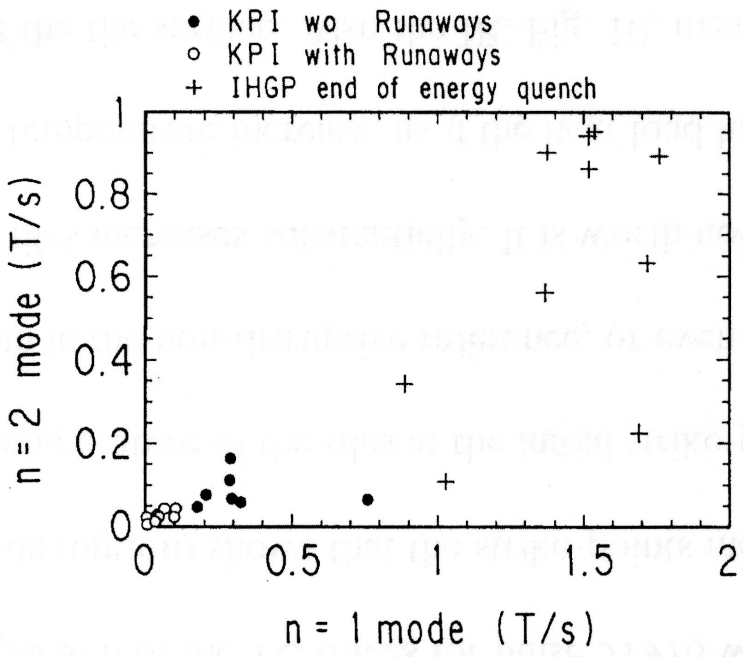

Figure 7: *Magnetic fluctuation* $|\dot{\tilde{B}}_r|$ *for the* $n = 1$ *and 2 modes at the drop in the central* T_e *for a pellet injection and at the end of the energy quench for a density limit in JT-60U. Open circles — runaway generation for a pellet injection, solid circles — runaway generation is not observed for a pellet injection, crosses — runaway generation is not observed for a density limit [24].*

3.2.1 DIII-D

About $4 \cdot 10^{22}$ particles (atoms or molecules) at a high pressure (70 *bar*) were released in 2 – 5 *ms* into DIII-D plasmas [26, 27]. Four kinds of gas were taken: deuterium, helium, neon, argon. It was observed that the gas jet propagated as a neutral gas at sound speed. The dependence of the jet speed on the atomic mass, m, $v_{jet} \propto m^{-1/2}$ was confirmed. As impurities reached the plasma core, the central n_e increased by an order of magnitude due to ionization and T_e collapsed in less than 1 *ms*, initiating the current quench.

In unmitigated disruptions during the thermal quench typically 20 – 40% of the sum of the thermal and magnetic initial energy was conducted on the divertor. After the puff of neon or argon the divertor thermography showed a surface temperature rise consistent with the deposition of 3 – 5% of W_{th}. The integrated radiation energy accounted for the total content $W_{th} + W_{mag}$. Important is that no traces of injected impurities were found in subsequent discharges. The rise in the vessel pressure was only ~ 10 *Pa* and it did not cause any damage to the pumping system.

During these experiments no significant runaway population was observed in high pressure neon and argon injections, while an argon pellet produced a tail of runaway current (Fig.8 a). Calculations of the electric fields during the current quench pointed

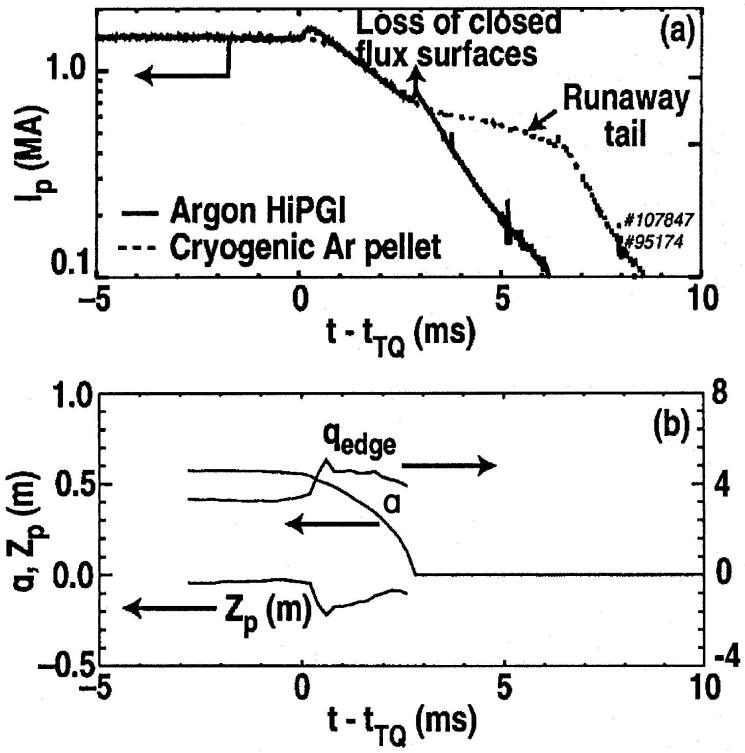

Figure 8: *Time traces of: a) — total plasma current. In comparison to argon cryogenic pellet injection, no sign of confined runaway electron current is found for the high pressure gas injection, b) — core plasma centroid position (midplane: $z = 0$) and core plasma minor radius a, and edge safety factor q during the high pressure gas injection [26].*

further to a complete suppression of runaways at high enough impurity densities ($> 7 \cdot 10^{21}\ m^{-3}$).

In VDE's, poloidal vessel halo currents and their non-axisymmetric peaking were reduced by about a factor of 2 – 4 compared to unmitigated cases. The high pressure gas injection could keep the plasma current without a substantial vertical movement over the time of the current decay (Fig.8 b), and minimize the induction of halo currents.

Looking towards ITER it was concluded that also the ITER plasma would be quenched rapidly through radiation much like in DIII-D at the neon or argon density of $\sim 10^{21}\ m^{-3}$. On the assumption of a uniform dispersion of the thermal and magnetic energies the heat loads would probably not lead to surface melting or ablation for the wall materials. VDE's and halo currents would be reduced because of the fast current termination. For this, a further modest increase in the gas pressure would be required for the gas jet to penetrate to the center of the hotter and higher pressure plasma. Also an increase in the impurity density up to $\sim 8 \cdot 10^{21}\ m^{-3}$ would be necessary to fully suppress runaway production.

3.2.2 JET

Experiment on mitigation of disruptions by a gas puff performed on JET tokamak in Abingdon (UK) were described in [28]. Plasmas in poloidal limiter and elongated configurations were brought at first to a density limit by a graduate slow argon puff. Different amounts of helium ($\sim 6 \cdot 10^{21}$, $\sim 2 \cdot 10^{22}$, $\sim 6 \cdot 10^{22}$ particles) were injected. In a limiter plasma helium puff lead to some reduction of the divertor septum surface temperature seen by a thermography — $250°C$ without helium puff and $150°C$ with it. Even with the smallest gas amount applied no signatures of runaways on hard X-ray and soft X-ray signals were found with a killer gas, whereas pronounced runaway traces both in hard X-ray and soft X-ray existed in usual disruptions.

The decreased heat flux onto the divertor was not observed with VDE's. In contrast, the septum temperature raised up to $500°C$ after the injection of helium while being $350°C$ in a reference example without gas. The helium puff extended the duration of the plasma current quench and resulted in higher vacuum vessel reactions. These facts may indicate that not sufficient gas was injected to mitigate heat loads and vertical forces strong enough.

3.2.3 JT-60U

On JT-60U, three methods of plasma termination have been investigated: using high-Z atoms (argon) only, low-Z atoms (hydrogen) only, and a mixture of these two delivered into the vessel by separate gas valves [29].

An intense argon puff with a rate of 17.9 $Pa\ m^3 s^{-1}$ (1 $Pa\ m^3$ corresponds to $2.4 \cdot 10^{20}$ at room temperature) was observed to lead to an oscillating appearance of runaways followed by a long continuous RE tail late in the current quench phase. The signature of RE's was seen by soft X-ray, hard X-ray and neutron emission diagnostics.

A runaway-free termination was obtained using a slow (2.2 $Pa\ m^3 s^{-1}$) argon, massive (120 $Pa\ m^3 s^{-1}$) hydrogen and a mixtured (2.2 $Pa\ m^3 s^{-1}$ Ar + 120 $Pa\ m^3 s^{-1}$ H) injections (Fig.9). Because the T_e in the center was lower after the drop (at $t \approx 11.95\ s$) in the case of the mixture gas puff, the plasma current was terminated with a higher rate. From Fig.9 i), it is seen that the increase in radiation power is much higher in this case, even though the amount of argon is small as compared to the pure argon injection. Since radiation losses are proportional both to n_e and to n_{Ar}, $P_{rad,Ar} = n_e n_{Ar} L_{Ar}$, ($L_{Ar}(T_e)$ — radiation rate for argon), an admixture of much hydrogen provides an increase in n_e, while argon is responsible for a high L_{Ar}. A growth of the electron density is also beneficial in preventing runaways generation.

Gas mitigation experiments on JT-60U showed that an intense argon injection induced a fast termination, however, the appearance of runaway electrons during the current

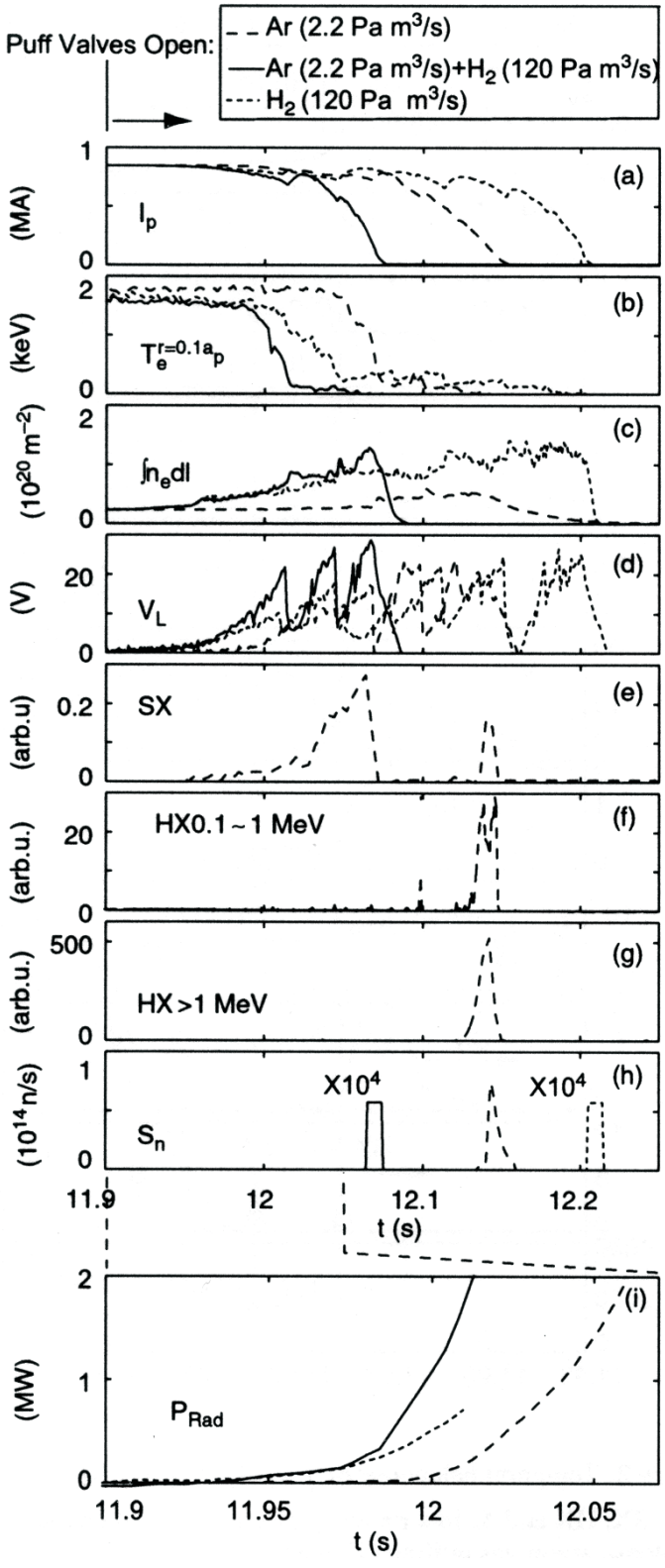

Figure 9: *Temporal evolution of plasma parameters for three shutdown discharges in which argon, hydrogen, and a mixture of argon and hydrogen was injected into JT-60U plasmas. The signal from the top to bottom are: I_p — plasma current, $T_e^{r=0.1a_p}$ — electron temperature at 0.1 of the minor radius, $\int n_e dl$ — line averaged electron density, V_L — loop voltage, SX — soft X-ray signal, HX — hard X-ray signals in the corresponding energy ranges, S_n — neutron emission, P_{rad} — radiation power [29].*

quench phase was observed. No signatures of RE's were detected in the case of a massive hydrogen puff, but the current decay time was then substantially longer. An acceptable compromise was found to be a mixture of argon and hydrogen which achieved a fast termination of plasma current with just weak production of runaways.

The results of the experiments on mitigation of disruptions by pellet and gas injection described above are summarized in Table 2. It is seen that in all cases of the pellet

	Injected impurity	*Reduction of heat flux*	*Reduction of halo currents*	*Runaways*
Pellet injection				
ASDEX Upgrade	Ne	90%		
DIII-D	Ne, D+Ne	40%	30 – 40%	Yes (with Ne)
JT-60U	Ne	85%		Yes
Gas injection				
DIII-D	D, He, Ne, Ar	90%	2 – 4 times	No
JET	He	No		No
JT-60U	H, Ar, H+Ar			Yes (with Ar)

Table 2: *Overview of the results of mitigation of disruptions by pellet and gas injection.*

injection runaway electrons are produced (production of runaways was not investigated on ASDEX Upgrade). After the gas injection runaway electrons are present only in one case (JT-60U, pure argon) and their production is suppressed by a mixed gas puff. On JET, the reduction of heat loads of the wall is not observed, in contrast to the results of the other experiments. A possible reason for this will be discussed in Section 7.3.3.

3.3 Mitigation of disruptions by injection of a liquid jet

An injection of a jet of liquid can be an alternative to the above mentioned techniques which combines the advantage of pellets in deep penetration into a plasma and a massive density build-up, characteristic of a gas puff. This method has not yet been tested on any tokamak and only theoretical explorations of the problem exist [30, 31]. Since its main goal is the prevention of the runaway appearance, an injection of a high-Z material, resulting in a high plasma resistivity and high electric fields, is not acceptable. That is why hydrogen or deuterium are considered for the injection. Still, despite a moderate duration of current decay, keeping $E < E_{crit}$, this will mitigate mechanical loads of the tokamak vessel.

The variation of the diameter of the liquid jet and its velocity presents a mean to

control the amount of the mass of the injected material and its deposition profile in the plasma.

However, a jet has disadvantages as well. When the liquid exits from a nozzle into the vacuum region between the nozzle and plasma, it becomes superheated, and a rapid boiling and vaporization can take place, which destroys the jet. Also breaking into droplets having approximately the size of the initial jet due to surface tension or turbulent pulsations is possible in the vacuum region. Besides, breaking into a chain of droplets can happen already in plasma due to recoil forces originating during ablation. It is supposed, nevertheless, that penetration of a droplet stream should not be essentially different from jet penetration.

In [30] a promising conclusion is drawn concerning a plasma termination in ITER. A wide range of jet parameters can be chosen for this. Taking the ITER parameters to be $R = 8.14\ m$, $a = 2.8\ m$, $n_0 = 10^{14}\ cm^{-3}$, $T_0 = 10^4\ eV$, a deuterium jet would require, for example, the radius of 0.4 cm being injected at a speed of 600 m/s in a time of 5 ms, resulting in a total jet length of 3 m.

3.4 Modeling of disruptions

Interest to a numerical description of a disruption is high, since an appropriate model could confirm our understanding of underlying processes of a disruption. Further, a proper modeling could predict, which of its consequences might present troubles in ITER or an other machine under construction. That is why attempts have been made to calculate the evolution of the main plasma parameters like T_e, n_e, T_i, I_p, Z_{eff} (effective plasma charge) in different approximations.

3.4.1 Thermal quench on DIII-D

On DIII-D, the code KPRAD has been worked out [13, 32]. This is a time dependent model used to simulate the radiation and energy balance in pellet injection experiments. The calculation is carried out on a single given flux surface only, and no radial transport is considered. At first the charge states distribution for the impurity species is solved and the subsequent radiative losses from each charge state are found (this means coronal equilibrium is not assumed). Then a new self-consistent energy balance including radiation losses, ohmic heating and collisional energy exchange between all species is calculated at each time step. The newly found values of the plasma density and temperature are then used for the subsequent ionization balance. The code considers as separate species the original electrons and ions, as well as the impurity ions and the electrons contributed from their ionization. Radiation rates for each charge state k, $L_k(W/m^3)$ are extracted from the ADPAK [33] atomic database. The electron density, n_e, and the density of each

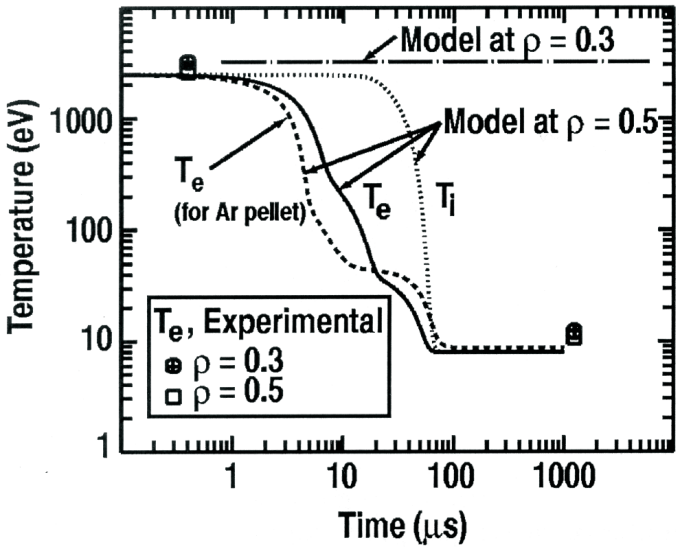

Figure 10: *Time evolution of the electron temperature (solid) and ion temperature (dotted) during a neon pellet ablation as calculated from the KPRAD code at normalized radii of $r/a = 0.5$ and $r/a = 0.3$ (dash-dot). Experimental measurements of the electron temperature (from Thomson scattering) before and after the pellet injection at $r/a = 0.3$ (circle with cross) and $r/a = 0.5$ (square). Also shown is a KPRAD code calculation of the electron temperature evolution if the pellet material was argon instead of neon (dashed) [32].*

charge state, n_k, are taken to calculate the radiated power $P_{rad,k} = n_e n_k L_k$. Initial plasma parameters (n_{e0},T_{e0}, j_0) are taken from measurements. The local current density, j, is held proportional to the measured total plasma current I_p, i.e. $j(t) = j_0 \cdot I_p(t)/I_{p0}$. Ohmic heating power, P_{ohmic}, and the parallel electric field, E, are derived from the Spitzer resistivity ($\eta \propto Z_{eff} T_e^{-3/2}$, $P_{ohmic} = \eta j^2$, $E = \eta j$). The code predicts the time evolution of electron and ion temperature, electron density, average charge state of impurity, total radiation, and radiation per charge state. An example of the code run for an injection of a neon pellet is shown in Fig.10. The experimentally measured electron temperatures at $r/a = 0.5$ agree with the KPRAD prediction, but the code does not predict the measured collapse of the central temperature $r/a < 0.4$, that is attributed to anomalous penetration of the pellet impurity into the core (KPRAD does not calculate transport).

3.4.2 Post-thermal quench core and halo current evolution on DIII-D

The core and halo current evolution for the case of a helium puff induced disruption has been modeled on DIII-D [34]. The model consists of two coupled differential equations. The core current decays resistively with a decay rate which increases in time as the plasma core shrinks. At the same time, the current is convectively transferred from the core to the halo region halo as the motion of the plasma into the limiting surface causes closed

core field lines to open up and become halo field lines. The core current evolution is thus described by a circuit equation derived from Faraday's law and modified to include the convective loss:

$$\frac{dI_p^{core}}{dt} = -\gamma_{p0}\frac{\kappa_0 a_{p0}^2}{\eta_{p0}}\left(\frac{\eta_p}{\kappa a_p^2}\right) I_p^{core} + (1-f_{re})J_{edge}\frac{d}{dt}(\kappa a_p^2) - \frac{M_{ph}}{L_p}\frac{R_{h\ eff}}{L_{h\ eff}} I_{h\ tor}, \qquad (5)$$

where I_p^{core} is the core (toroidal) plasma current, γ_p represents the core current decay rate, a_p is the core plasma minor radius, η_p is the core plasma resistivity, L_p is the total core plasma self inductance, f_{re} is the fraction of the lost edge current which is "scraped off" at the limiting surface and reinduced in the core plasma (the remainder is induced or convected into the halo plasma), and $J_{edge} \equiv f_J I_p^{core}/A_p$ is the toroidal current density at the last closed flux surface. The subscript *0* denotes values at the beginning of the current quench; quantities without this subscript are instantaneous values. The second term describes the effect of closed core plasma field lines opening and becoming part of the halo as the plasma moves into the limiting surface. This term is approximately proportional to the vertical growth rate, and therefore becomes important when the growth rate is comparable to or larger than the core plasma resistive decay rate γ_{p0}. f_J is the ratio of the edge current density to the average core plasma current density, and $A_p = \pi\kappa a_p^2$ is the poloidal cross-sectional area of the core plasma. The core plasma resistive decay rate at the start of current quench, γ_{p0}, is given by

$$\gamma_{p0} \equiv \frac{R_p}{L_p} \cong \frac{2\eta_{p0}}{\mu_0 \Gamma_{p0}\kappa_0 a_{p0}^2}, \qquad (6)$$

where $\Gamma_{p0} \equiv \ln|8R_0/a_{p0}\sqrt{\kappa_0}| + (l_{i0}/2) - 2$, and l_{i0} is the normalized internal inductance per unit length at the start of the current quench.

The halo circuit equation, also derived from Faraday's law, includes similar inductive-resistive terms to those of the core current equation, Eq.5

$$\frac{dI_{h\ tor}}{dt} = -\frac{R_{h\ eff}}{L_{h\ eff}} I_{h\ tor} - \frac{M_{hp}}{L_{h\ eff}}\frac{dI_p^{core}}{dt} - \frac{1}{L_{h\ eff}}\frac{d}{dt}\left(\frac{\Phi_h}{q_h}\right). \qquad (7)$$

Equation 7 represents the dynamic evolution of the toroidal halo current, $I_{h\ tor}$, driven by the loss rate of the core plasma current, dI_p^{core}/dt (including resistive decay, convection, and scraping), and the rate of change of the poloidal projection of toroidal flux linked by the halo current, $d(\Phi_h/q_h)/dt$. Here use is made of the force-free constraint relating the poloidal halo current, I_{hpol}, to the toroidal halo current: $I_{h\ pol} = I_{h\ tor}/q_h$. M_{hp} is the mutual inductance between the core plasma and halo currents. The effective halo self inductance, L_{eff}, and resistance, R_{eff}, are given respectively by

$$L_{h\ eff} \cong L_{h\ tor}\left[1 + \kappa\left(\frac{a_h}{q_h R_0}\right)^2\left(\ln\left|\frac{8R_0}{a_h\sqrt{\kappa}}\right| - 2\right)^{-1}\right] \qquad (8)$$

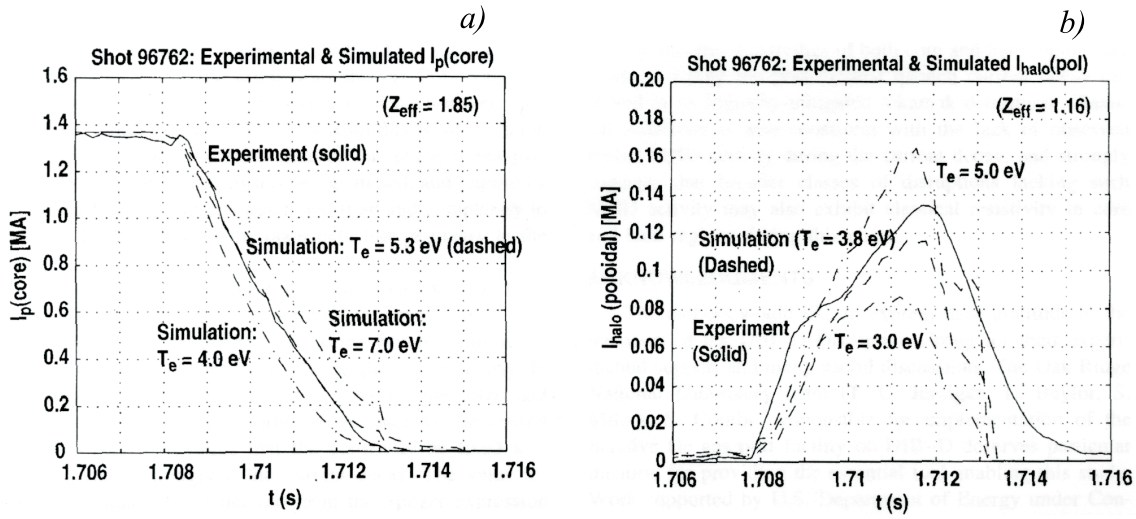

Figure 11: *a) — Comparison of the experimental and simulated core current decay history for a massive helium puff induced disruption in DIII-D. b) — Comparison of the experimental and simulated halo current evolution history [34].*

and

$$R_{h\ eff} \cong R_{h\ tor}\left[1+\kappa\left(\frac{a_h}{q_h R_0}\right)^2\right], \tag{9}$$

in terms of the halo toroidal self inductance, $L_{h\ tor} \cong \mu_0 R_0(\ln|8R_0/a_h\sqrt{\kappa}| - 2)$, and resistance, $R_{h\ tor} \cong \eta_h R_0/\kappa a_h \delta_h$, where η_h is the parallel resistivity in the halo region. These terms depend on the evolution of the halo geometry, which in turn depends on the plasma movement and core plasma current history.

Fig.11 a) shows a comparison between the simulated and reconstructed core plasma current evolution for various values of T_e (Z_{eff} is fixed at its measured value). The solid line indicates the experimentally measured core plasma current decay. The dashed line, denoting the current decay history simulated by assuming the core T_e and Z_{eff} precisely matching the measured values, shows very good agreement throughout the core current decay history. The dash-dot curves show current decay histories resulting from electron temperatures varied from the measured value by $\sim \pm 1.5eV$ and using the measured value of Z_{eff}. These latter simulations show significant deviation from the experimental history. Fig.11 b) shows a similar comparison between the simulated and measured poloidal halo current evolution. As in the core current decay simulation, the dashed line denoting the halo current history simulated using measured values of T_e and Z_{eff} shows very good agreement throughout the halo current evolution, demonstrating that the resistivities of both core and halo regions are classical during the post-thermal quench current decay observed in an impurity-provoked tokamak disruption.

3.4.3 Discharge termination for JT-60U

A question of modeling of a radiative plasma termination has been also addressed on JT-60U [29, 11]. The simulation is time dependent but does not contain any spatial coordinate. It follows the temperature behaviour after an injection of impurity by analyzing a simple zero-dimensional power balance equation $d/dt(3nT) = P_{oh} - P_L$, P_{oh} — ohmic heating, P_L — impurity radiation losses. By putting the time derivative d/dt to zero, an equilibrium temperature $\widetilde{T_e}$ can be obtained where P_L is compensated by P_{oh}. Using the Spitzer resistivity, the toroidal electric field, a driving mechanism for runaway electrons production, is found: $E \propto Z_{eff} T_e^{-3/2} j$. Application of various amounts and kinds of gas (D, N, Ne, Ar, Kr, Xe) and their mixtures leads to different radiation rates and number of electrons released through ionization of the gas. This has a direkt impact on the plasma cooling time and the value $\widetilde{T_e}$. The calculation concentrates mostly on finding regions in the (n_{imp}-$\widetilde{T_e}$) dependence (n_{imp} — density of the injected impurity) where production of runaway electrons is absent.

3.4.4 Discharge termination for ITER

Kuteev *et al.* have considered a quench or ramp-down of a plasma discharge in ITER by use of a krypton pellet [12]. The calculation is zero-dimensional and the basic equations have the form:

$$\frac{d}{dt}(3n_e T_e) = \frac{j^2}{\sigma} - n_e n_{Kr} Q_{rad}, \tag{10}$$

$$\frac{d}{dt}(\frac{1}{2} L I_{pl}^2) = -\frac{j^2 V_{pl}}{\sigma}, \tag{11}$$

where $j = I_{pl}/\pi a^2 \kappa$ is the average plasma current density (κ is elongation), σ — Spitzer conductivity, n_{Kr} — the average krypton density created by the pellet injection, and L — plasma inductance, assumed to be constant. The ion and electron temperatures are supposed to be equal.

The ablation of a pellet is simulated giving the penetration length of the pellet cloud and the number of ablated atoms. These data are then put to the above set of equations to produce the time dependence of I_{pl} and T_e. The output of the code for the case of a $r = 5\ mm$ krypton pellet is displayed in Fig.12. Initially, the ohmic heating power is negligible and the temperature decays to a few tens of eV in 20 ms. The plasma current does not change during this period. Then the radiation is balanced by the ohmic heating and the temperature falls together with the current density. This stage takes another 50 ms. A termination of a discharge can be obtained in 0.08 s.

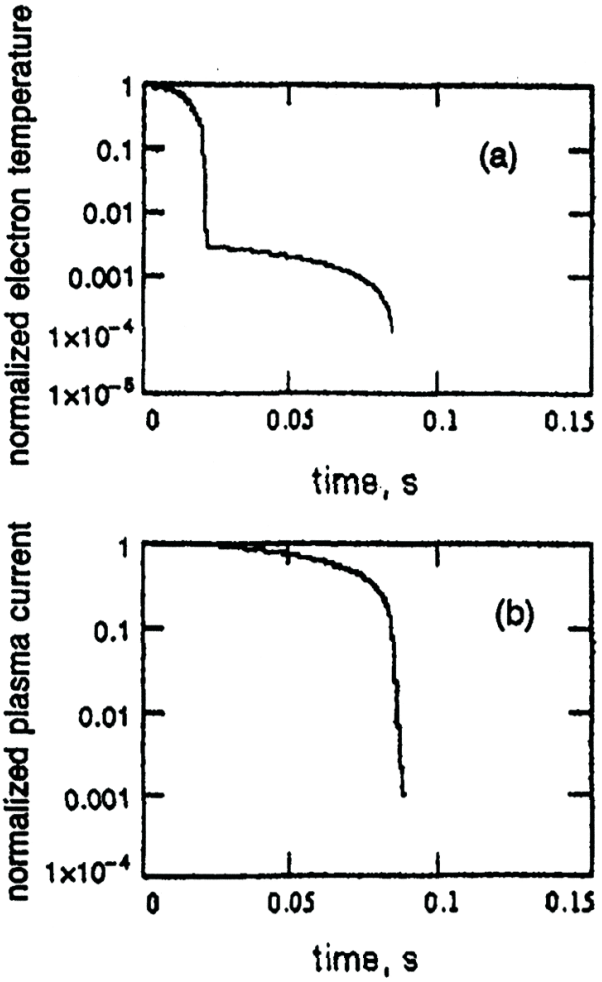

Figure 12: *Evolution of plasma parameters after injection: (a) — normalized electron temperature, (b) — normalized plasma current [12].*

4 DEVELOPMENT OF A FAST GAS VALVE FOR THE MITIGATION OF DISRUPTIONS

4.1 Construction of the gas valve

Fig.13 shows a drawing of the valve: in the normal state an aluminium piston (6) pushed by the excessive pressure in the chamber (13) separates the working volume (3) from the discharge vessel. Once the pan-cake valve coil (11) is activated, eddy currents are induced in the piston and it is pulled back thus opening a path for the gas flow. After the decay of the currents induced in the piston it is again driven under the action of the gas in the volume (13) which brings it into the original position. The electrical current is supplied by a capacity with $C_{load} = 0.180\ mF$ charged at a voltage of up to $U_{load} = 2\ kV$. The circuit is switched by an ignitron after a trigger signal. The fuelling gas reservoir can be varied (by machining) between 5 and 250 ml. The fuelling pressure should be high

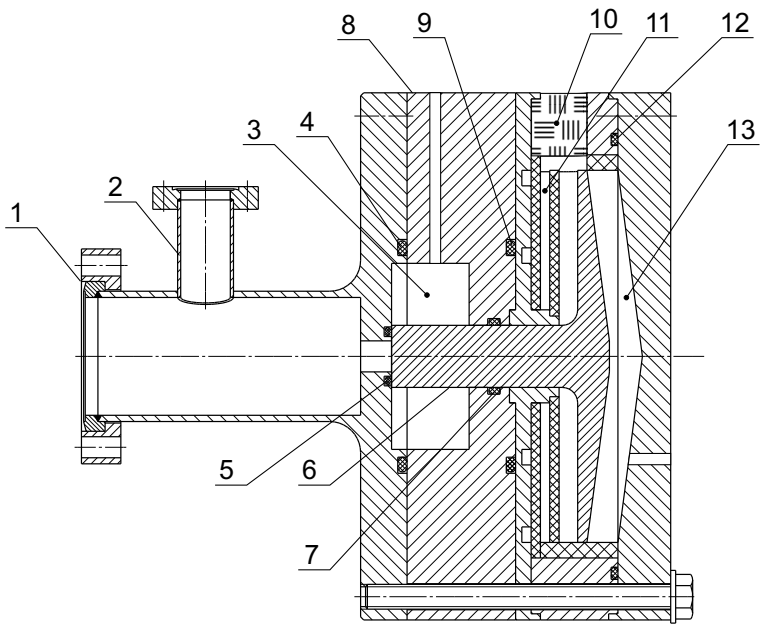

Figure 13: *Cross section drawing of the fast valve. 1 – CF 35 flange; 2 – pressure measurement flange; 3 – working reservoir; 4, 5, 7, 9, 12 – o-rings; 6 – piston; 8 – case; 10 – HV coil input (filled with epoxy); 11 – coil; 13 – closing gas volume.*

enough enabling a fast gas flow into a tokamak chamber. The working pressure is selected between 1 – 30 *bar*, at which the gas is supposed to expand in vacuum with its sound speed, because no profiled exit nozzle is foreseen in the present design. O-ring (5) seals the reservoir from the discharge chamber, and (7) — the reservoir from a back volume (13); the pressure in this back volume guarantees a fast closing of the stem after its activation. Towards the discharge chamber the valve is equipped with a high vacuum CF 35 flange (1) in order to obey normal tokamak requirements. An additional measurement flange (2) is foreseen as well. The total length of the valve amounts to 20 *cm* and its diameter — to 17 *cm*. The photos of the complete valve and of the internal parts are shown in Fig. 14, a) and 14, b), respectively.

An important feature of the design of the valve is an avoidance of any ferrite material, allowing it to be installed very close to a tokamak with its full magnetic field. In our case on ASDEX Upgrade the valve operated successfully in the full field of 2 T. Mounting the valve directly on a tokamak vessel results in a faster reaction time, because there is no distance separating the valve from the vessel. Other valves may use a ferromagnetic stem, which is attracted into a coil. This mount with a ferromagnetic stem is smaller and has a higher coupling to the electric circuit; but its disadvantage is that e.g. the tokamak toroidal magnetic field saturates the ferrite stem such that it can not operate directly at the vacuum vessel.

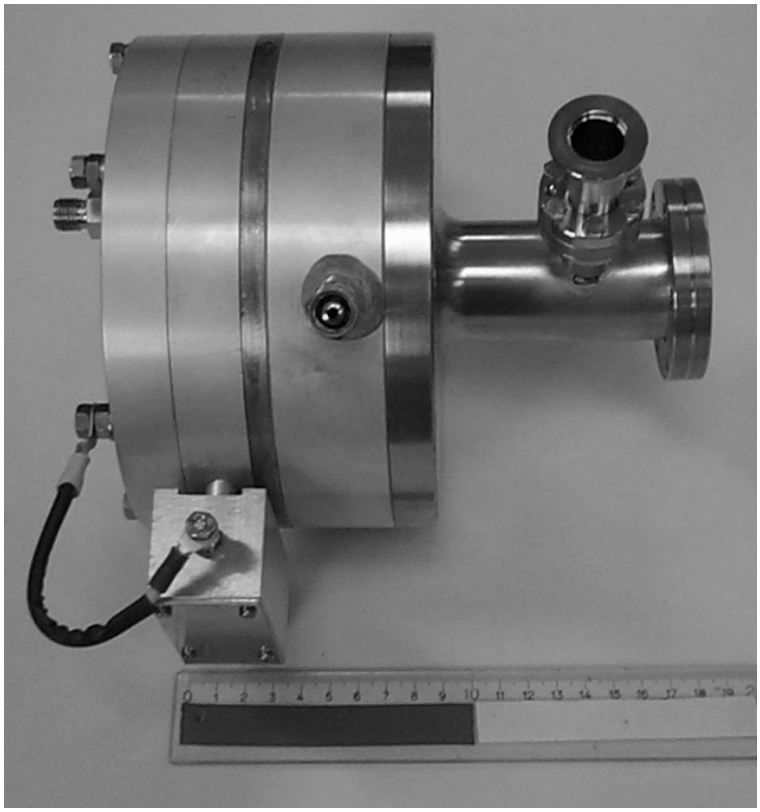

a)

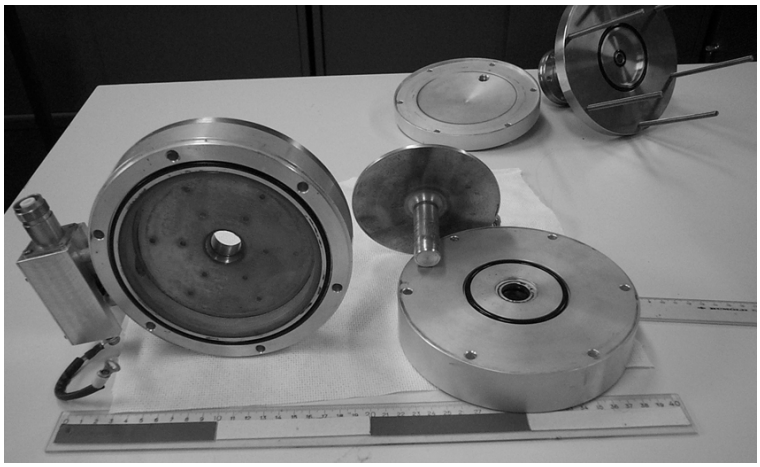

b)

Figure 14: *Photographs of the fast valve: a) – general view, b) – disassembled to the component parts.*

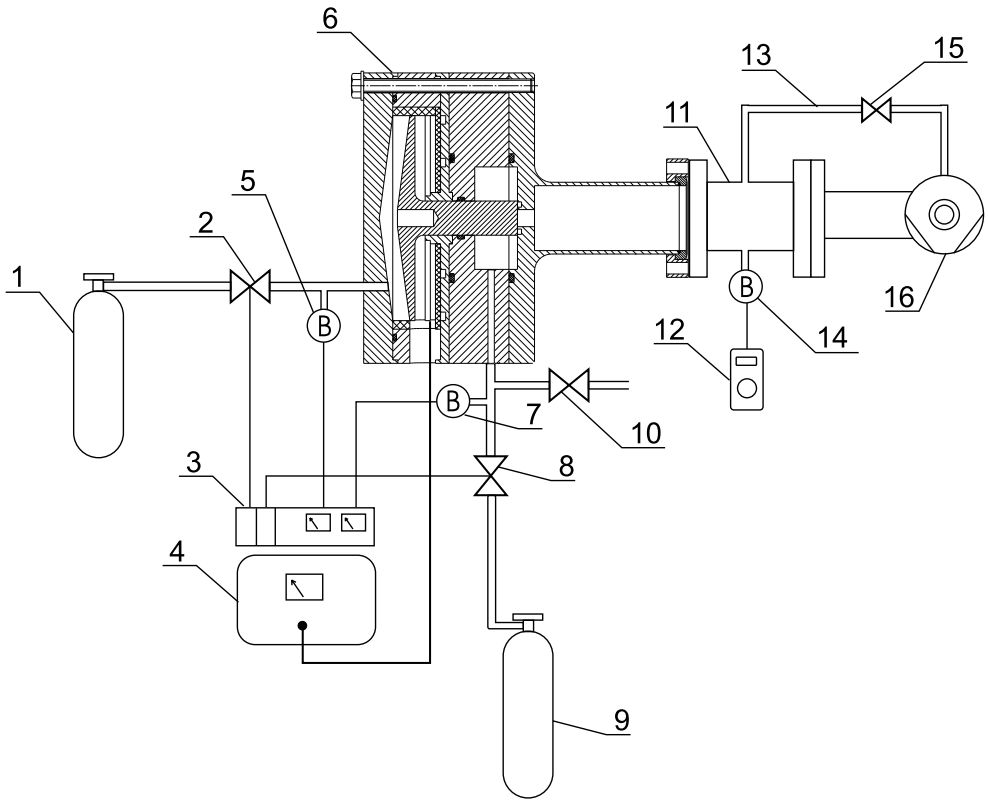

Figure 15: *Equipment test scheme. 1, 9 – gas bottles; 2, 8 – safety valves; 3 – safety valves control, power supply and indication for the baratrons; 4 – fast valve high voltage power supply; 5, 7, 14 – baratrons; 6 – fast valve; 10 – pumping valve; 11 – target volume; 12 – digital voltmeter; 13 – by-path; 15 – hand valve; 16 – turbopump.*

4.2 Calibration of the valve and its characteristics

In order to check the valve performance, a test bench was assembled as indicated in Fig.15. The test bench included the fast valve (6) attached to a vacuum volume (11), pressure meters — baratrons (5, 7, 14), a turbo pump (16), a high voltage supply (4) and gas bottles (1, 9). Several safety valves (2, 8) were positioned to avoid a situation when the whole gas bottle would be released into a discharge volume upon failure of the fast valve. These pneumatically activated valves were located close to the fast valve such that the extra gas reservoir was minimized. One valve (10) was located to pump out the working volume if the type of gas had to be changed. A controller (3), that united the functions of supplying the electromagnetic valves and baratrons with power and displaying pressure read-outs was assembled in a standard 19-inch Eurocard case. The coil of the fast valve was fed from a capacitor storage (4) using an ignitron high current switch. Both devices were controlled either manually or by TTL signals. A typical flow diagram during the operation in the lab could be reflected as follows (Table 3).

At first the valve 2 opens providing a gas pressure on the stem and closing it off

Event	*Valve 2*	*Fast valve 6*	*Valve 8*	*Valve 10*	*Hand valve 15*
1. Closing pressure on	open	closed	closed	closed	closed
2. Working pressure on	closed	closed	open	closed	closed
3. Shot	closed	open	closed	closed	closed
4. Pumping out	closed	closed	closed	closed	open
5. Pumping the working volume out (optional)	closed	closed	closed	open	closed

Table 3: *Valves states on the different stages of operation.*

from the discharge vessel (row 1 in the Table). Then the valve reservoir is refilled by the working gas up to the desired pressure by opening the valve 8 (row 2). A high voltage pulse pulls the stem back opening the fast valve 6 for about After the shot, the injected gas is pumped out from the target volume 11 through the hand valve 15 and by-pass 13.

For the actual experiments on tokamaks similar actions are performed, except for the step 4. Step 1 has to be executed only occasionally. The valve is so tight that the pressure remains for days without refilling.

During the tests the following characteristics were considered:

- the amount of injected gas,

- gas throughput and the reaction time,

- reliability of operation.

To determine how much gas is injected from the working volume for each valve shot, a scan over the gas pressure was made. There are two possibilities to calculate the number of injected particles: one can directly measure the pressure increase in the target volume after the shot or derive it knowing the values of the gas pressure before the injection and the working reservoir volume. The calibration curves obtained in the former way for two different cases (namely, for the 30 cm^{-3}- and 60 cm^{-3} volumes) are shown in Fig.16. The other parameters were 1.5 kV for activation of the valve coil and 5 bar helium for closing the valve (pressure in the volume 13, Fig.13). The absolute accuracy of the amount of the injected gas is about 10% , mainly given by the irregular shape of the target volume (11, Fig.15), into which the gas is released. In the operational pressure range the amount of the injected gas is proportional to that stored initially in the valve. Experiments on ASDEX Upgrade (with the total vessel volume 14 m^3) have shown that already about 30 $mbar \cdot l (7.5 \cdot 10^{20}$ particles) of gas is sufficient to generate reliably a disruption. On the other hand, the amount of the injected gas is low enough not to shut the pumping

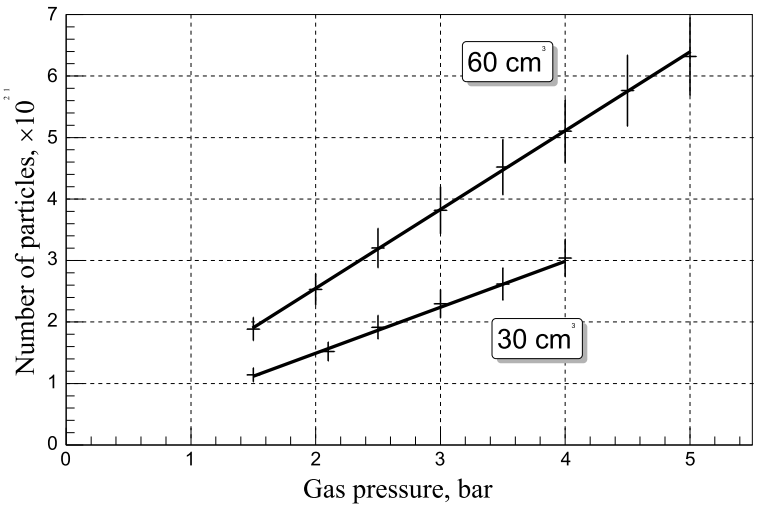

Figure 16: *Number of injected particles vs. gas pressure for two different working volumes,* 30 cm^3 *and* 60 cm^3. *The pressure is in absolute units.*

system (e.g. turbo-pumps) down or provoke a detrimental heat load at cryo-pumps. If necessary, the working pressure may be increased up to 30 *bar*.

The figure of quality of the valve is the gas throughput and the reaction time of the valve. Piezoelectric valves [35] have ideal short response time, but their throughput is too small. Therefore a valve with a piston [36, 37] is required that gives sufficient clearance for a gas flow. The most direct response to the action of the valve is a pressure rise measurement in the test chamber after the shot. However, normal pressure gauges are unable to detect the pressure increase in the pressure range involved. Ionization gauges or Penning gauges react fast, but they go into saturation at moderate pressures; baratrons have a reaction time of milliseconds and are therefore too slow. In order to obtain the opening characteristic of the valve, we utilized the following method: we inserted a glass fiber into the bore hole which leads to the filling reservoir, then we illuminated the glass fiber and detected the light at the valve exit by mounting a photomultiplier at the CF flange of the valve. The light from the glass fiber was reflected many times diffusely at the reservoir walls; therefore the multiplier signal was directly proportional to the opening of the valve. Represented in Fig. 17, a) and 17, b) are the initiation of this opening with the extended time scale and the full process, respectively. One sees that the valve starts to open 0.5 *ms* after the trigger signal. After about 1 ms, it is nearly completely open and after 18 *ms* is closed again due to the repulsive pressure in the back volume.

The curve of the electrical current through the valve coil is of interest as well. Fig.18 gives the plot measured by a commercial pulse current measurement instrument. The current maximum is reached after 400 μs and then the signal decays with the rate of a critically damped oscillation. Since the opening of the valve starts at about the maximum

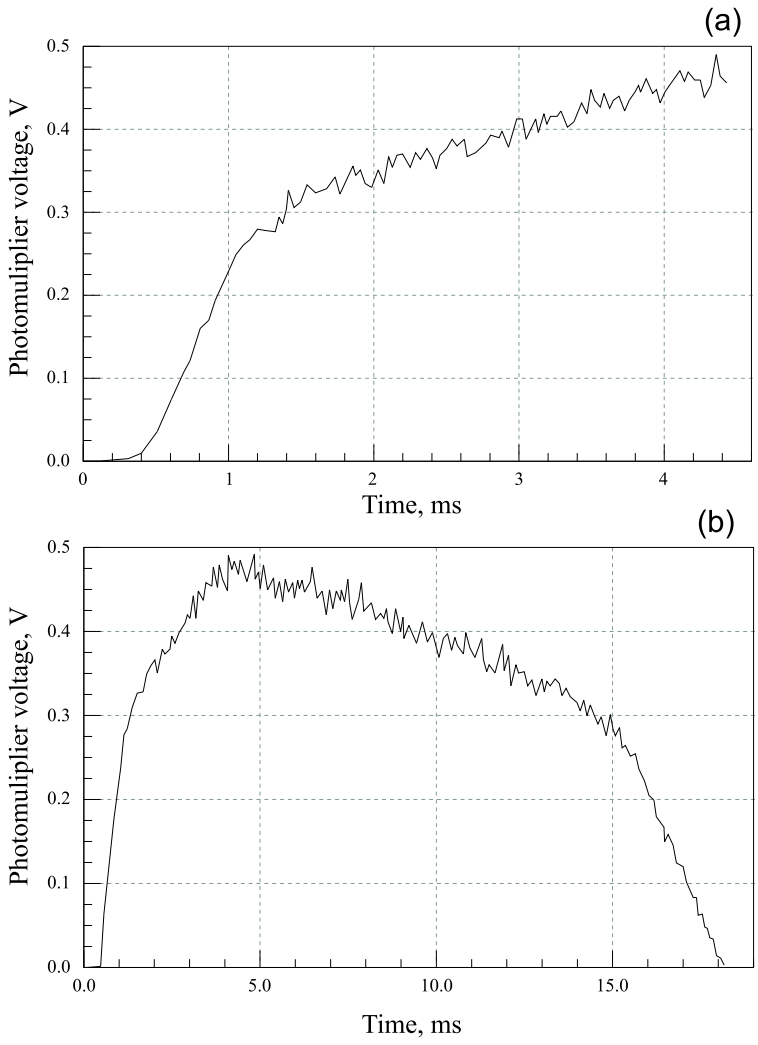

Figure 17: *Opening characteristics of the fast valve. a) – initial stage with the extended time scale, b) – full process.*

of the valve current, i.e. the stem reaches its maximum kinetic energy also close to this time, the energy transfer from the electrical circuit to mechanical energy is close to its maximum. This means, the capacitance C is well chosen for the given inductance of the valve. The electrical circuit is switched by an ignitron; this tube switches only one polarity of the current. The fact that the valve current is critically damped is, therefore, very favourable because otherwise high voltages in the coil would be generated due to dB/dt when the coil current were terminated when passing zero. This high induced voltage has proven to be dangerous for the circuit because it may create shorts in the pancake coil and damage it.

To check whether the valve is reliable over a long operation period and whether it remains vacuum-tight, continuous cyclic testing was undertaken. A pressure of 2.5 *bar* helium was applied for both closing the valve and injecting gas. 2 kV voltage was used for activating. Shots occurred at a frequency of one shot every 40 seconds, determined

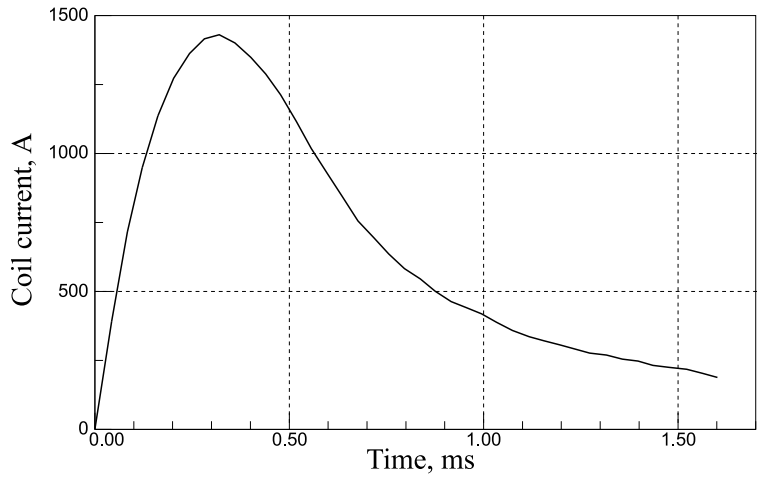

Figure 18: *Trace of the electrical current through the valve coil.*

by the charging time of the capacitance and the pumping rate of the turbopump. The pressure signal was measured by a baratron in the target volume (11, Fig.15). In total, about 1000 shots were performed within the framework of this test and no change in the character of operation was found. Up to now, about 500 more gas puffs have been done during experimental programs, again without any failure.

5 EXPERIMENTS ON ASDEX Upgrade

A series of experiments on mitigation of disruptions using the fast valve was carried out on the ASDEX Upgrade tokamak. The machine is briefly described in the following section. Thereafter, the motivation of the experiments and the equipment used are given. Finally, the interpretation of the experimental results is discussed.

5.1 Tokamak ASDEX Upgrade

The major parameters of ASDEX Upgrade are listed in Table 4. Fig.19 shows the poloidal

Major plasma radius, m	1.65
Minor plasma radius, m	0.5
Elongation	1.8
Plasma volume, m^3	14
Plasma current, MA	0.4 – 1.6
Maximal toroidal field, T	3.1
Working gas	deuterium, hydrogen, helium
Electron density, m^{-3}	10^{20}
Electron temperature, keV	6 – 10
Pulse duration, s	<10
First wall material	carbon, tungsten

Table 4: *Major parameters of the ASDEX Upgrade tokamak.*

cross-section of the machine. The abbreviation ASDEX stands for Axial Symmetric Divertor EXperiment. Its characteristic feature is a poloidal divertor which can produce elongated plasmas either with one X-point (top- or bottom-diverted configuration) or with two X-points.

5.2 Motivation, tasks and experimental arrangement

Disruption mitigation is an important topic which occupies a permanent place in the ASDEX Upgrade activities. Much work has been done with large pellets (so-called killer pellets) to terminate the discharge [38] and a neural network to predict situations which result in disruptions [39]. Together with us, the first experiments on mitigation of disruptions by a gas injection were started on ASDEX Upgrade. The following questions were raised:

1) to which extent is a large gas injection for mitigation of disruptions acceptable on ASDEX Upgrade?

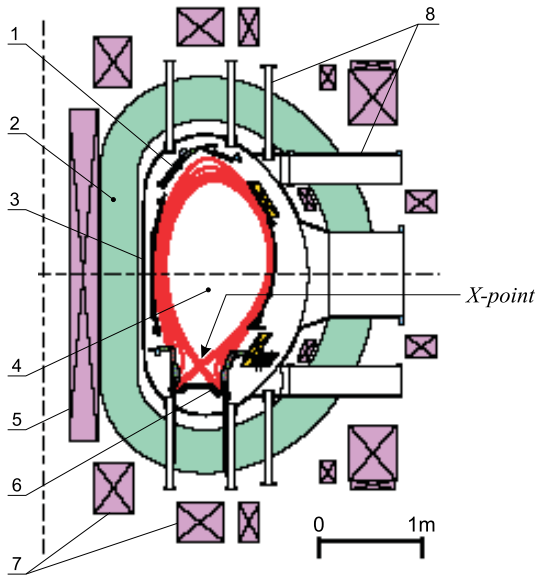

Figure 19: *Poloidal cross-section of the ASDEX Upgrade experiment. 1 – upper divertor plates, 2 – toroidal field coils, 3 – vacuum vessel, 4 – plasma, 5 – transformer yoke, 6 – lower divertor plates, 7 – vertical field coils, 8 – vacuum ports.*

2) how fast does killer gas terminate a plasma discharge, that is by how much does it shorten the current quench phase?

3) does killer gas injection reduce the value and/or the character of distribution of the heat flux onto the divertor surface?

4) how efficient is killer gas injection in reducing halo currents and mechanical loads on the tokamak vessel?

5) do killer gas induced disruptions produce runaways?

6) which kind and amount of killer gas is the optimal choice for mitigation?

The point #2 should be investigated because the injection of a large amount of gas is a technique of an emergency discharge termination and it must have a sufficient capability of a fast dissipation of the plasma current. This is important, in particular, for mitigation of VDE's. The plasma current decay rate $\frac{1}{I_p}\frac{dI_p}{dt}$ should be higher than the rate of the vertical movement $\frac{1}{z}\frac{dz}{dt}$, where z is the distance to the vessel's wall. In this case the current decays before it touches the wall and the problem of halo currents is minimized. However, a fast current decay induces a high loop voltage and currents in vessel components. The induction of these currents must be taken into account by the mechanical design.

The scheme of the experimental arrangement is presented in Fig.20. The fast valve (10) is connected to a gate-valve (1) opening the access inside the vacuum vessel through an intermediate volume (3) and an electrical insulator (2). A turbopump (8) is used to

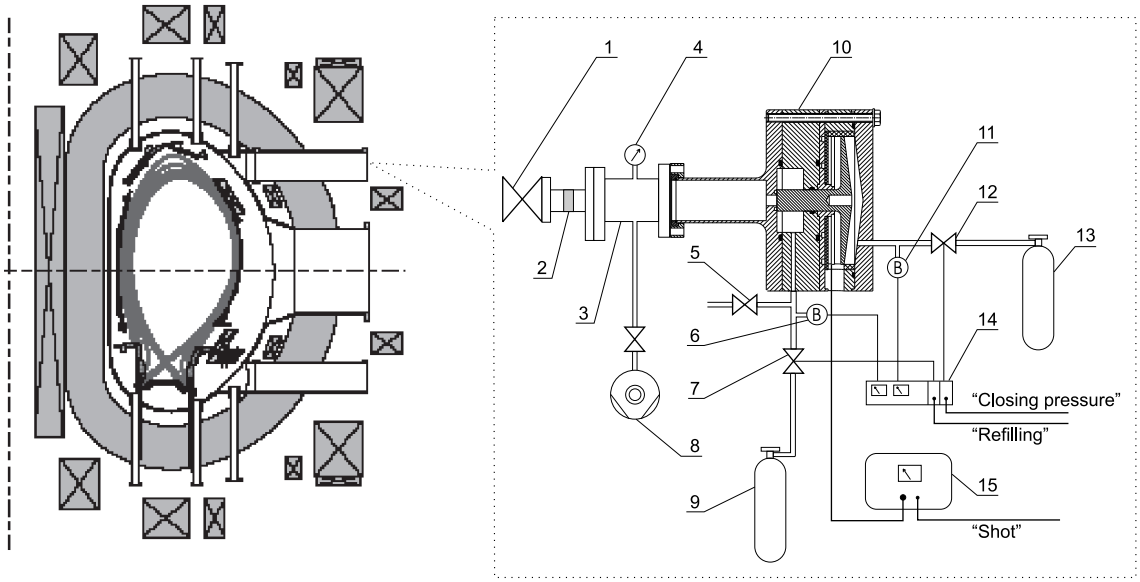

Figure 20: *Setup of the fast gas valve and its position on ASDEX Upgrade. 1 – gate-valve to the vacuum vessel, 2 – electrical insulator, 3 – intermediate volume, 4 – "ionovac" pressure gauge, 5, 7, 12 – safety valves, 6, 11 – baratrons, 8 – turbopump, 9, 13 – gas bottles, 10 – fast valve, 14 – control unit, 15 – high voltage generator. For a better view, the equipment in the dotted box is shown on an enlarged scale.*

pump this volume. The pressure in this volume is monitored by a "ionovac" pressure gauge (4). Opening of the gate-valve #1 is possible only after reaching an acceptable vacuum in the exit nozzle of the fast valve. The rest of the equipment including a power generator (15), control unit (14), safety valves (5, 7, 12), baratrons (6, 11) and gas bottles (9, 13) is the same as during calibration (see Section 4).

Timing is based on the general timing system of ASDEX Upgrade. Three signals associated with different stages of the tokamak discharge control the valve operation. Firstly, the time marker "closing pressure" opens the valve #12 providing the pressure for closing the fast valve (Fig.20). As was mentioned in Section 4, the restoration of this pressure does not need to be done often because it remains for a long time without refilling. The second time marker, "refilling", refills the working volume with the chosen gas by opening the safety valve #7. This 'ready-to-shoot' state lasts until the final signal, "shot", switches on the high voltage generator (15) and activates the valve coil. The gas is then released into the vessel. The time marker "shot" can be preset either manually at a desired time before a plasma discharge or produced by a computer during a plasma discharge (see Subsection 5.3 "Scenarios of operation"). After this, the cycle is repeated. The time interval between discharges on ASDEX Upgrade is always longer than it is required to prepare the fast valve for the next gas puff.

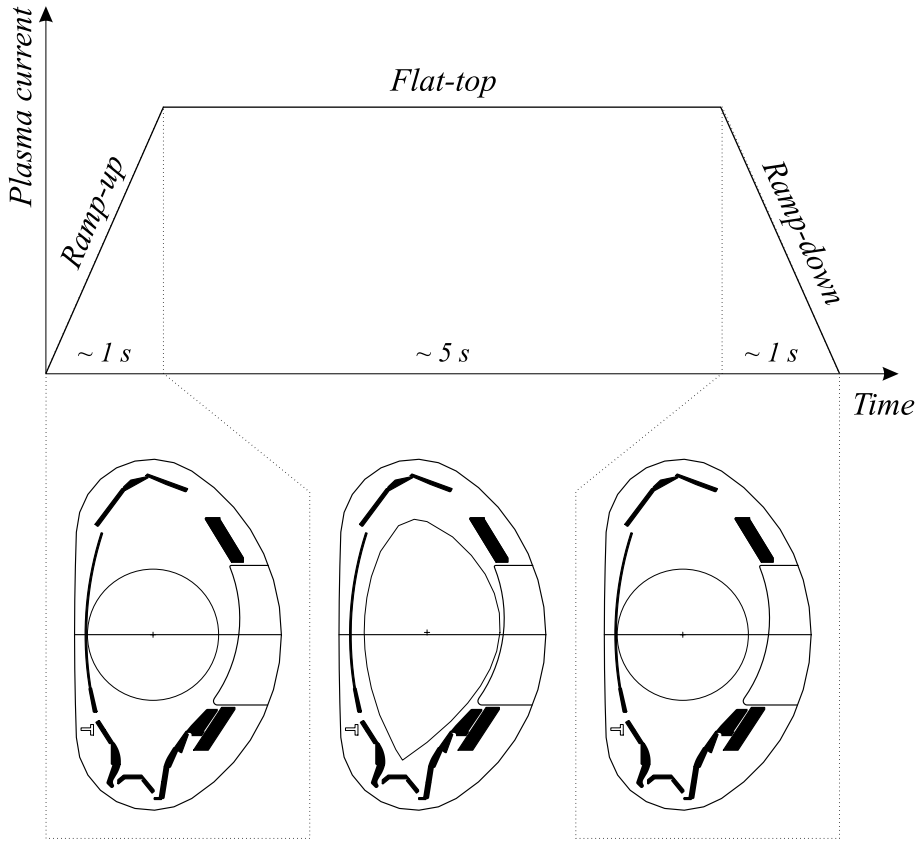

Figure 21: *Different stages of a discharge in ASDEX Upgrade and the corresponding shapes of the plasma.*

5.3 Scenarios of operation

At the initial stage of every tokamak discharge the plasma current is raised (current "ramp-up") and at the end it is lowered (current "ramp-down"). In between, there is a stage at which the current is kept constant (current "flat-top"), and this is the main part of a discharge. During the ramp-up and ramp-down the divertor and vertical magnetic field coils for plasma elongation are switched off. The plasma has a circular shape, with the wall serving as a limiter (Fig.21). During the flat-top phase the plasma is elongated.

a) Circular plasma case. In an elongated plasma a strong gas puff leads to the VDE described in Section 2.2. The collapse of the plasma against the wall releases a large amount of impurities. It is then difficult to distinguish the influence of the injected gas from effects produced by the released impurities. That is why the experiments with a gas puff were partially carried out in circular plasmas where VDE does not occur. However, it will be seen later that natural disruptions without a gas injection occasionally end with a vertical movement similar to VDE.

b) Elongated plasma case. The very end of the flat-top phase of a discharge with the lower X-point is used to investigate the response of an elongated plasma for a fast massive

gas puff.

For both cases *a)* and *b)* 3 different gases are tested. In order to obtain a favourable effect, one needs a minimum number of particles injected, which roughly corresponds to the number of plasma particles during a density limit disruption. However, one also does not want to inject too much gas, because then vacuum pumps or diagnostics may be affected. In the experiments, different amounts of gas are injected, namely, $\approx 120\ mbar \cdot l$ of gas ("$\approx$" sign is set here, because no precise measurements of the working pressure were available at that time), 80, 30 and 25 $mbar \cdot l$. This corresponds to the number of injected atoms of $3{\cdot}10^{21}$, $2{\cdot}10^{21}$, $7.5{\cdot}10^{20}$ and $6{\cdot}10^{20}$, respectively. Taking the vessel volume to be 45 m^3 the pressure increase in the vessel due to the injection of the maximum number of particles can be esimated as

$$\Delta p = nkT = \frac{3 \cdot 10^{21} 1.38 \cdot 10^{23} 300}{45} \approx 0.003\ mbar, \tag{12}$$

where k is the Boltzmann constant and T is the gas temperature (300 K). This is smaller than the upper in-vessel pressure limit of 0.01 $mbar$ on ASDEX Upgrade. For most cases, the time of the gas puff is set manually.

c) After performing the experiments *a)* and *b)* the gas injection equipment is combined with a locked mode indicator taken as a disruption warning signal. The locked mode indicator analyses the frequency of rotating MHD modes derived from the signals of the poloidal magnetic filed perturbations. When the frequency drops the output signal of the indicator increases. In a density limit disruption with detectable precursors the valve is in a feedback loop in which the trigger time is given by the locked mode indicator. Details of this experiment will be explained later.

5.4 Experimental results

5.4.1 Influence on the current decay time

a) Circular plasmas. Several discharges with injections of different kinds and amounts of gas into circular plasmas are compared. Fig.22 a) shows the time traces of the plasma current for three disruptions: the red curve corresponds to the discharge with an injection of 120 $mbar \cdot l$ of helium (discharge #14481), the green curve corresponds to the discharge with an injection of 80 $mbar \cdot l$ of helium (discharge #15309), and the blue curve, for comparison, corresponds to the discharge where no gas was injected (discharge #14460). An increase of the electron density prior to the disruption in the discharge #14460 suggests that the density limit was reached. The begin of each disruption in Fig.22 a), indicated by the characteristic peak in I_p signal, is shifted in time to zero. In all 3 cases, the current drop time $\Delta\tau_I$ is calculated as a time during which the plasma current falls by 90% of its pre-disruptive value. In this way, the last several milliseconds, where the current

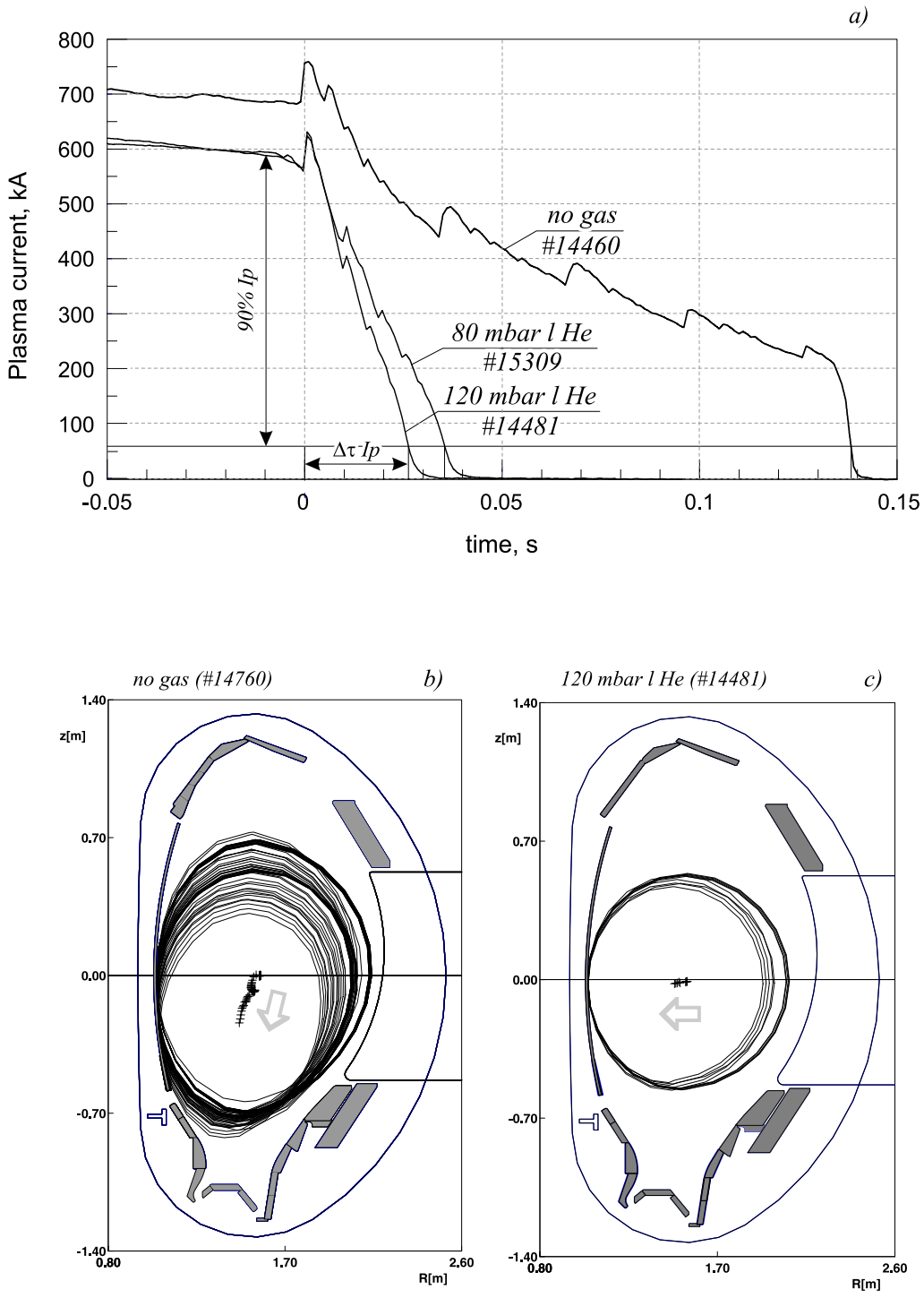

Figure 22: *a) — Decay of the plasma current after the injection of different amounts of helium: red curve — 120 mbar · l, green curve — 80 mbar · l, blue curve — no gas injected. b) — Reconstruction of the last closed magnetic surface in the discharge #14760, last reconstruction time — 53 ms after the begin of the disruption, time step is 1 ms. c) — Same as b), but for the discharge #14481, last reconstruction time — 5 ms, time step is 1 ms. Green crosses denote the geometrical center of the plasma column. Red arrows indicate the plasma motion with time.*

measurements do not seem to be correct, are excluded. At this time the measurement shows exactly the same exponential behaviour of I_p for all observed cases. The exponential curve has the time constant of 2 ms which corresponds to the resistive time constant of the wall, and the last milliseconds of the plasma current measurements may be attributed to the decay of image currents in the wall. It is seen from Fig.22 a) that there is clearly a big influence of the gas injection on $\Delta\tau_I$. In the case of the blue curve (natural density limit disruption, no gas puff) $\Delta\tau_I$ amounts to ≈ 140 ms. The edge plasma cooling by impurities in the density limit disruption results in a high edge current density gradient which destabilizes the $q = 2$ mode. The overshoots of the plasma current at $t \approx 0.035$, 0.069, 0.098 and 0.127 s are supposed to originate from the conservation of the poloidal magnetic flux during the changes in the internal plasma inductance, as it was described in Section 2. Limited amplitude capabilities of the plasma positioning feedback system does not allow it to compensate the growing plasma position deviation. The reconstruction of the last closed magnetic surface for the disruption in the discharge #14760 without a gas puff, given in Fig.22 b), shows a distinct downward motion from the start of the disruption. It is assumed that when the plasma collapses against the wall, a large amount of wall impurities is released which enhance the current decay rate. In contrast to the case of the blue curve, in the case of the red curve (large amount of helium) the current drop time amounts to 27 ms, and in the case of the green curve (low amount of helium) it amount to 36 ms, with the circular plasma column remaining (at least initially) at the inner wall in the equatorial plane (Fig.22 c), showing that the plasma positioning is still under control. It was expected that a larger amount of gas causes a faster current decay due to an enhanced plasma cooling. The experiment, however, does not show a strong dependence on the amount of the gas applied.

Similar to Fig.22 a), curves of plasma current disrupting after injections of neon and argon are shown in Fig.23. The red curve is measured in the discharge after the injection of 120 $mbar \cdot l$ of neon (discharge #14499), the green curve is measured in the discharge after the injection of 30 $mbar{\cdot}l$ of neon (discharge #15328), and the blue curve is measured after the injection of 30 $mbar \cdot l$ of argon (discharge #15447). The rate of the current fall is approximately the same for all three cases. As expected from the radiation cooling efficiency, $\Delta\tau_I$ is much shorter than in the case of helium (note the different time scale, as compared to Fig.22). The injection of a larger amount of neon (red curve) results in a slightly faster current decay compared to a smaller amount (green curve). Since the plasma resistivity $\eta \propto Z_{eff} T_e^{-3/2}$, an injection of a hifg-Z impurity should accelerate the plasma current decay due to the increase of η. In our experiments, argon with $Z = 18$ does not prove to be more effective in shortening the current decay than neon with $Z = 10$. After the gas injection, the electron temperature at the place of the contact with the gas drops and this does not allow ionization of the gas up to high states. Moderate values

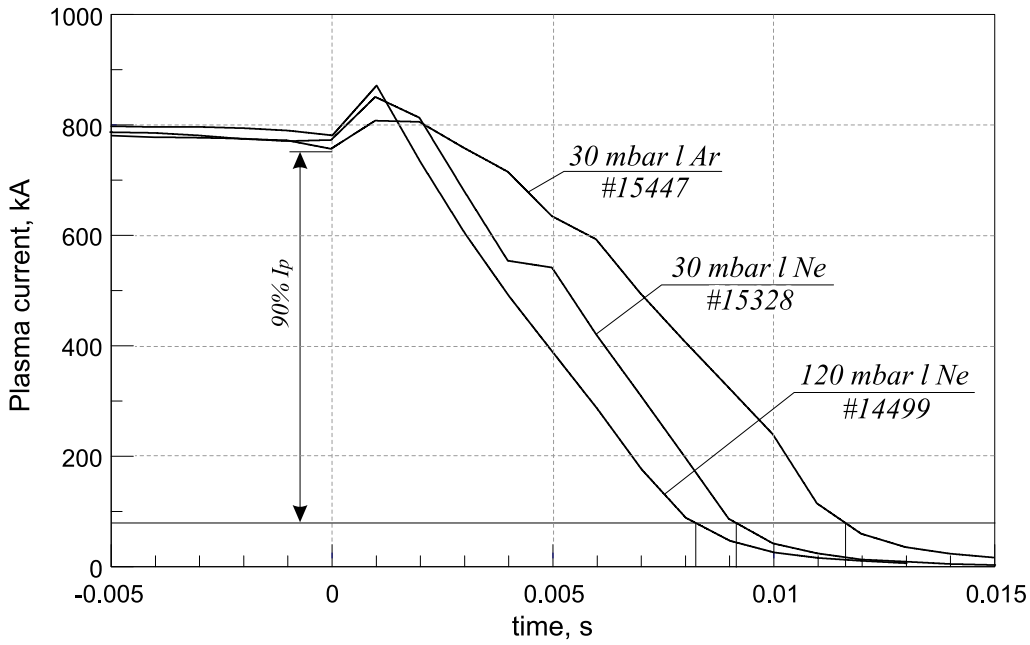

Figure 23: *Similar to Fig.22 but for neon and argon: red curve — 120 $mbar \cdot l$ of neon, green curve — 30 $mbar \cdot l$ of neon, blue curve — 30 $mbar \cdot l$ of argon. Note the different time scale as compared to Fig.22.*

of Z_{eff} for neon and argon should be expected. Another reason that argon does not accelerate the plasma current decay could be that the time of the penetration of argon into the plasma is longer, because it is by $M_{Ar}/M_{Ne} \approx 2$ times heavier than neon.

An overview of the current decay time $\Delta\tau_I$ is plotted in Fig.24 for several kinds and amounts of killer gas at different plasma currents. The disruptions occurred without gas injection are depicted by open circles. If the plasma keeps its vertical location at the equatorial plane, $\Delta\tau_I$ may amount to several hundreds of milliseconds. Higher plasma current in Fig.24 means that the disruption occurs earlier in the current ramp-down phase of the discharge and that the plasma is still partially elongated after the flat-top phase (see Fig.21). Then the vertical plasma position can be lost similar to VDE and the plasma current terminates quickly due to a crash in the divertor and the large influx of impurities from the divertor plates. Even in these cases specially marked in Fig.24 $\Delta\tau_I = 50 - 100\ ms$. Colored markers correspond to the disruptions after injections of killer gas, and in all these cases the current dissipation time is smaller, the drop being especially fast if 120 $mbar \cdot l$ of neon is used.

The delay between the time of the injection of killer gas and the begin of the disruption at different electron densities is presented in Fig.25. This time consists of two parts. The first part is the time of flight from the valve exit to the plasma, determined as the time between the start trigger for the valve and the begin of the increase of the electron density at the plasma edge. This time denoted by open circles in Fig.25 shows the expected

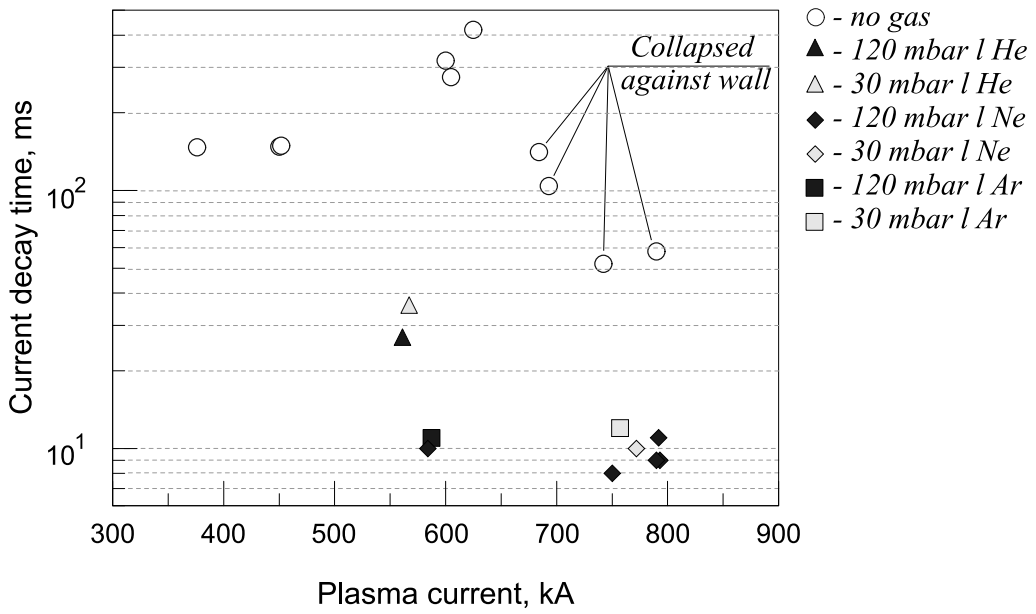

Figure 24: *Current decay time $\Delta\tau_I$ with and without killer gas puffs at different plasma currents.*

dependence on the square root of atomic mass, given by the gas sound speed

$$V_s = \sqrt{\frac{3kT}{M}}, \tag{13}$$

where k is the Boltzmann constant, T is the gas temperature and M is the mass of the gas atom. The second part corresponds to the delay between the density increase and the disruption. It will be discussed in Section 5.5. The amount of killer gas is 120 $mbar \cdot l$ in all cases. The whole delay to the disruption lies between 6 and 14 ms (closed circles in Fig.25). In the case of helium, discharges with different pre-disruptive plasma currents are taken, what may explain the scatter in the data.

b) *Elongated plasmas.* In this case no clear influence of the injection of killer gas on the current decay was found. Fig.26 a) shows three curves of the plasma current during the disruptions in elongated plasmas. The red curve is obtained after the puff of 120 $mbar \cdot l$ of neon (discharge #14503), the green curve is obtained after the puff of 120 $mbar \cdot l$ of argon (#14536), and the blue curve is obtained in the density limit without gas injection (discharge #14489). All these disruptions are followed by a downward VDE. It was decided not to use helium because of its weaker ability of the termination of a discharge. For all discharges $\Delta\tau_I$ lies around 10 ms with some differences in the behaviour of the current. It is observed that there is no usual current overshoot just prior to the beginning of the current quench phase on the red curve, although it is present in several other discharges with neon.

Fig.26 b) which is similar to Fig.25, gives the flight time of the gas and the delay to the disruption when killer gas is injected into elongated plasmas. The star in Fig.26 b)

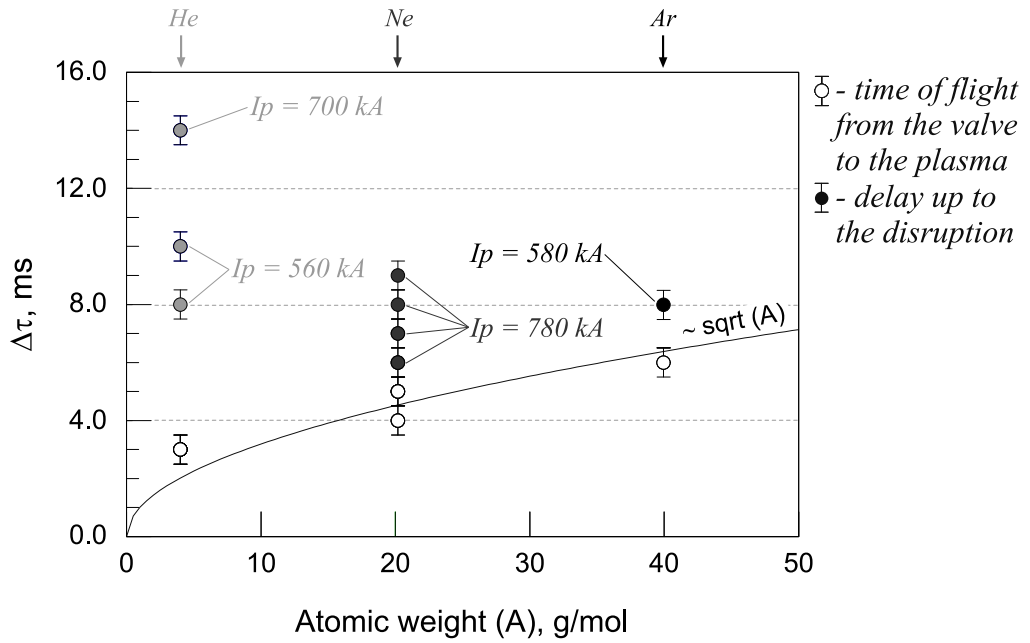

Figure 25: *Time of flight of different kinds of gas from the exit of the valve to the plasma (open circles) and the delay from the opening of the valve to the begin of a disruption (closed circles) as a function of atomic weight. The black curve corresponds to the square root from the atomic weight. The amount of gas is the same in all cases. The values of the pre-disruptive plasma current are given. The flight distance is* $\sim 2\ m$.

represents the mitigated disruption #15484. In this discharge, the plasma density is gradually raised by a slow deuterium puff until the density limit disruption starts to develop. Neon is injected into the precursor phase (see Section 5.4.3). In the other discharges in this section disruptions in stable plasmas are provoked by the injection of killer gas. After the puff into the collapsing plasma the disruption comes earlier than after puffs into stable ones. In all cases the dependence of the time of flight on the square root of atomic mass holds again.

5.4.2 Influence on halo currents and mechanical forces acting on the tokamak vessel

a) *Circular plasmas.* Halo currents in disruption of circular plasmas during the current ramp-up and ramp-down do not present a problem for ASDEX Upgrade and this part was not investigated.

b) *Elongated plasmas.* The support structures of the divertor tiles of ASDEX Upgrade are connected to the vessel through measurement resistors (shunts) which give the value of halo currents at different poloidal and toroidal locations at the inner and outer walls of the vacuum vessel. The structure of the shunt measurements is shown in Fig.27 a). The shunts are distributed not uniformly in the poloidal and toroidal directions. The halo

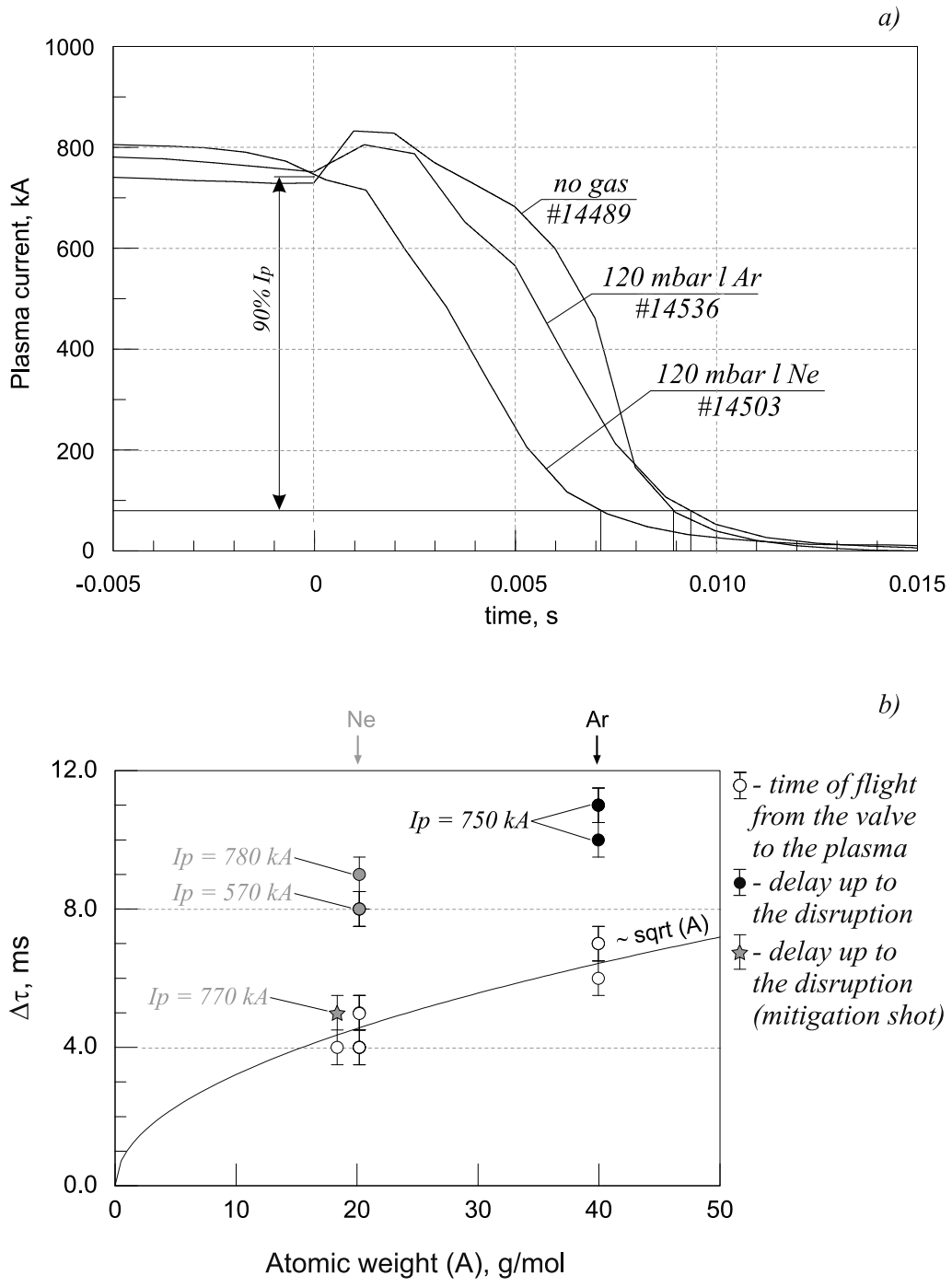

Figure 26: *a) — Decay of the plasma current in an elongated plasma: red curve — after an injection of* 120 $mbar \cdot l$ *of neon, green curve — after an injection of* 120 $mbar \cdot l$ *of argon, blue curve — no killer gas. b) — Similar to Fig.25, but for the case of elongated plasmas.*

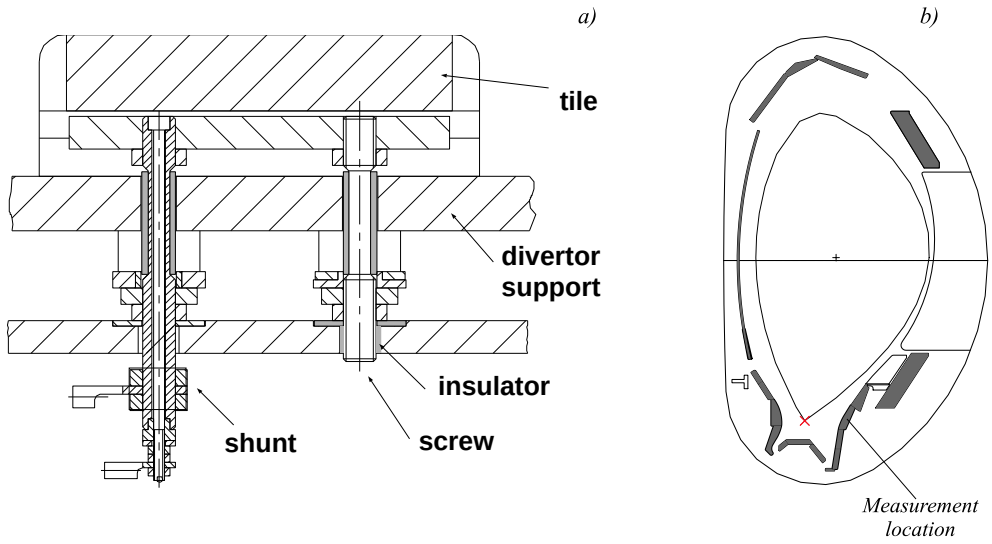

Figure 27: *Shunt measuremets of halo currents: a) — position of the shunt at the divertor tile support, b) — poloidal measurement location.*

currents which will be discussed below are measured at the poloidal location indicated in Fig.27 b), at which there are more toroidal measurement channels available.

Fig.28 shows the toroidal distribution of the halo currents in two disruptions, with and without killer gas injection. In both cases a downward VDE takes place. Halo currents induced at different toroidal locations reach a maximum simultaneously [41]. The toroidal distribution of the halo currents at their maximum in a density limit disruption (discharge #14489) is given in Fig.28 a), and the distribution of the halo currents in a disruption provoked by an injection of 120 mbar·l of neon (discharge #14503) is given in Fig.28 b). In Fig.28 a) and b), it is seen that the amplitude of the halo currents falls by a factor of 4 – 5. The measurements at the toroidal sectors 15 and 16 tend to show higher values than at the other locations, probably because of the bigger plate size collecting the halo current. The plasma current corresponding to the maximum of the halo currents (black arrows in Fig.28 a) and b) differs in both cases. Halo currents are produced when the plasma column touches the wall (see Section 2). In the case of the gas puff (discharge #14503) the plasma current by the moment of the largest halo currents is lower than in the case without gas puff (discharge #14489), which may contribute to the reduction of the halo current amplitudes.

The mechanical support of the vacuum vessel of ASDEX Upgrade is such that it is suspended by rods at eight toroidal positions. There are strain gauges built in these suspension rods. For the same discharges as above, the time traces of the mechanical load on the vessel is shown in Fig.29 a) and b). There is a clear (in average, by a factor of 3) and favourable reduction of the stresses in the mitigation case. The integral value

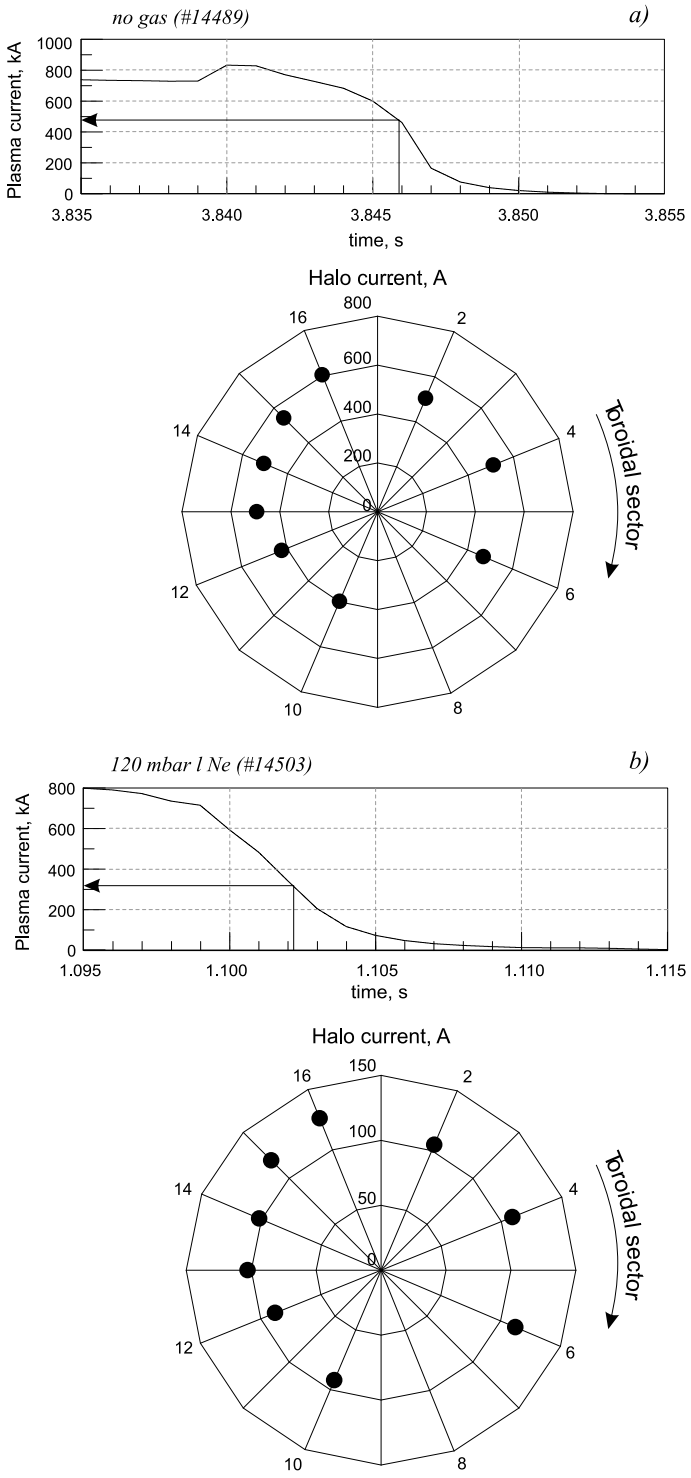

Figure 28: *Comparison of the halo currents in disruptions with and without killer gas injection. a) — Plasma current and the toroidal distribution of the maximal halo currents in a density limit disruption (discharge #14489, no gas), b) — plasma current and the toroidal distribution of the maximal halo currents in a provoked disruption (discharge #14503, 120 mbar·l of neon). Black arrows denote the times at which the toroidal distributions are plotted and the corresponding values of the plasma current. Note a different current scale in b) as compared to a).*

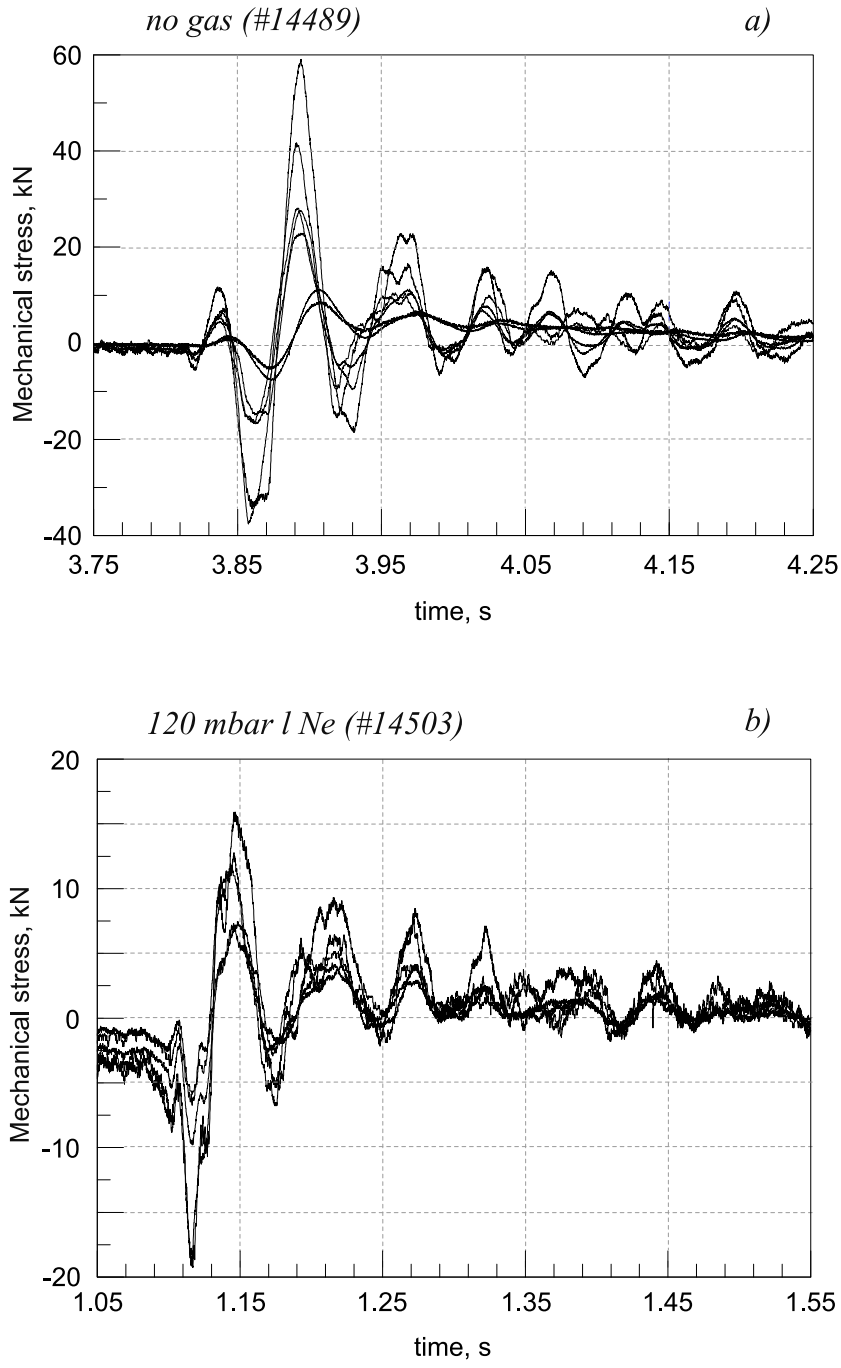

Figure 29: *Mechanical stress in the vessel suspension rods: a) — in #14489 without killer gas, b) — in #14503 with 120 mbar·l of neon. Note a different scale of stresses as compared to a).*

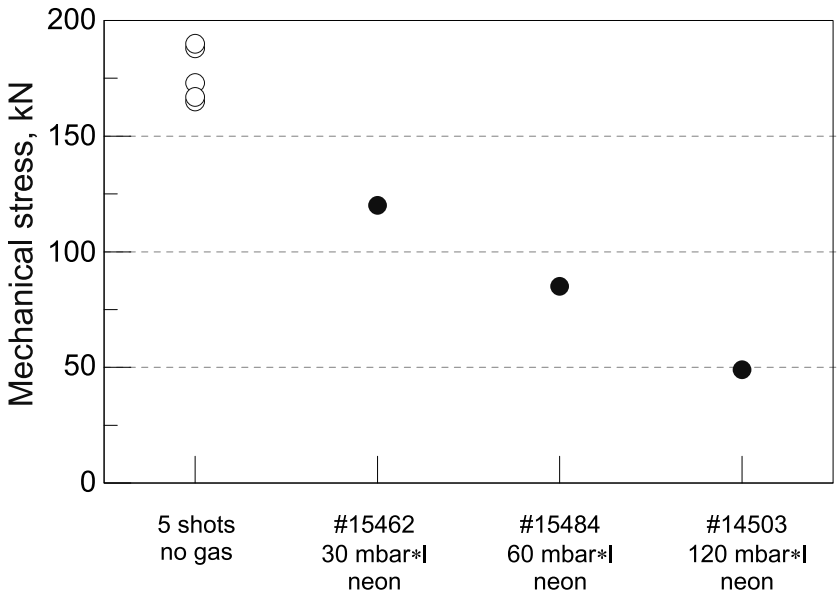

Figure 30: *Diagram showing the influence of different amounts of killer gas on the maximal mechanical force on the machine vessel.*

$\int I_{halo} dt$, which is proportional to the stresses induced, decreases only due to a lower I_{halo}, because the duration of the event does not change significantly.

Two more discharges with different amounts of injected gas were analyzed with respect to the suppression of halo currents. Fig.30 summarizes how different gas amounts influence the maximum mechanical load on the tokamak vessel. This value is obtained by taking the absolute value of the sum of all 8 strain gauge measurements:

$$\text{Maximum vertical force} = |\sum_k F_z^k|, \tag{14}$$

where F_z^k is the vertical force measured at kth toroidal position. The monotonous decay of the curve presents freedom of choosing a suitable working point, which should be a compromise between an acceptable increase of the pressure inside the vessel produced after a gas puff (see Section 5.3) and the strength of the mitigation effect.

5.4.3 Mitigation of a density limit disruption

In the experiments described above the trigger time for the gas injection is set manually. An example of a density limit disruption (discharge #15484) mitigated by a gas puff is shown in Fig.31. The density is gradually built up by a slow deuterium injection until it finally reaches the limit and a disruption becomes unavoidable. The recognition of a coming disruption is a separate complex task [39] which is not treated in these thesis. For the mitigation of a densitys limit disruption a “locked mode indicator” is used as a disruption warning signal. During the precursor phase of the disruption, perturbations of

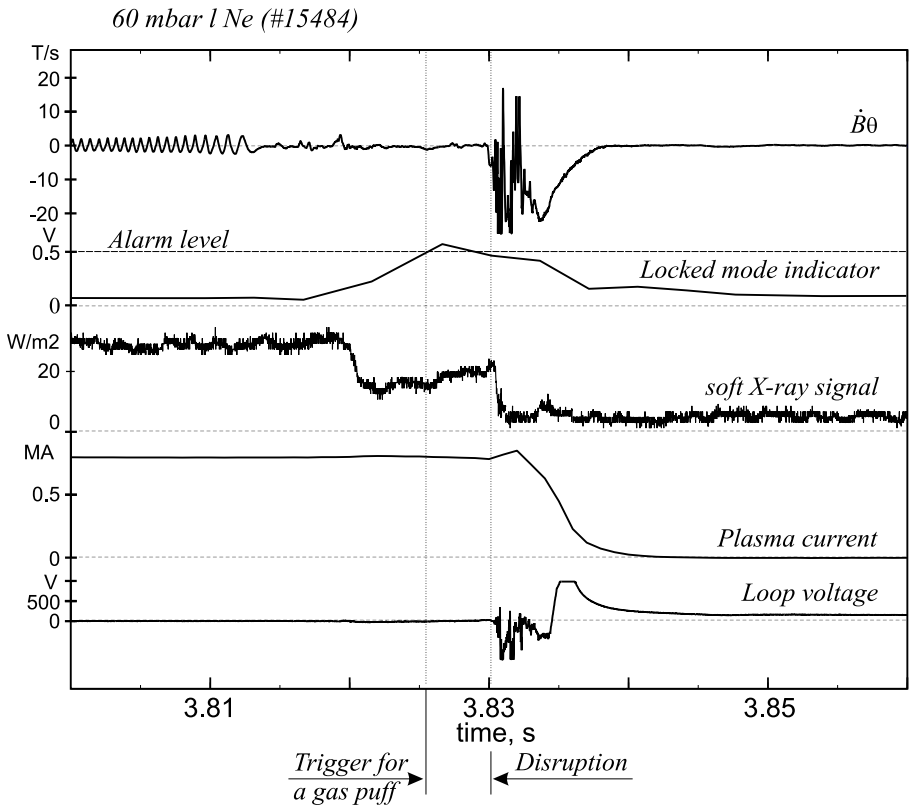

Figure 31: *An example of mitigation based on a locked mode trigger. The positive peak of the loop voltage signal (below) is in saturation at* 1000 V.

the poloidal magnetic field $\dot{B}_\theta$ due to the development of MHD modes are measured by coil arrays at different poloidal and toroidal positions and the structure of the existing modes is analyzed. When the frequency of the measured perturbation corresponding to the rotation frequency of the mode drops, the output signal of the indicator increases. The plasma starts to collapse at $t \approx 3.82\ s$, as seen from the drop in the soft X-ray signal. As the locked mode signal exceeds the pre-programmed level of 0.5 V, a trigger pulse for the gas injection is given. In this discharge the mitigation of the density limit disruption leads to the reduction of the mechanical loads by a factor of 4 compared to the reference discharge #14489 without additional gas injection (see Fig.30).

5.4.4 Concluding remarks

The reduction of heat fluxes on the divertor tiles was not investigated due to difficulties in obtaining the infrared thermography measurements of the surface temperature of the tiles.

Generation of runaway electrons was not studied systematically, but runaway electrons were not detected in most cases. Only in 4 of 27 mitigation discharges bursts of soft X-rays (from $\sim 0.5\ ms$ to milliseconds) accompanied by peaks on hard X-ray monitors appeared

at a low target plasma density ($n_e \approx 2 - 2.5 \cdot 10^{19}\ m^{-3}$) in the discharges with injections of either neon or argon, indicating runaway electron production. Runaways were not observed in disruptions after injections of helium.

Finally, it should be noted that an increase of the pressure inside the vacuum vessel after the injection of a large amount of gas can cause problems with the vacuum equipment of the tokamak (cryo-pupmps, pressure meters, ...) or affect diagnostics directly connected to the tokamak vessel. Besides, a certain amount of killer gas can be present in the machine. The retention of argon in the machine after the argon puff observed by spectroscopy was higher than the retention of helium and neon after the helium and neon puffs, respectively. However, the residual amount of gas in all 3 cases does not present a problem to start the following discharge.

5.5 Interpretation of the experimental results

It has been shown experimentally that an external massive gas puff into plasmas with a circular cross-section reduces the plasma current decay time. The injections of neon with $Z_{Ne} = 10$ and argon with $Z_{Ar} = 18$ shorten the current decay time compared to the injection of helium $Z_{He} = 2$. The injection of a larger amount of gas results in a faster current decay as compared to a smaller amount of gas.

The experimental results can be explained by the general mechanism of the density limit disruption. The gas from the valve exit is supposed to expand into the vacuum vessel at sound speed. Before the disruption, it is not clear to which extent the penetration of the gas into the plasma should be described by diffusion and to which by convection. The penetration of the gas into the plasma is accompanied by the plasma cooling due to ionization and radiation losses. In addition, the heat is exchanged between the hot plasma electrons and the electrons produced by ionization.

The time delay between the injection of the gas into the vessel and the begin of the disruption is determined by the time in which the plasma current density profile at the $q = 2$ surface is modified such that it becomes MHD unstable. This delay varies between 2 ms for neon and argon injection and 11 ms for helium injection (Fig.25, Fig.26 b) and it depends on the injection rate, inward penetration rate of the gas and its radiative cooling potential. In particular, the radiative cooling potential of helium is by a factor of 100 – 1000 lower than that of neon or argon at edge plasma temperatures of 50 – 100 eV [43] what is manifested in a larger delay in the case of helium.

During the disruption, impurity radiation seems to be important both in the energy quench and in the current quench. The increase of n_e originating from ionization of the impurity plays a positive role, intensifying the radiative losses. High levels of radiation of the order of 1 GW during the energy quench have been reported after a massive gas puff

[44]. The rise of the main chamber wall temperature due to the deposition of the radiated energy may require a proper choice of the amount of injected gas.

In order to quench the plasma's thermal energy in the plasma core, a mechanism is needed which brings the radiants deep inside the plasma at the start of a disruption. In [26], the gas jet with the mass density ρ and velocity v having the pressure $p \sim \rho v^2 \sim 30\ kPa$ enters the plasma at the volume average electron pressure $p_e = n_e k T_e \sim 7\ kPa$. The jet has been found to penetrate through the plasma at sound speed. Another fast penetration mechanism can be an enhancement of particle transport due to magnetic perturbations during a disruption. The star in Fig.26 b shows that a disruption occurs earlier when killer gas is injected in an already collapsing plasma indicating an enhanced inward penetration of the gas. Plasmas which are far from a disruption have a longer response time. The question of the importance of a rapid impurity penetration towards the plasma center for the explanation of the energy quench will be addressed in Section 7.3.1.

Due to the drop of the plasma temperature after the energy quench, the plasma resistivity is substantially increased (see Section 2.3) and the current quench starts. The rate at which the energy of the magnetic field associated with the plasma current can be dissipated and radiated determines the duration of the current decay. This, in turn, depends on the value of the post-thermal quench temperature. It will be shown in Section 7.3.2 that there exist a balance between the ohmic heating and the cooling by radiation and heat conduction. In the case of a pre-emptive gas injection the radiation power is determined by the radiative cooling rate and the amount of the gas injected. At post-thermal quench electron temperatures of $\approx 5 - 10\ eV$ helium has the lowest radiative rate compared to neon and argon. Therefore, the injection of neon or argon results in a faster plasma current decay, than the injection of helium, as it is seen from Fig.24. The idea is also supported by the results obtained with different amounts of the same gas. It is difficult to quantify the effects because of a complex correlation of the processes involved.

If a disruption occurs naturally, the impurities from the wall are released during the energy quench [45]. The release of the wall impurities acts similar to the injection of the killer gas and cools the plasma by radiation and ionization losses and dilution. However, the amount of the impurities in the plasma is smaller leading to a longer current quench.

A replacement of the wall impurities by the killer gas, which can be easily pumped out, means a lower presence of intrinsic tokamak impurities in a disruption and a better conditioning of the machine for the subsequent discharges. An indication of this was observed in the experiments carried out on ASDEX Upgrade. The effect is seen in disruptions of circular plasmas (Fig.32, b). In particular, the intensity of $C\ III$ line measured in the lower divertor region drops at some locations by a factor of ≈ 10 when helium is puffed (discharge #14481), compared with a similar disruption without any gas injection (discharge #14551), the pre-disruptive thermal energy being higher and the plasma being

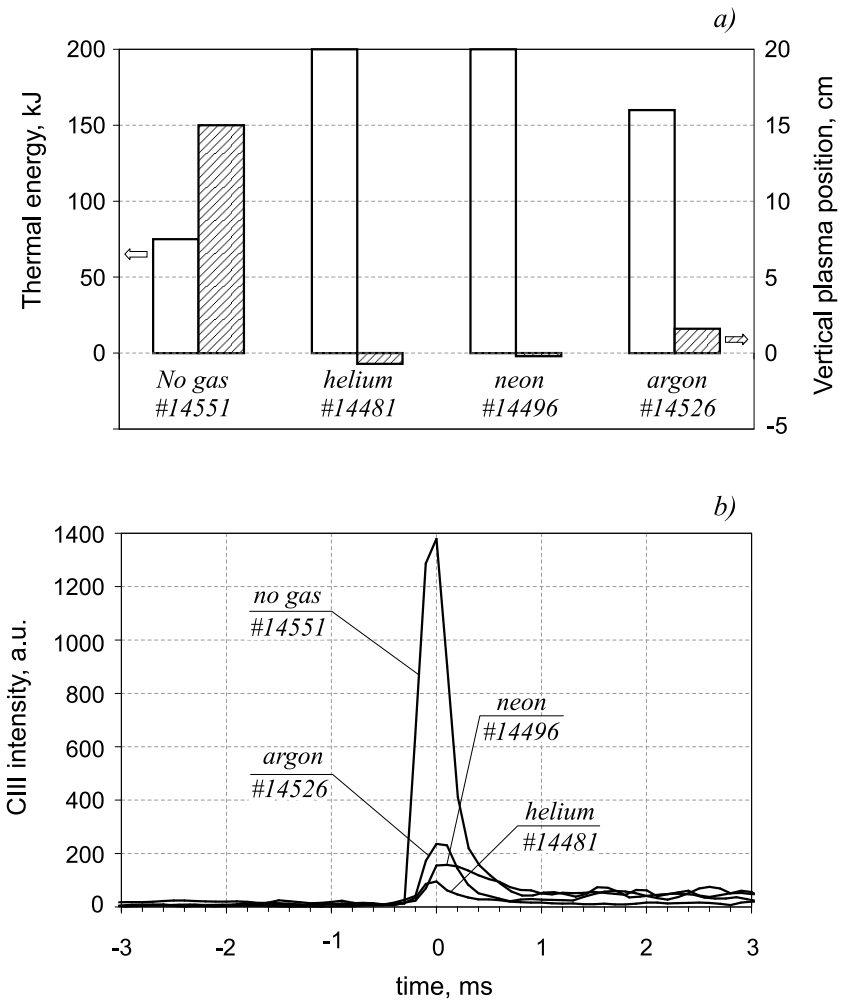

Figure 32: *Reduction of the C III intensity after a killer gas puff as compared to an unmitigated disruption. a) — thermal energy (left scale) and vertical plasma position (right scale) before the disruption, b) — time traces of C III line for the above discharges ($t = 0$ refers to the time of maximum C III emission).*

closer to the divertor in this case (Fig.32, a). A more general correlation between the intensity of the $CIII$ line which represents the carbon content in the plasma and the duration of the current quench is shown in table 5. This is, in fact, the correlation between the impurity content in the plasma (including carbon represented by the $CIII$ line intensity) and the duration of the current quench. If the amount of impurities in a disrupting plasma (either carbon and oxygen from the walls or killer gas externally injected) is high, the disruption will be fast. Inversely, it is seen that the contents of wall impurities is low after mitigated disruptions with the reduced current decay.

The shortening of current decay is not observed in disruptions of elongated plasmas. Here the feedback system cannot keep the plasma column at the neutral point where the forces in the vertical direction are balanced. Once the position control fails, the full

Discharge Nr.	*Killer gas*	*CIII line intensity*	*Duration of the current quench, ms*
#14460	no	low	150
#14551	no	high	55
#14481	He	low	30
#14496	Ne	low	10
#14460	Ar	low	10

Table 5: *Correlation between the impurity content in the plasma (including carbon represented by the CIII line intensity) and the duration of the current quench.*

column moves either up- or downwards, depending, in particular, on the starting position of the plasma column with respect to the neutral point. The time scale of the vertical displacement event is typically $\sim 10ms$, what is comparable to the time of the current decay obtained in the experiments with an injection of a heavy gas. In this case, the VDE is too fast for the gas to develop its full influence.

It was explained in Section 5.2 that a fast termination of the plasma current in a VDE is suggested to minimize the induction of halo currents. Despite the absence of the reduction of the current decay time, the induction of halo currents and mechanical loads of the vessel are mitigated in our experiments by a factor of 4. This suggests an other mechanism of the mitigation effect. Halo currents flow partially in the halo region of the plasma and partially in the vessel's wall. After the puff, the gas expands in the vacuum chamber and produces a cold and resistive plasma at the wall. The region occupied by this cold plasma includes also the halo region (see Fig.5). Due to the high resistivity of the halo region, the diffusion rate of the magnetic field from the plasma is increased and the magnetic flux changes without inducing compensation currents.

6 MODELING OF THE PLASMA BEHAVIOUR AFTER A LARGE GAS INJECTION

As was described previously, several attempts of modeling disruptions have been undertaken. The treatment of a disruption was to a large degree simplified. A new alternative of simulating the gas injection into a tokamak plasma is proposed here. Its main extension is that particle and heat transport are treated in a 1-D case compared to previous 0-D calculations.

6.1 Model description

The model is based on fluid equations in a cylindrical geometry. Cylindrical geometry assumes a large aspect ratio tokamak neglecting the toroidicity of the plasma. Three plasma species, which are the background plasma ions, ions of a single impurity species and electrons, are treated separately.

6.1.1 Background ions

The term 'background ions' is used for the ions of which the plasma is constituted. The evolution of the ion density n_H is given by the continuity equation:

$$\frac{\partial n_H}{\partial t} + \frac{1}{r}\frac{\partial}{\partial r}\left(r\Gamma_{\perp H}\right) = 0. \tag{15}$$

The diffusion equation for the particle flux perpendicular to the magnetic field, $\Gamma_{\perp H}$

$$\Gamma_{\perp H} = -D_{\perp H}\frac{\partial n_H}{\partial r} + V_{\perp H} n_H \tag{16}$$

contains both a diffusive and a convective part.

The time evolution of the ion temperature T_H is computed from the energy balance equation

$$\frac{3}{2}\frac{\partial n_H T_H}{\partial t} + \frac{1}{r}\frac{\partial}{\partial r}[r(\frac{3}{2}\Gamma_{\perp H} T_H - \chi_{\perp H}\frac{\partial T_H}{\partial r})] = P_{eH} - P_{ii}, \tag{17}$$

$\chi_{\perp H}$ being the perpendicular ion thermal conductivity. The terms which appear in Eq.17 on the right-hand side are values per volume unit. They account for the collisional heat exchange between the electrons and background ions (P_{eH}), and between the initially hot background ions and the cold impurity fraction (P_{ii}),

$$P_{eH} = \frac{3}{2} n_H \frac{T_e - T_H}{\tau_{ex,eH}}, \tag{18}$$

$$P_{ii} = \sum \frac{3}{2} n_z^j \frac{T_H - T_i^j}{\tau_{ex,ii}^j}, \tag{19}$$

where T_e is the electron temperature, T_i^j is the temperature of a jth impurity component n_z^j. Each kind of collisions is characterized by its own heat exchange time [2]

$$\tau_{ex,eH} = \frac{m_H}{2m_e}\tau_{eH}, \tag{20}$$

$$\tau_{ex,ii}^j = \frac{m_z}{2m_H}\tau_{ii}^j, \tag{21}$$

where m_e, m_H, m_z are the electron, background ion and impurity atom masses, respectively. Different values of τ on the right sides of Eqs.20 and 21 correspond to the electron-background ion and background ion-impurity ion collisions.

The model has been adapted to the experiments with circular plasmas in the current ramp-down phase of ASDEX Upgrade discharges. During this time, additional heating sources are not present and therefore not included in the right-hand side of Eq.17. Ohmic heating contributes directly to the electron temperature and is then transferred to the ions by the P_{eH} term.

Transport coefficients $D_{\perp H}$ and $V_{\perp H}$ are determined such that they satisfy the ambipolarity condition

$$\Gamma_{\perp H} + \sum \Gamma_{\perp z}^j = \Gamma_{\perp e} \tag{22}$$

and quasi-neutrality condition

$$n_{\perp H} + \sum n_{\perp z}^j = n_{\perp e}, \tag{23}$$

where $\Gamma_{\perp z}^j$, $\Gamma_{\perp e}$ are fluxes of the impurity ions and electrons, respectively (see subsections below). The choice of the value of the thermal conductivity will be described in Section 7.1.

6.1.2 Impurity fraction

The continuity equation for an impurity charge state n_z^j has the form:

$$\frac{\partial n_z^j}{\partial t} + \frac{1}{r}\frac{\partial}{\partial r}(r\Gamma_{\perp z}^j) = S_z^j, \tag{24}$$

S_z^j being the rate at which the jth impurity population is changed due to ionization and recombination,

$$S_z^j = n_e(n_z^{j-1}\langle\sigma v\rangle_{ion}^{j-1} - n_z^j\langle\sigma v\rangle_{ion}^j + n_z^{j+1}\langle\sigma v\rangle_{rec}^{j+1} - n_z^j\langle\sigma v\rangle_{rec}^j), \tag{25}$$

$\langle\sigma v\rangle_{ion,rec}^j$ are T_e-dependent Maxwell-averaged cross-sections of ionization and radiative recombination for the jth component. The values are extracted from the atomic database ADAS [46]. The dependence of the cross-sections on n_e is ignored. For neutrals and fully ionized species, Eq.25 takes the form

$$S_z^0 = n_e(-n_z^0\langle\sigma v\rangle_{ion}^0 + n_z^1\langle\sigma v\rangle_{rec}^1) + Q_{puff}, \tag{26}$$

$$S_z^Z = n_e(n_z^{Z-1}\langle\sigma v\rangle_{ion}^{Z-1} - n_z^Z\langle\sigma v\rangle_{rec}^Z), \tag{27}$$

where Z is the impurity charge and Q_{puff} describes the rate of the injection of neutrals at the edge.

The calculation of T_i^j results from the energy balance for the impurity ions

$$\frac{3}{2}\frac{\partial n_z^j T_i^j}{\partial t} + \frac{1}{r}\frac{\partial}{\partial r}[r(\frac{3}{2}\Gamma_{\perp z}^j T_i^j - \chi_{\perp z}^j\frac{\partial T_i^j}{\partial r})] = P_{ii}, \tag{28}$$

where the contribution of the electron-impurity ion collisions is neglected due to a big difference in masses of the colliding particles.

Both of transport coefficients, $D_{\perp z}^j$ and $V_{\perp z}^j$, can adopt any value, different for different ionization states. The choice of the values for $D_{\perp z}^j$, $V_{\perp z}^j$ and $\chi_{\perp z}^j$ will be described in Section 7.1. The diffusion coefficient for the neutral component is put to zero, and the neutrals are introduced into the plasma by a convective flow at the sound speed, which is justified if a gas at a pressure of several bars is injected into vacuum.

6.1.3 Electrons

The continuity equation for electrons

$$\frac{\partial n_e}{\partial t} + \frac{1}{r}\frac{\partial}{\partial r}(r\Gamma_{\perp e}) = S_e, \tag{29}$$

and the electron flux

$$\Gamma_{\perp e} = -D_{\perp e}\frac{\partial n_e}{\partial r} + V_{\perp e}n_e, \tag{30}$$

are similar to those of the ions. Here S_e is a source of electrons released through ionization of impurities injected, $S_e = \sum jS_z^j$, where S_z^j is the rate at which the jth charge state appears. The computation of S_z^j is explained above in subsection 'Injected impurity'.

The electron temperature is inferred from the conservation of energy

$$\frac{3}{2}\frac{\partial n_e T_e}{\partial t} + \frac{1}{r}\frac{\partial}{\partial r}[r(\frac{3}{2}\Gamma_{\perp e}T_e - \chi_{\perp e}\frac{\partial T_e}{\partial r})] = P_{oh} - P_{line} - P_{br} - P_{ion} - P_{eH}, \tag{31}$$

where $\chi_{\perp e}$ is the transverse electron heat conductivity, P_{oh} is the ohmic heating power, P_{line} is the impurity radiation power, P_{br} is the bremsstrahlung power, P_{ion} is the ionization power. The ohmic heating is calculated by

$$P_{oh} = \eta j_p^2, \tag{32}$$

where j_p is the plasma current density and η is the Spitzer resistivity [2]

$$\eta = 1.65\cdot 10^{-9}\ln\Lambda Z_{eff}/T_e^{3/2}\ \text{ohm·m}, \tag{33}$$

T_e in keV, $\ln\Lambda$ is the Coulomb logarithm put equal to 15 as it is usually taken in calculations. Radiation losses are $P_{line} = n_e n_z L_z$, with L_z being the radiation rate coefficient for a given impurity [47]. Bremsstrahlung losses are evaluated from [2]

$$P_{br} = 5.35\cdot 10^{-37}{Z_{eff}}^2 n_e n_z T_e^{1/2}\ \text{W}\cdot\ \text{m}^{-3}, \tag{34}$$

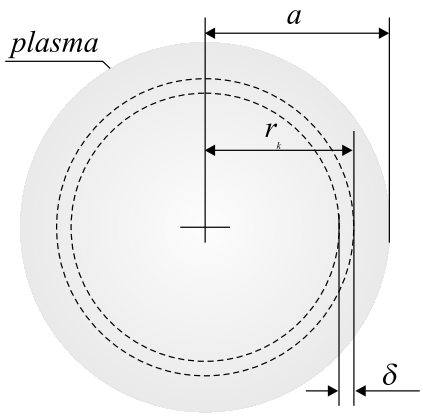

Figure 33: *To the calculation of the total plasma resistance. The poloidal plasma cross-section is divided on concentric layers, the resistivity η_k of each of them being determined by the local value of T_e.*

T_e in keV. Z_{eff} is the effective plasma charge. The power of bremsstrahlung is negligible under the conditions considered in the model. The electron energy spent for ionization is expressed by $P_{ion} = \sum E^j_{ion} S^j_z$, E^j_{ion} being the energy needed to bring an ion from the $(j-1)$st to jth ionization state (only single ionizations from neighbouring states are considered).

The values of $D_{\perp e}$, $V_{\perp e}$ and $\chi_{\perp e}$ are determined in Section 7.1.

6.1.4 Plasma current

The decay of the plasma current is derived from the equation

$$\frac{dI_p}{dt} = -\frac{I_p}{\tau}. \tag{35}$$

The diffusion of the poloidal magnetic field in the plasma is represented approximately by the decay time constant

$$\tau = \frac{R_p}{L_p}, \tag{36}$$

R_p being the overall plasma resistance and L_p is the plasma inductance. To calculate the resistance of the plasma column with a non-uniform T_e-distribution, it is divided on thin cylindrical layers of width δ (Fig.33). The resistance of each of them becomes

$$R_k = \eta_k \frac{2\pi R_0}{\pi[r_k^2 - (r_k - \delta)^2]}, \tag{37}$$

where R_0 is the major radius of the tokamak, r_k denotes the radial position and η_k is the T_e-dependent resistivity (Eq.33) at $r = r_k$. The total plasma resistance is equivalent to a circuit of parallel conductors:

$$\frac{1}{R_p} = \sum \frac{1}{R_k}. \tag{38}$$

The plasma inductance is calculated using the formula [2]

$$L_p = \mu_0 R_0 \left[\ln\left(\frac{8R_0}{a}\right) - 2 + \frac{l_i}{2} \right], \tag{39}$$

where $\mu_0 = 4\pi \cdot 10^{-7}\ H/m$, l_i is the plasma internal inductance. l_i depends on the current density profile and may change during a disruption, but, for simplicity, this effect is not taken into account here and L_p is kept constant throughout the calculation.

The toroidal current density is rearranged at every time step and is derived from the Ohm's law for each cylindrical layer (see Fig.33).

$$j_p = \frac{E_{tor}}{\eta} = \frac{U_{loop}}{2\pi R_0 \eta}, \tag{40}$$

where E_{tor} is the toroidal electric field, U_{loop} is the loop voltage,

$$U_{loop} = -L_p \frac{dI_p}{dt}. \tag{41}$$

The term $\mathbf{v}\times\mathbf{B}$ in the generalized Ohm's law $\mathbf{E}+\mathbf{v}\times\mathbf{B} = \eta\mathbf{j}$ is neglected. The loop voltage given in Eq.41 is taken to be constant over the whole radial calculation domain. At the plasma current decay time of 10 ms, the electron temperature during the current decay of 10 eV and $Z_{eff} = 3$, the depth of the penetration of the electric field into the plasma is $\approx 45\ cm$ which is almost equal to the plasma size. The assumption of the constant U_{loop} may be not justified during the energy quench time of $\sim 100\ \mu s$ and the value of j_p close to the center given by Eq.40 may be too large. However, j_p is used only to evaluate the ohmic heating power in the energy balance (Eq.31) in which the heat conduction and electron flux terms are supposed to exceed by far the ohmic heating during the energy quench. The choice of the electron heat conductivity and diffusion coefficient will be described in Section 7.1. The part in U_{loop} which drives the plasma current by the change of the magnetic flux of the tokamak's primary winding is typically about one volt in the flat-top phase, and it is negligible compared to the high decay rate of I_p in a disruption, amounting to $\sim 10\ MA/s$ at a plasma inductance of several μH.

Substituting Eq.36 in Eq.35 the loop voltage is written as

$$U_{loop} = \frac{L_p}{\tau} I_p = I_p R_p, \tag{42}$$

if one neglects for simplicity the derivative $d\tau/dt$. It will be shown in Section 7.3.2 that the plasma temperature stays almost constant during the current quench and, together with the assumption of the unchanged L_p, the decay rate τ does not change in time.

The schematic in Fig.34 summarizes the correlations between the different plasma parameters used in the model.

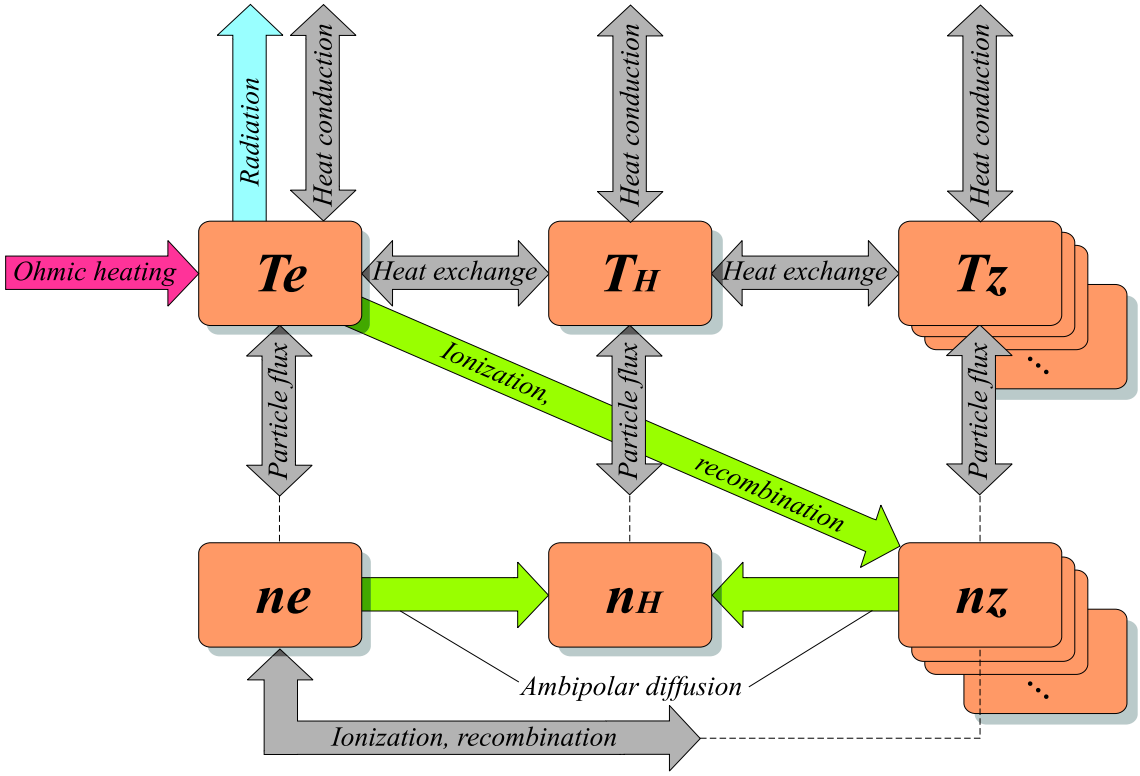

Figure 34: *Correlations between the different plasma parameters used in the model. Red arrow increases the parameter considered, blue — decreases, gray can both increase and decrease, green arrow describes an indirect dependence.*

6.2 Numerical solver

6.2.1 Finite volumes approach with the upwind scheme and the recursion method

A combined advection-diffusion equation is taken for a cylindrical geometry in a generalized form

$$\frac{\partial}{\partial t}k_1 v u + \frac{1}{r}\frac{\partial}{\partial r}\left[r\left(k_2\Gamma u - \chi\frac{\partial u}{\partial r}\right)\right] = Q, \tag{43}$$

where $k_{1,2} = \text{const}$. Such a form allows equations for both density and temperature to be solved. Choosing $k_1 = k_2 = v \equiv 1$, $u \equiv n$, $\Gamma \equiv V_\perp$, $\chi \equiv D_\perp$ the continuity and diffusion equations (Eq.29, 24) are obtained, while setting $k_1 = k_2 \equiv 3/2$, $v \equiv n$, $u \equiv T$, $\Gamma \equiv \Gamma_\perp$, $\chi \equiv \chi_\perp$ describes the energy balance equations (Eq.31, 17, 28).

Differentiation of Eq.43 and combining terms gives

$$\frac{\partial}{\partial t}k_1 v u + \frac{\partial}{\partial r}\left(k_2\Gamma u - \chi\frac{\partial u}{\partial r}\right) = Q - \frac{1}{r}\left(k_2\Gamma u - \chi\frac{\partial u}{\partial r}\right). \tag{44}$$

Eq.44 is discretized on a radial grid r_i with the discretization step Δr and then integrated over a cell of the length Δr embracing r_i between the west point r_w and the east point r_e (Fig.35). This approach is called *finite volumes* method and it reflects the balance between

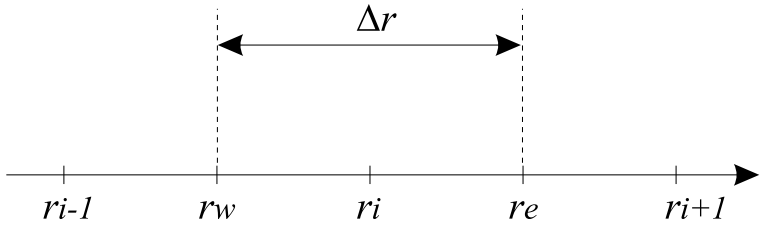

Figure 35: *Radial discretization grid used in the model.*

the fluxes through the borders and the sources inside the area considered. It reduces the differential order of Eq.43 to the first degree making the calculation easier, while the second common approach, *finite differences* method, just approximates all derivatives by their difference analogues keeping the second differential order of the equation.

Integrating Eq.44 and building a fully implicit scheme one obtains

$$k_1\frac{(vu)_i-(vu)_i^0}{\Delta t}\Delta r+(k_2\Gamma u)_e-\left(\chi\frac{\partial u}{\partial r}\right)_e-(k_2\Gamma u)_w+\left(\chi\frac{\partial u}{\partial r}\right)_w=$$

$$=Q_i\Delta r-\frac{1}{r_i}\left((k_2\Gamma u)_i-\left(\chi\frac{\partial u}{\partial r}\right)_i\right)\Delta r, \tag{45}$$

where the subscript 0 denotes the values from the previous iteration step, and the term $1/r_i\ldots$, for simplicity, is supposed to be constant in the integration region around r_i. If Eq.43 is taken as a heat diffusion equation ($v\equiv n_e$), the first term on the left-hand side in Eq.45 means that the temperature equilibration due to a change in n_e (dilution) must occur within a single calculation time step.

The discretization of the radial derivatives gives

$$\left(\chi\frac{\partial u}{\partial r}\right)_e=\chi_e\frac{u_{i+1}-u_i}{\Delta r},\ \left(\chi\frac{\partial u}{\partial r}\right)_w=\chi_w\frac{u_i-u_{i-1}}{\Delta r}. \tag{46}$$

χ_e, χ_w can be averaged in several ways, for example, as

$$\chi_e=2\left(\frac{1}{\chi_i}+\frac{1}{\chi_{i+1}}\right)^{-1},\ \chi_w=2\left(\frac{1}{\chi_{i-1}}+\frac{1}{\chi_i}\right)^{-1}, \tag{47}$$

producing results which are numerically more stable.

The presence of a convective term Γu in Eq.43 complicates the numerical solution, because in this case it is subject to numerical instabilities. The *upwind* scheme is used here to handle these uncomfortable terms. For the calculation of the term $(\Gamma u)_e$ in Eq.43 the value of $\Gamma_e=\Gamma(r_e)$ and either u_i or u_{i+1} are taken depending on the Γ_e. If $\Gamma_e>0$ that is the particles flow from the left to the right, u_i is chosen. Otherwise, u_{i+1} is used. The term $(\Gamma u)_w$ is treated in the similar way and the upwind scheme produces

$$(\Gamma u)_e=\max(\Gamma_e,0)u_i-\max(-\Gamma_e,0)u_{i+1},$$

$$(\Gamma u)_w = \max(\Gamma_w, 0)u_{i-1} - \max(-\Gamma_e, 0)u_i. \tag{48}$$

The intermediate values Γ_e, Γ_w can be also approximated by several methods, for instance, as an arithmetic mean. Substituting Eq.46 and Eq.48 in Eq.45 forms a set of linear equations

$$a_{ki-1}u_{i-1} + a_{ki}u_i + a_{ki+1}u_{i+1} = v_i^0 u_i^0 + Q_i\Delta t, \tag{49}$$

where the coefficients are

$$\begin{aligned} a_{ki-1} &= -\chi_w\frac{\Delta t}{\Delta r^2} + \frac{1}{r_i}\chi_i\frac{\Delta t}{2\Delta r} - k_2\max(\Gamma_w, 0)\frac{\Delta t}{\Delta r}, \\ a_{ki} &= k_1 v_i + (\chi_e + \chi_w)\frac{\Delta t}{\Delta r^2} + \frac{k_2}{r_i}\Gamma_i\Delta t + k_2\left[\max(-\Gamma_w, 0) + \max(\Gamma_e, 0)\right]\frac{\Delta t}{\Delta r}, \\ a_{ki+1} &= -\chi_e\frac{\Delta t}{\Delta r^2} - \frac{1}{r_i}\chi_i\frac{\Delta t}{2\Delta r} - k_2\max(-\Gamma_e, 0)\frac{\Delta t}{\Delta r}. \end{aligned} \tag{50}$$

These coefficients constitute a matrix which contain only 3 elements surrounding the diagonal terms (so-called *tridiagonal* matrices). The recursion method is used for the solution of the system Eq.49, Eq.50. The recursion method treats the system of N equations $\mathbf{A}x = \mathbf{B}$, with $\mathbf{A}$ being tridiagonal:

$$\mathbf{A} = \begin{pmatrix} \beta_1 & \gamma_1 & 0 & . & . & 0 \\ \alpha_2 & \beta_2 & \gamma_2 & 0 & . & 0 \\ 0 & \alpha_3 & \beta_3 & \gamma_3 & 0 & . \\ . & . & . & . & . & . \\ . & . & . & \alpha_{N-1} & \beta_{N-1} & \gamma_{N-1} \\ . & . & . & 0 & \alpha_N & \beta_N \end{pmatrix}. \tag{51}$$

Then by introducing auxiliary variables g_i and h_i by

$$x_{i+1} = g_i x_i + h_i \ (i = 1, \ldots, N-1) \tag{52}$$

the 'downward' recursion is found:

$$g_{N-1} = \frac{-\alpha_N}{\beta_N}, \ h_{N-1} = \frac{b_N}{\beta_N}, \tag{53}$$

$$g_{i-1} = \frac{-\alpha_i}{\beta_i + \gamma_i g_i}, \ h_{i-1} = \frac{b_i - \gamma_i h_i}{\beta_i + \gamma_i g_i} \ (i = N-1, \ldots, 2). \tag{54}$$

After arriving at g_1 and h_1 the variable x_1 can be found:

$$x_1 = \frac{b_1 - \gamma_1 h_1}{\beta_1 + \gamma_1 g_1} \tag{55}$$

and then the known values g_i, h_i are inserted in the 'upward' recursion given by Eq.52.

For the application in the disruption model, all algorithms considered above have been implemented in the programming language 'C'.

6.2.2 Boundary conditions

The boundary conditions for the calculation are chosen in the following way. All profiles are assumed to be symmetric with respect to the axis $r = 0$, meaning that the derivatives of the densities and temperatures are equal to zero at the center. The Shafranov shift which is a toroidal geometry effect is not taken into account in the cylindrical model. It depends on the plasma β and amounts typically to 5 – 10 cm, what is negligible compared to the minor radius of 0.5 m.

At the plasma edge ($r = a$) T_e and T_H are kept equal to 2 eV, n_e and n_H are equal to 10^{18} m^{-3} and $n_z = 0$. The temperature of 2 eV is assumed to be equal to 0 compared to pre-disruptive temperatures of ~ 1 keV and the physics below 2 eV is not considered.

6.3 Tests of the numerical code

Two test runs of the code were made. In one of them, the solution of the advection-diffusion equation was verified. In the second, the treatment of the atomic data for neon was checked.

6.3.1 Test of the advection-diffusion equation solver

To test the performance of the solver, a combined plane advection-diffusion equation in the form

$$\frac{\partial f}{\partial t} = \frac{\partial}{\partial x}\left(kxf\right) + \frac{1}{2}\frac{\partial^2}{\partial x^2}(Df) \tag{56}$$

is considered. It has a known analytical solution. If one starts with a Gauß function

$$f(x,0) = \frac{1}{2\pi\Omega_0}\exp^{-\frac{x^2}{2\Omega_0}} \tag{57}$$

within a region $[-a, a]$, then the diffusion tries to broaden the initial profile, while the advection works in the opposite direction. As a result, the solution is expressed as

$$f(x,t) = \frac{1}{2\pi\Omega}\exp^{-\frac{x^2}{2\Omega}} \tag{58}$$

with

$$\Omega = \Omega_0\exp^{-2kt} + \frac{D}{2k}(1 - \exp^{-2kt}). \tag{59}$$

The comparison between the analytical solution for $k = 3$, $D = 2$, $\Omega_0 = 0.1$, $-5 \leq x \leq 5$, $0 \leq t \leq 0.5$, and that delivered by the code with $\Delta r = 0.05$, $\Delta t = 0.01$ is shown in Fig.36 a). The boundary conditions are taken as $f = 0$ for $x = \pm 5$. In the calculation a transition from a cylindrical to a plane geometry is realized by considering the problem at the large major radius $R = 100$ $m \gg a = 5$ m (see Fig.1). A seen in Fig.36 a), the analytical solution and the numerical calculation agree very well.

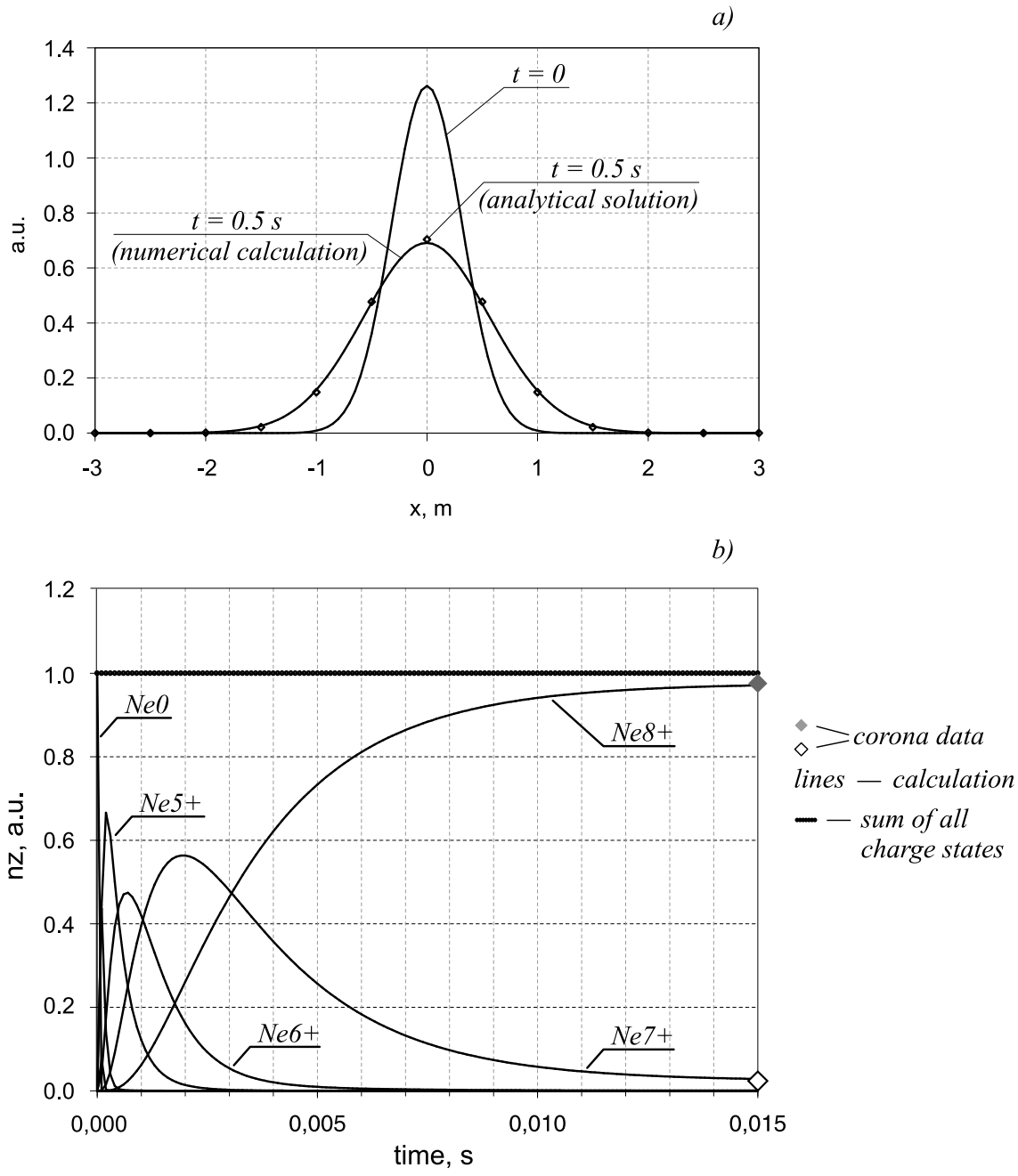

Figure 36: *Verification of the results produced by the code. a) — comparison of the evolution of an advection-diffusion system with the analytical solution, b) — time development of different charge states of neon reaching the corona equilibrium.*

6.3.2 Evolution of the charge states of the impurity

In another test, the treatment of ionization and recombination of impurity in the case of neon is verified. For this, neutrals of unit density are introduced into a plasma with $n_e = 10^{19}\ m^{-3}$ and $T_e = 100\ eV$. If the temperature and the number of particles are kept constant the impurity charge state populations must reach the corona equilibrium [43]. The time evolution of different ionization states n_z^j is presented in Fig.36, b). After some changes at the beginning, the system comes to an equilibrium where essentially only 2 states are present, as prescribed by the corona equilibrium. The thick black line in Fig.36 b) indicates the sum of all charge states.

7 CALCULATION RESULTS

7.1 Disruption calculation scenario

For the modeling, the disruption in the discharge #14499 from the experimental program on ASDEX Upgrade is chosen. The investigation of the electron temperature collapse after the gas puff which could be compared to experimental observations is of main interest. The following set of parameters is adopted in the calculation (Table 6). The disruption

Major plasma radius	$1.65\ m$
Radial calculation region	from $a_0 = 0.05$ to $a = 0.5\ m$
Radial calculation step	$0.05\ m$
Original plasma	hydrogen
Pre-disruptive plasma current	$850\ kA$
Pre-disruptive plasma temperature	$T_e = T_H = 1\ keV \cdot (1 - (r/a)^2)^2$
Pre-disruptive plasma density	$n_e = n_H = 10^{19}\ m^{-3} \cdot (1 - (r/a)^2)$
Injected gas	neon, $120\ mbar \cdot l$ in $3\ ms$

Table 6: *Set of parameters used for the calculation.*

calculation scenario is divided into three stages (Fig.37).

On the stage 1 from $t_0 = -0.5\ ms$ to $t = 0$, the injection of neon atoms at $r = 0.5\ m$ with the sound speed of neon $c_s = 435\ m/s$ starts. When travelling inside the plasma, the neutrals are ionized, and it is supposed that the fraction which is not ionized continues to move with the sound speed, as reported in [26, 27]. The particle transport on the stage 1 is assumed to be anomalous. It is known that the transport coefficients observed in tokamak experiments exceed teh diffusion caused by binary Coulumb collisions by more than an order of magnitude. In the tokamak magnetic field geometry this is called *neoclassical* diffusion. Therefore, both $D_{\perp e}$ and $D_{\perp z}$ are put equal to $1\ m^2/s$ [51, 52]. The value of the electron thermal conductivity $\chi_{\perp e}$ is chosen such as to conduct the energy of the ohmic heating in the absence of the injected gas to the wall, keeping the electron temperature constant. This leads to $\chi_{\perp e} = 10^{20}\ m^{-1}s^{-1}$ (the units are such that the energy flux $q[\frac{eV}{m^2 s}] = \chi \frac{\partial T[eV]}{\partial r}$). For simplicity, ion thermal conductivities $\chi_{\perp H}$ and $\chi_{\perp z}$ are taken to be equal to $\chi_{\perp e}$ due to lack of information about the anomalous ion heat transport.

The disruption is prescribed to occur on the stage 2 at $t = 0$ (energy quench). This moment is determined heuristically. According to our view, when the electron temperature drops over a substantial radial region including the $q = 2$ surface, the contracting plasma current density profile must pass an MHD unstable shape, which causes the disruption. It

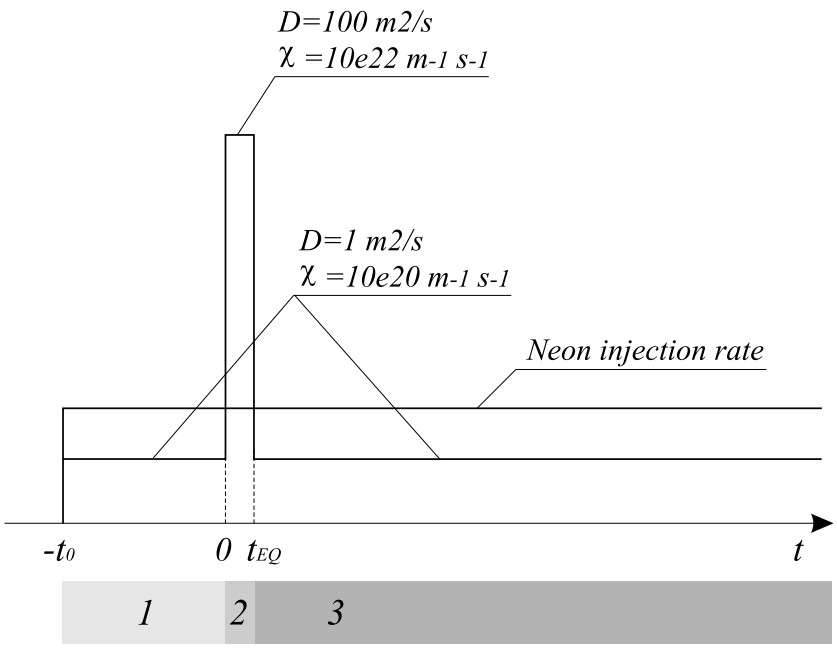

Figure 37: *Three stages of the disruption calculation (numbers below): 1 — delay to the energy quench, 2 — energy quench, 3 — current quench. The duration of the energy quench is exaggerated.*

has not been found out so far which transport mechanism is dominant during a disruption. For simplicity, we assume it to be pure diffusive and increase the diffusion coefficients up to $D_{\perp e} = D_{\perp z} = 100\ m^2/s$, value that has been estimated in [44]. The corresponding electron and ion heat conductivities are $\chi_{\perp e} = \chi_{\perp H} = \chi_{\perp z} = 10^{22}\ m^{-1}s^{-1}$. The duration of the stage 2 is taken to be equal to the characteristic energy quench time of $t_{EQ} = 0.2\ ms$ observed in experiments.

On the stage 3 starting at $t = 0.2\ ms$ (current quench), all transport coefficients are returned to their initial values of the stage 1. Experimentally, it is seen that the plasma sometimes partially recovers from the consequences of a disruption, pointing on the presence of confinement at this time.

7.2 Calculation results

The computed time evolutions of the profiles of the electron temperature, plasma current density and electron density are shown in Fig.38 and Fig.39.

After the injection of gas at $t = -0.5\ ms$ the edge electron temperature drops, mostly because of dilution by the cold electrons produced at the ionization, and a cold front moves towards the center with time (Fig.38 a). In $0.5\ ms$ the electron temperature drops over a half of the minor radius. The current density proportional to $T_e^{3/2}$ falls at the edge as well (Fig.38 b). However, the total plasma current can not decay on such a short time

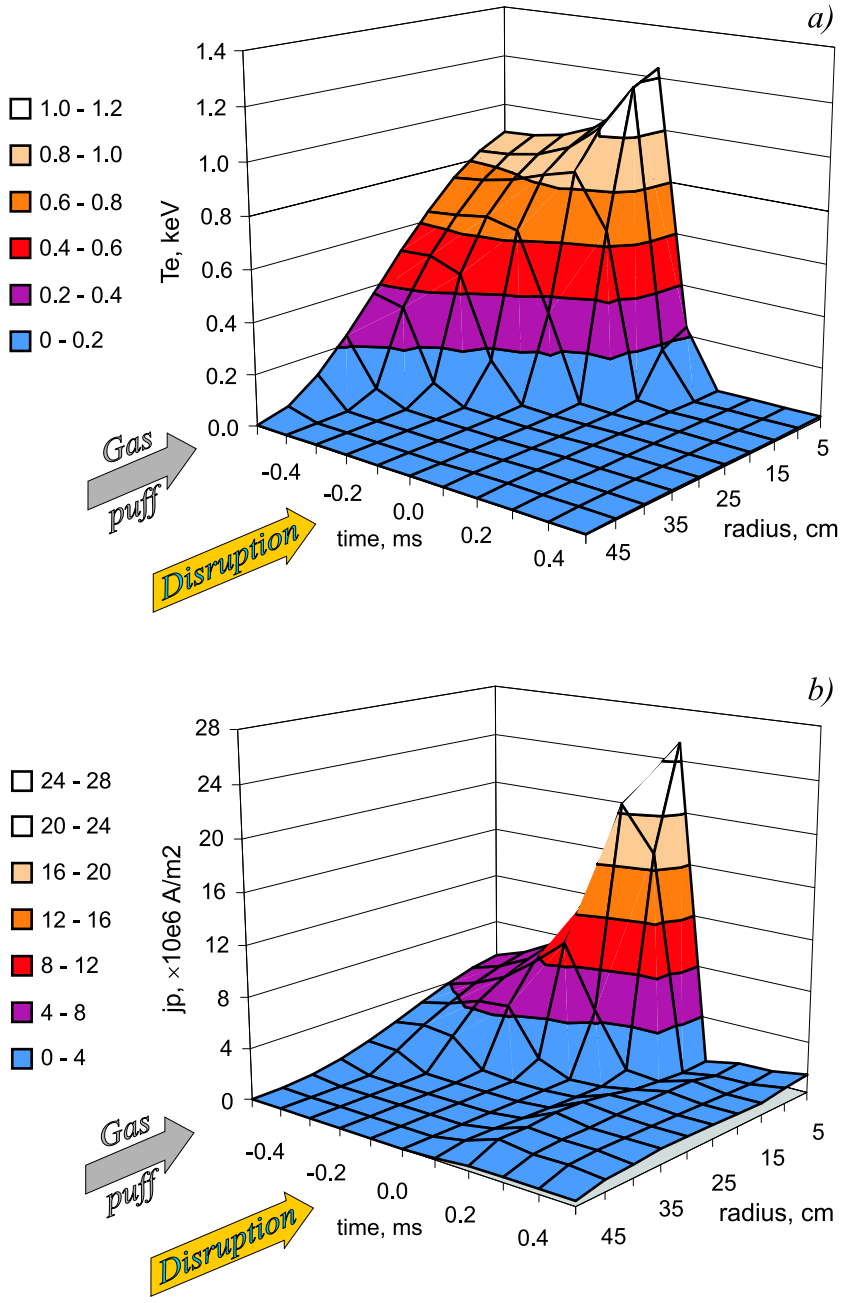

Figure 38: *Time evolution of the profiles of the electron temperature (a) and plasma current density (b) after the gas puff into the plasma at* $t = -0.5$ *ms.*

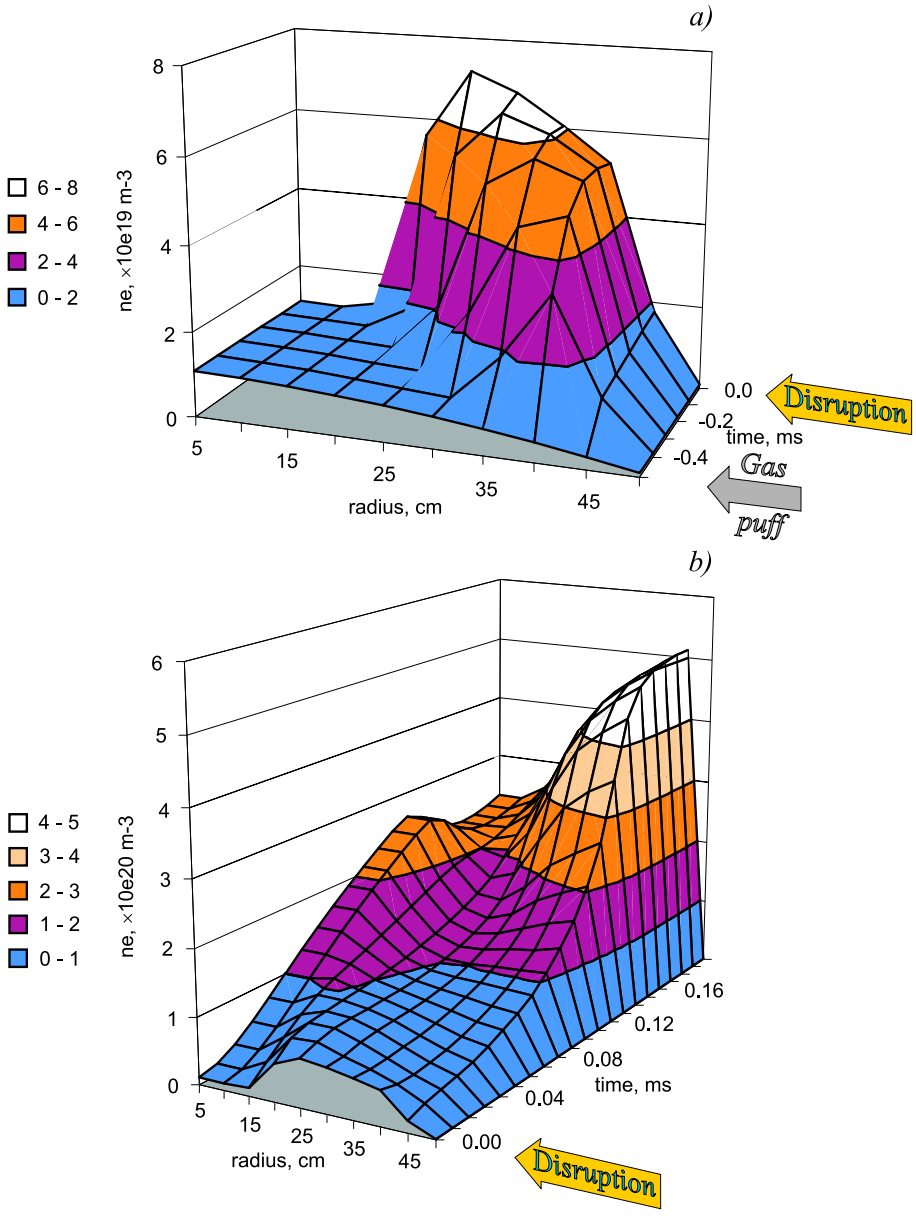

Figure 39: *Time evolution of the profile of the electron density after the gas puff: a) — before the disruption, b) — during the thermal quench phase with an extended time scale.*

scale. It leads to a peaking of the current density in the center and (in the framework of this model) to an increased ohmic heating at $r \approx 0$. If due to the deterioration of confinement the heat conduction of the real plasma rises yet prior to the energy quench, the growth of $T_e(0)$ should not be observed.

Fig.39 a) shows the evolution of the electron density profile from $t = -0.5\ ms$ up to $t = 0$. The front of the cloud of the injected neon cools the original plasma at the contact zone of the cloud and plasma, allowing the subsequent neon atoms to penetrate further. It is seen in Fig.39 a) that the electron density peak moves by $\approx 20\ cm$ in $0.4\ ms$ that is with the speed $\approx 500\ m/s$, which corresponds to the neon sound speed $c_s^{Ne} = 435\ m/s$.

After the onset of the disruption at $t = 0$, the thermal energy collapses rapidly. Fig.40 a) shows the central T_e plotted against time from the start of the disruption. The electron temperature drops in $\sim 0.1\ ms$ (Fig.40 a) corresponding to what is typically observed in tokamaks, for instance, in [53]. The existing peaked electron density profile at first flattens due to abnormally grown diffusivity, then an accumulation of the incoming electrons again takes place at the edge (Fig.39 b), with an enlarged time scale), because the gas puff still continues.

During the current quench starting at $t = 0.2\ ms$, the calculation shows that the central electron temperature stays nearly constant oscillating around $\approx 6\ eV$ (Fig.40 b) for reasons which will be discussed later. The same happens over the whole profile. At such a low T_e the plasma current dissipates quickly. A comparison between the I_p trace experimentally measured and the result of the calculation is displayed in Fig.40 c). During the current quench, an almost constant value of $T_e \approx 5 - 6\ eV$ results in a resistive decay time $\tau \approx 2\ ms$, which is too short compared to the experiment. As an example, an exponential curve with the time constant $\tau = 4\ ms$ is plotted in Fig.40 b). This curve reproduces the measured development of I_p better. This means, the calculated neon density in the plasma is too high. It is difficult to determine the density of neon neutrals on entering the plasma. Therefore, it may be reduced by assuming a larger vacuum volume between the vessel's wall and plasma edge, to which neon expands. A lower n_z should lead to a higher electron temperature of about $10\ eV$ and to a subsequent increase of the current decay time to $\tau = 4\ ms$ in agreement with the experiment. It is, however, clear from Fig.40 c) that the behaviour of the experimental I_p differs from an exponential one due to processes, which are not included in the model.

An example of a contour plot of the charge state densities of the injected neon (with $Z_{Ne} = 10$) is shown in Fig.41 a). The picture is taken at $t = 0.65\ ms$, at the end of the energy quench. In the calculation, the particle convective velocities are assumed to be $V_{\perp e}$ and $V_{\perp z} = 0$ (except for the neon neutrals which travel with sound speed). Only anomalous diffusion coefficients described above drive the particle transport. From Fig.41 a) it is seen that most of the neon atoms are moderately ionized up to $+1 - +2th$

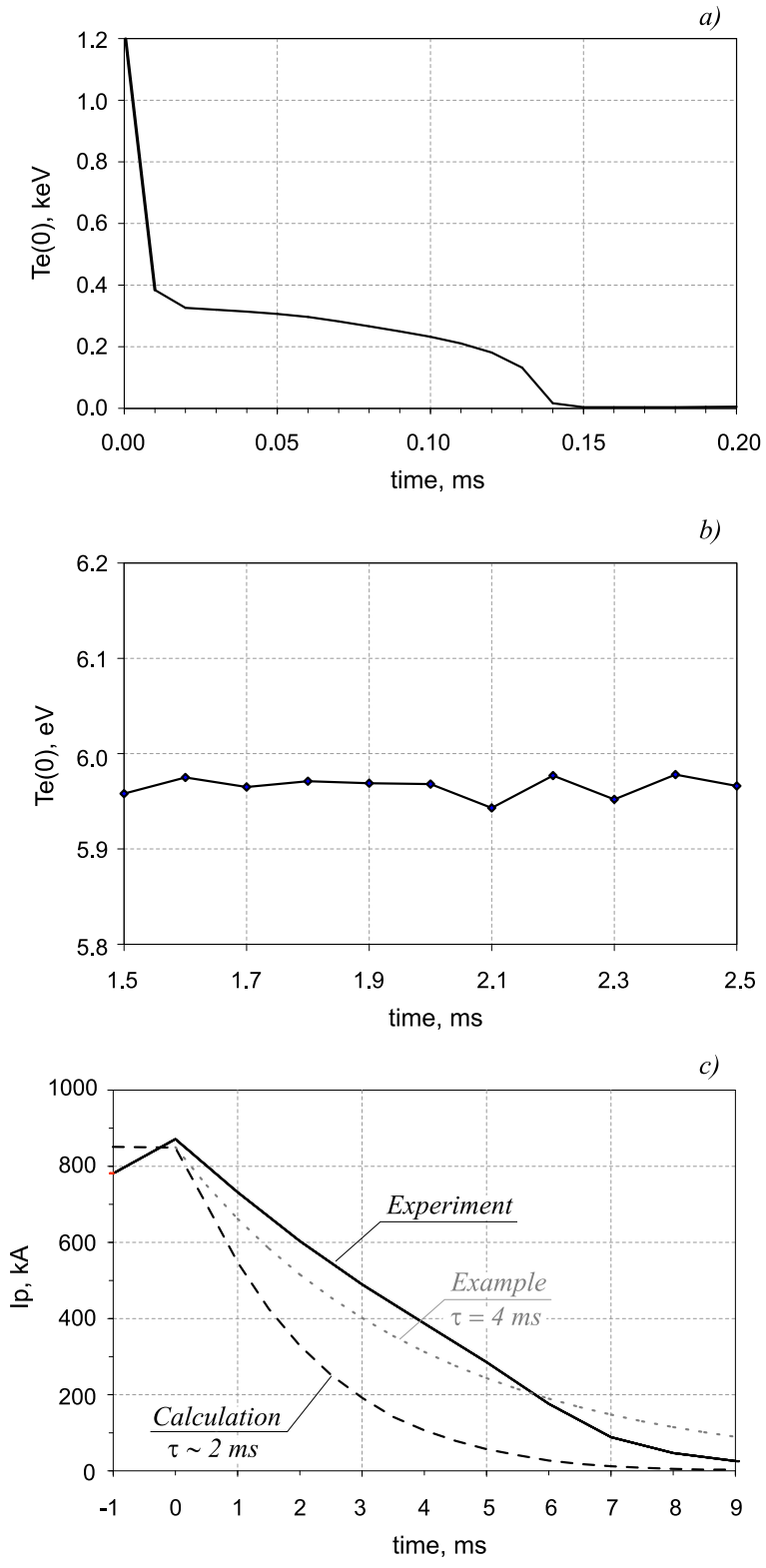

Figure 40: *a), b) — Behaviour of the central electron temperature during and after the thermal quench. c) — Comparison of the experimental plasma current decay (red line) with the modeling result (blue line) and a simple exponential dependence (grey line).*

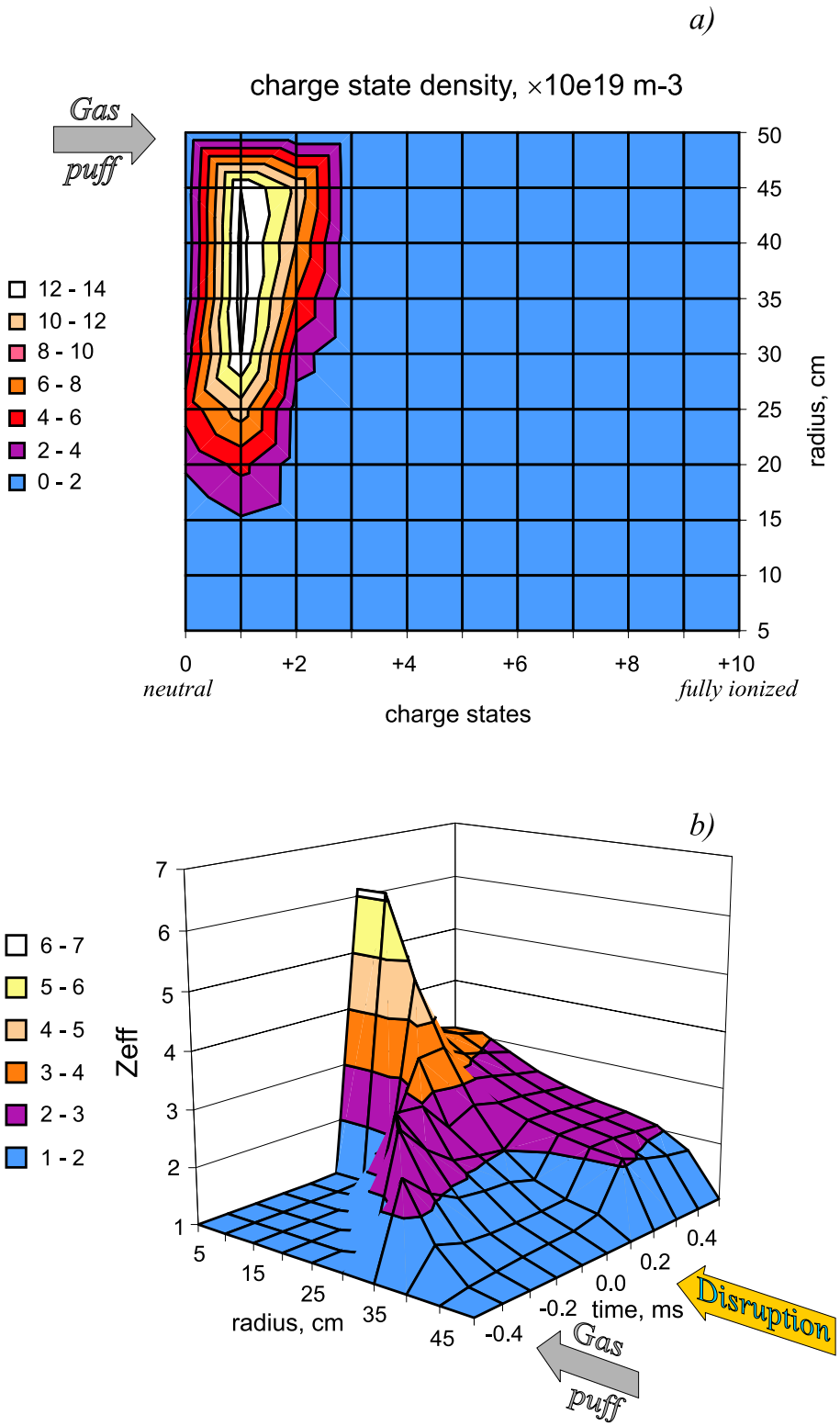

Figure 41: *a) — An example of a contour plot for the charge states of the injected neon at* $t = 0.14$ *ms. b) — Dynamics of the profile of the plasma* Z_{eff}.

charge state, as it should be at $T_e \approx 6\ eV$ after the energy quench. Radially the density of the neon ions is peaked close to the edge where the gas enters the plasma, but the unmagnetized neon atoms are able to penetrate substantially deeper due to the cooling of the plasma at the edge. The resulting dynamics of the plasma Z_{eff}-profile is given in Fig.41 b). The penetration of neon is well seen as a growing and moving peak of Z_{eff} at $t = -0.5 - 0.2\ ms$). After the fall of T_e the effective ion charge returns to modest values around 3.

7.3 Discussion

7.3.1 Role of the impurity line radiation in the central temperature collapse

The loss of the plasma thermal energy occurring on the time scale of some hundreds microseconds [53] is not yet completely understood. The results of the modeling performed here with neon injection may raise the meaning of impurity radiation for the explanation of the energy quench. It has been experimentally observed in [44] that the level of the impurity radiation, reached at a density limit disruption, accounts for the total pre-disruptive thermal energy contents of the plasma, and only a small part of it is conducted to the machine walls. Fig.42 a) reflects the growth of the radiation power (in W/m^3) during the energy quench. The radiation can locally amount to $\sim 0.8\ GW/m^3$. A plasma with $T_e = T_i = 1\ keV$ and $n_e = n_i = 10^{19}\ m^{-3}$ has the energy density $2nT \sim 10^3\ Pa$. In order to radiate this energy in the typical energy quench time of $\sim 0.1\ ms$, one would need the radiation power density of $P_{rad} = 0.01\ GW/m^3$. So, the radiation power obtained in the calculation may account for a substantial fraction of the initial stored plasma thermal energy despite the very short time of the energy quench.

To find out the contributions of the radiation and heat conduction in the drop of the central T_e, three calculation cases have been compared (Table 7). Case #1 represents

	D_e, D_z, m^2/s	χ_e, $m^{-1}s^{-1}$	*Duration of the energy quench, ms*
Case #1	100	10^{22}	0.14
Case #2	100	10^{20}	0.24
Case #3	1	10^{22}	no energy quench

Table 7: *Contributions of the radiation and heat conduction in the drop of the central T_e.*

the disruption scenario in which both the diffusion and the heat conduction are increased during the energy quench. In case #2, enhanced heat conduction is excluded by keeping it at the initial low value. Thus only radiation is present. In case #3, in contrast to case #2, the increased heat conduction is taken into account, and the radiation power

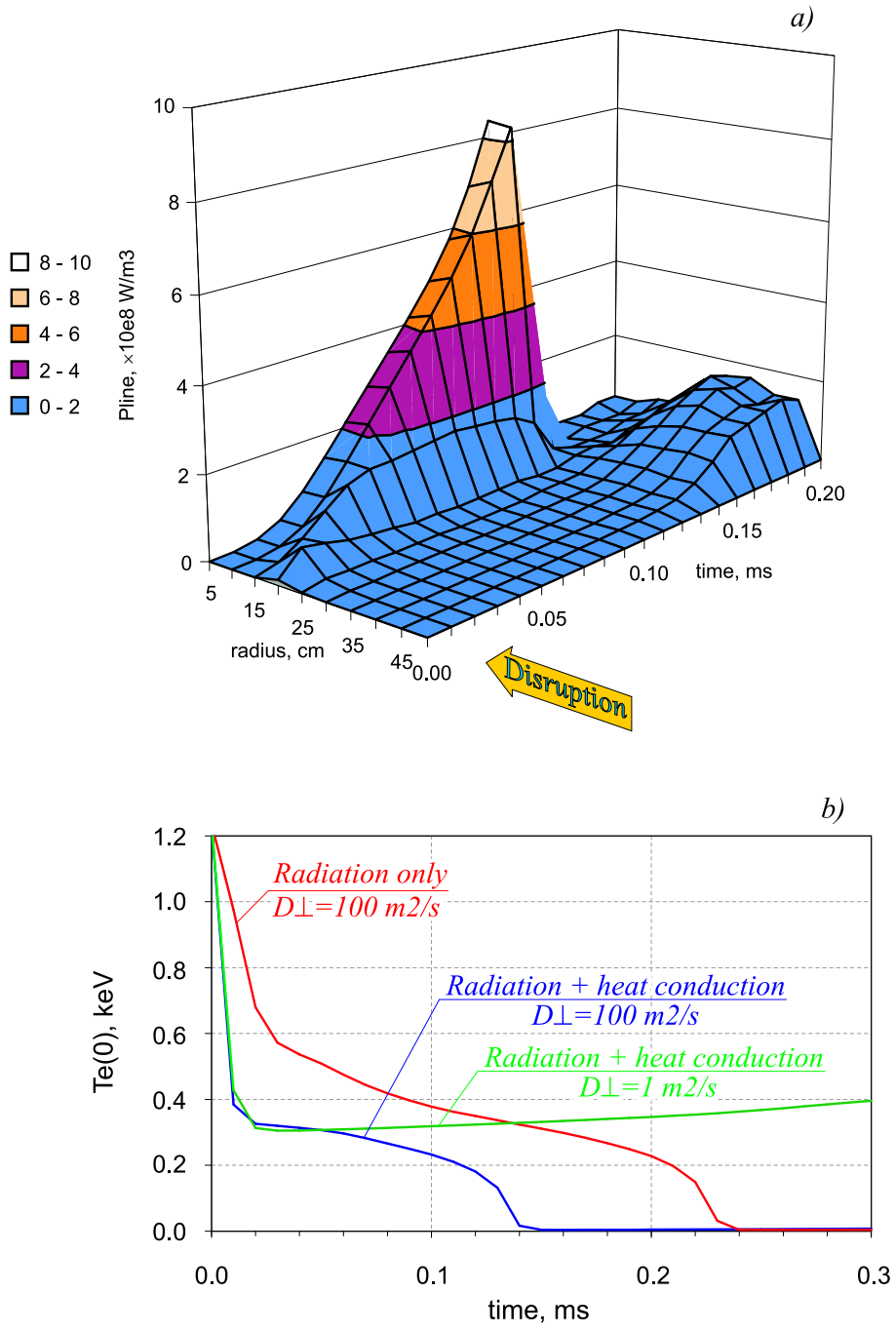

Figure 42: *a) — Power of the line impurity radiation through the energy quench. b) — Comparison between the contributions of heat conduction, line radiation and particle transport into the collapse of the central T_e. Blue line — both radiation and heat conduction are active, $D_\perp = 100\ m^2/s$; red line — heat conduction is neglected, $D_\perp = 100\ m^2/s$; green line — both radiation and heat conduction are active, $D_\perp = 1\ m^2/s$.*

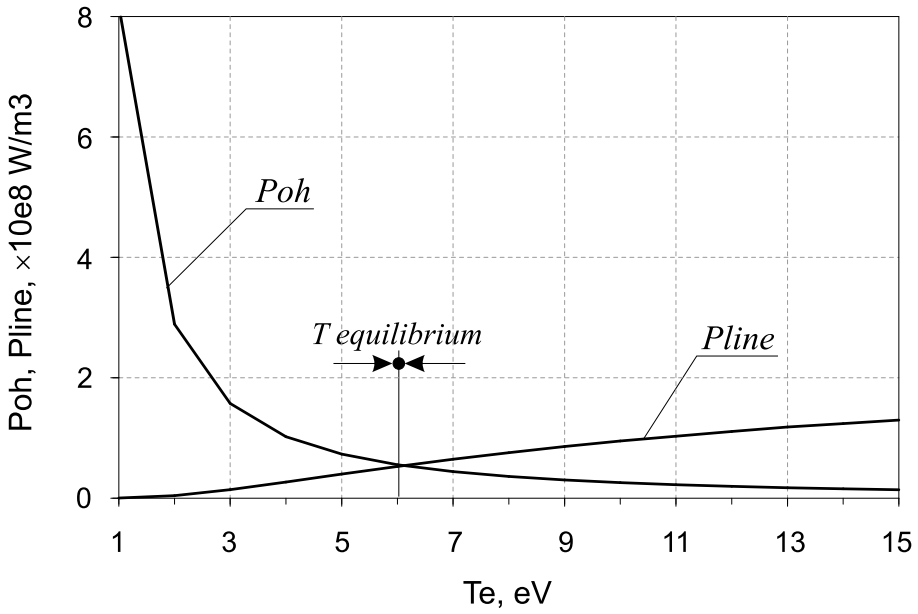

Figure 43: *A stable post-thermal quench temperature point, originating from a balance between the ohmic heating and radiative cooling.*

in the center is kept low by assuming a slow transport of the impurity. The comparison between the three cases is shown in Fig.42 b). The blue, red, and green lines correspond to case#1, case#2, case#3, respectively. In case #1, the temperature collapses quickly, at the beginning due to a sudden increase in the heat conductivity, and later — due to the increased radiation losses. In case #2, the energy quench lasts longer. However, its duration is still comparable with that observed in experiments. In case #3, the temperature has initially a behaviuor similar to case #1 owing to the enhanced heat transport, but remains at about 300 eV by the end of the energy quench. Therefore, our modeling predicts that the energy quench occurs only if impurity radiation is taken into account. However, the radiation power can explain the abrupt loss of the plasma thermal contents only if a rapid transport of the impurity towards the plasma center is assumed.

7.3.2 Appearance of a stable point in T_e after the energy quench

The calculation shows that after the energy quench the electron temperature stays approximately constant over the whole radial profile and is equal to several eV (Fig.40 b). This appears to reproduce the real post-thermal quench situation in a disruption, reported, for example, in [34] where T_e and Z_{eff} did not change throughout the current decay after helium injection.

The origin of the appearance of a constant temperature value is explained in Fig.43, where two dominant terms influencing the development of T_e are plotted. P_{oh} represents the dependence of ohmic heating on the temperature using Eq.32 with $Z_{eff} = 2.5$

(Fig.41 b). The cooling mechanism (P_{line}) is estimated taking into account only the Ne^{2+} and Ne^{3+} components (Ne^{2+} density is the highest at this time, but most of the radiation originates from Ne^{3+}). Other terms like P_{ion}, P_{br} and heat exchange between particles are ignored. It is clear from Fig.43 that the balance of the heating and cooling leads to $T_e \approx 6\ eV$. This is in agreement with Fig.40 b). The equilibrium is stable: an increase in T_e leads to an enhanced radiation and subsequent cooling; inversely, if T_e drops further, the ohmic term heats the plasma again, which has been already pointed out in [5, 11]. At later times of the current quench phase the plasma current decays, the ohmic heating power decreases and the equilibrium point in Fig.43 moves to zero.

7.3.3 Conclusions for the interpretation of disruptions without external gas injection

The modeling shows that the radiation losses play an important role both in the energy and current quench phases of a disruption. The initial drop in the energy quench phase can be explained by increased heat conduction. However, without radiation the temperature fall would stop at about 300 eV.

Experimentally, always a strong correlation between the energy quench and impurity radiation is observed [44, 54]. The enhancement of the impurity release starts at a low level with the growth of internal modes and increases suddenly by orders of magnitude during the energy quench. The times of both the energy quench onset and the impurity release enhancement are so close that it is presently impossible to distinguish between the cause and the consequence.

In our view, a disruption without external gas injection develops as follows. The growing modes indicate that the plasma becomes MHD unstable. After the beginning of the energy quench, the confinement breaks down with a time scale of the Alfvén transit time, which is the fastest time scale in the plasma. The collapsing internal energy is conducted to the wall and releases a large amount of impurities, e.g. by sputtering. The impurities must posses an initial energy of few eV to explain their fast progression towards the plasma core. Their radial velocity should be of the order of $10^4\ m/s$. The fast radial penetration can be explained only by a very high value of the diffusion coefficient (as assumed in our model), or by convection. Within 0.1 ms the impurities reach their full radiation power such that they can reduce the plasma temperature rapidly, consistent with the observations.

During the current quench phase, the impurity radiation determines the power balance and the duration of the current decay. Therefore, the current decay time differs substantially from a disruption to a disruption, depending, probably, on the amount and kind of the impurities released. In disruptions with gas injection the amount of impurities

is rather high and therefore the current quench phase is short.

On JET, an injection of a moderate amount of helium into an elongated plasma extended the current decay time ($\Delta\tau_I \approx 100\ ms$) as compared to a normal disruption ($\Delta\tau_I \approx 20\ ms$)[28]. In this case the intense release of the wall impurities in the energy quench is not supposed to occur. The dissipation of the plasma current is then determined by the radiative cooling of the plasma by helium which is lower than that of the wall impurities (basically, carbon and oxygen). This leads to the longer plasma current decay observed.

8 SUMMARY AND CONCLUSIONS

From the work, several conclusions can be drawn:

- A fast valve with a high gas throughput has been developed. To our knowledge, it is the valve with the fastest reaction time available. The time from a trigger signal to the start of the valve opening is 0.5 ms, and to the fully open state 1 ms. In contrast to valves used in other experiments, this new design contains no ferromagnetic materials. Therefore, it is not affected by the strong tokamak magnetic field and can be mounted directly at the vacuum vessel. It can operate at working gas pressures of $0 - 30$ bar and its gas capacity can be varied between $0 - 250$ cm^3, resulting in an injection of up to $1.9 \cdot 10^{23}$ particles. The valve has been taken into operation, calibrated and tested. No special exit nozzle is required and the particles are injected into a tokamak vacuum chamber at sound velocity.

- The first experiments on mitigation of disruptions by a gas injection on the the ASDEX Upgrade tokamak have been carried out. In constrast to the experiments on DIII-D, a low pressure ($\sim$ 1 bar) gas injection has been performed, what is limited by a tolerable increase of the pressure inside the vacuum vessel.

- An injection of an amount of impurity atoms comparable to that of the target plasma has been shown to reduce the duration of the plasma current decay in ASDEX Upgrade, if a VDE is absent. The reduction from ~ 100 ms in a natural disruption down to ~ 10 ms in disruptions after a gas puff was observed. The degree of the reduction depends on the kind of injected gas and its amount. The effect can be used for terminating a discharge quickly to avoid the dangerous consequences of an uncontrolled disruption.

- The induction of halo currents and the subsequent mechanical loads of the ASDEX Upgrade vacuum vessel has been mitigated by a pre-emptive low pressure gas injection by a factor of 4. The choice of the kind and amount of killer gas presents a freedom to find a compromise between an acceptable increase of the in-vessel pressure and a strength of mitigation desired. In ASDEX Upgrade ($V = 14$ m^3), optimal characteristics of a killer gas puff have been found to be an injection of 120 $mbar \cdot l$ of neon, which is suggested for disruption mitigation [42] on a regular basis.

- A numerical model has been developed to simulate the process of a large gas injection into a plasma and to describe the subsequent energy and current quenches. Compared to previous models, both particle and energy transport are treated in a

one-dimensional case. The modeling shows that line radiation of the injected impurity plays a substantial role in quenching the plasma's thermal energy. For this, a rapid transport of the impurity of the order of $D_\perp \approx 100\ m^2/s$ towards the plasma core has to be assumed. An appearance of a stable post-thermal quench temperature of several eV over the whole poloidal cross-section is shown numerically.

– The model shows the importance of the impurity radiation for naturally developing disruptions. With the outward heat conduction as the only sink mechanism, the electron temperature remains at around 300 eV at the end of the energy quench, in contradiction to the observations.

Future plans will concern the following points:

– Recently the installation of the valve on TEXTOR has been finished and its operation has been checked. The future work will include building a mitigation system on TEXTOR. The experimental results obtained on ASDEX Upgrade in circular plasmas will be verified. In addition, questions of an in-out symmetry of heat fluxes during the energy quench measured by two infrared cameras and of a possible reduction of a wall impurities contents after the energy quench will be addressed.

– An interest has been shown from JET for the valve in order to construct a disruption mitigation system.

– A verification and further development of the disruption model will be performed. The deviation of the calculated plasma current behaviour from the measured one must be corrected by implementing a more precise equation of the current decay. Computations with gases other than neon, having different radiation properties, will provide further investigation of disruptions because of a killer gas injection (helium, argon, krypton,...) and the natural density limit (carbon, oxygen).

9 ACKNOWLEDGEMENTS

I would like to thank my tutor Prof.U.Samm and the director of the institute Prof.R.Wolf for their support and continuous help during the PhD studies.

I express gratitude to my scientific supervisor Dr.K.H.Finken for his constant support and valuable pieces of advice throughout the work and at the stage of preparing the thesis. His help I appreciate a lot.

I would like to thank Prof.Kaufmann, Dr.O.Gruber, Dr.G.Pautasso and the ASDEX Upgrade team for their hospitality and help. I am particularly thankful to Dr.Pautasso for the aid in carrying out the experiments, getting the data and their interpretation. For the great technical assistance and much attention I express my sincere gratitude to P.Cierpka and M.Beck, also from IPP Garching.

I appreciate the help of my colleagues in IPP Jülich:
– Dr.D.Reiser and Dr.M.Tokar — for the fruitful discussions of the model and numeric solution method,
– Dr.M.Tokar — for providing me with the data on radiation rates of impurities,
– Mr.O.Marchuk — for providing me with the atomic data.

I sincerely thank Mr.A.Hiller and P.Cornette for many explanations, pieces of advice and collaboration work during the tests and calibration of the fast gas valve in the lab of IPP Jülich and later at the installation on TEXTOR.

I would like to thank Dr.G.Mank for the invitation me to IPP Jülich, suggestion of the topic of research and much attention at the initial stage of the work.

Last but not least I thank my wife Elena for much patience that she had during my work on these thesis.

References

[1] J.Raeder, L.Lengyel, F.Leuterer. *"Controlled nuclear fusion: fundamentals of its utilization for energy supply"*, John Wiley and Sons, New Jork, 1986.

[2] J.Wesson. *"Tokamaks"*. Clarendon Press, Oxford, 1987.

[3] J.Ongena, G.Van Oost. *Transactions of Fusion Technology* **37** (2000), p.3.

[4] L.A.Artsimovich. *Nucl.Fusion* **12** (1972), p.215.

[5] J.A.Wesson, R.D.Gill, M.Hugon, F.C.Schüller, J.A.Snipes, D.J.Ward, D.V.Bartlett, D.J.Campbell, P.A.Duperrex, A.W.Edwards, R.S.Granetz, N.A.O.Gottardi, T.C.Hender, E.Lazzaro, P.J.Lomas, N.Lopes Cardozo, K.F.Mast, M.F.F.Nave, N.A.Salmon, P.Smeulders, P.R.Thomas, B.J.D.Tubbing, M.F.Turner, A.Weller. *Nucl.Fusion* **29** (1989), p.641.

[6] G.Federici, C.H.Skinner, J.N.Brooks, J.P.Coad, C.Grisolia, A.A.Haasz, A.Hassanein, V.Philipps, C.S.Pitcher, J.Roth, W.R.Wampler, D.G.Whyte. *Nucl. Fusion* **41** (2001), p.1967.

[7] ITER Physics Basis. *Nucl.Fusion* **39** (1999), p.2137.

[8] P.B.Parks, M.N.Rosenbluth, and S.V.Putvinski. *Phys.Plasmas* **6** (1999), p.2523.

[9] A.Savtchkov, K.H.Finken, G.Mank. *Rev.Sci.Instrum.* **73** (2002), p.3490.

[10] A.Savtchkov, G.Pautasso, K.H.Finken, G.Mank. *Proceedings of the 29th European Conference on Plasma Phys. and Contr.Fusion* (2002) Vol.26B, P – 3.203.

[11] M.Bakhtiari, R.Yoshino, Y.Nishida. *Fusion Sci.Technology* **41** (2002), p.77.

[12] B.V.Kuteev, V.Yu.Sergeev, S.Sudo. *Nucl.Fusion* **35** (1995), p.1167.

[13] D.G.Whyte, T.E.Evans, A.G.Kelmann, D.A.Humphreys, A.W.Hyatt, T.C.Jernigan, R.L.Lee, S.L.Luckhardt, P.B.Parks, M.J.Schaffer and P.L.Taylor. *Proceedings of the 24th European Conference on Controlled Fusion and Plasma Physics, Berchtesgaden* (1997) Vol.21A, p. 1137.

[14] *http://w3.pppl.gov/ pletzer/programs/fortran-c-c++/pest3_suite/matlab/matlab.html*

[15] R.Dendy. *Plasma physics: an introductory course.* Cambridge University Press, Cambridge, 1993.

[16] Y.Nakamura, G.Pautasso, O.Gruber and S.C.Jardin. *Plasma Phys.Control.Fusion* **44** (2002), p.1471.

[17] F.C.Schüller. *Plasma Phys.Control.Fusion* **37** (1995), p.A135.

[18] P.L.Taylor, A.G.Kelmann, B.W.Rice, and D.A.Humphreys. *Phys.Rev.Letters* **76** (1996), p.916.

[19] P.Helander, L.-G.Eriksson and F.Andersson. *Plasma Phys.Control.Fusion* **44** (2002), p.B247.

[20] S.Putvinski, P.Barabaschi, N.Fujisawa, N.Putvinskaya, M.N.Rosenbluth and J.Wesley. *Plasma Phys.Control.Fusion* **39** (1997), p.B157.

[21] G.Pautasso, K.Büchl, J.C.Fuchs, O.Gruber, A.Hermann, K.Lackner, P.T.Lang, K.F.Mast, M.Ulrich, H.Zohm, ASDEX Upgrade team. *Nucl.Fusion* **30** (1996), p.1291.

[22] T.E.Evans, A.G.Kelmann, D.A.Humphreys, M.J.Schaffer, P.L.Taylor, D.G.Whyte, T.C.Jernigan, A.W.Hyatt, R.L.Lee. *J.Nucl.Mater.* **241 – 243** (1997) p.606.

[23] G.L.Schmidt, S.Ali-Arshad, D.Bartlett, A.Chankin, S.Clement, M.Gadeberg, P.Kuoschus, D.O'Brien, R.Reichle, G.Sadler, A.Tanga. *Proceedings of the 22th European Conference on Controlled Fusion and Plasma Physics* (1995) Vol.19C, p.IV-021

[24] R.Yoshino, T.Kondoh, Y. Neyatany, K.Itami, Y.Kawano, N.Isei. *Plasma Phys.Control.Fusion* **39** (1997), p.313.

[25] V.M.Timokhin, V.Yu.Sergeev, B.V.Kuteev. *Plasma Phys.Rep.* **27** (2001), p.181.

[26] D.G.Whyte, T.C.Jernigan, D.A.Humphreys, A.W.Hyatt, C.J.Lasnier, P.B.Parks, T.E.Evans, M.N.Rosenbluth, P.L.Taylor, A.G.Kelmann, D.S.Gray, M.E.Hollmann, S.K.Combs. *Phys.Rev.Letters* **89** (2002), p.055001-1.

[27] D.G.Whyte, T.C.Jernigan, D.A.Humphreys, A.W.Hyatt, C.J.Lasnier, P.B.Parks, T.E.Evans, P.L.Taylor, A.G.Kelmann, D.S.Gray, E.M.Hollmann. *19th IAEA Fus.Energy Conf.* (2002) IAEA-EX/S2-4.

[28] V.Riccardo, P.Andrew, L.C.Ingesson, G.Maddaluno. *Plasma Phys.Contr.Fusion* **44** (2002), p.905.

[29] M.Bakhtiari, Y.Kawano, H.Tamai, Y.Miura, R.Yoshino and Y.Nishida. *Nucl.Fusion* **42** (2002), p.1197.

[30] M.N.Rosenbluth, S.V.Putvinskij, P.B.Parks. *Nucl.Fusion* **37** (1997), p.955.

[31] P.B.Parks, M.N.Rosenbluth, S.V.Putvinski, T.E.Evans. *Fusion Science and Technology* **35** (1999), p.267.

[32] P.L.Taylor, A.G.Kelmann, T.E.Evans, D.S.Gray, D.A.Humphreys, A.W.Hyatt, T.C.Jernigan, R.L.Lee, J.A.Leuer, S.C.Luckhardt, P.B.Parks, M.J.Schaffer, D.G.Whyte, and J.Zhang. *Phys.Plasmas* **6** (1999), p.1872.

[33] R.A.Hulse. *Nucl.Technology/Fusion* **3** (1983), p.259.

[34] D.A.Humphreys, D.G.Whyte. *Phys.Plasmas* **7** (2000), p.4057.

[35] D.Marescaux, Rev.Sci.Instrum.65, 2414 (1994)

[36] J.Kriesel, R.Prohaska and A. Fisher, Rev.Sci.Instrum. **62** (1991), 2372

[37] J.C.Thomas, D.Q.Hwang, R.D.Horton, J.H.Rogers and R.Raman. Rev.Sci.Instrum. **64** (1993), 1410.

[38] G.Pautasso, K.Bühl, J.C.Fuchs, O.Gruber, A.Hermann, K.Lackner, P.T.Lang, K.F.Mast, M.Ulrich, H.Zohm, ASDEX Upgrade team. Nucl.Fusion **36** (1996) 1291.

[39] G.Pautasso, C.Tichmann, S.Egorov, T.Zehetbauer, O.Gruber, M.Maraschek, K.F.Mast, V.Mertens, I.Perchermeier, G.Raupp, W.Treutterer, C.G.Windsor, ASDEX Upgrade team. Nucl.Fusion **42** (2002), 100.

[40] J.A.Wesson, D.J.Ward, M.N.Rosenbluth. Nucl.Fusion **30** (1990) 1011.

[41] G.Pautasso, S.Egorov, K.H.Finken, O.Gruber, A.Hermann, C.J.Fuchs, M.Maraschek, R.Neu, Y.Nakamura, V.Rohde, A.Savtchkov, U.Seidl, B.Streibl, Ch.Tichmann and the ASDEX Upgrade team. *19th IAEA Fus.Phys.Conf.* (2002) IAEA-EX/P4-14.

[42] G.Pautasso, A.Savtchkov, S.Egorov, R.Dux, K.H.Finken, O.Gruber, G.Haas, G.Mank, M.Maraschek, V.Rohde, U.Seidl, and the ASDEX Upgrade team. *Proceedings of the 29th European Conference on Plasma Phys. and Contr.Fusion* (2002) Vol.26B, P – 2.051.

[43] D.E.Post, R.V.Jensen, C.B.Tarter, W.H.Grasberger, W.A.Lokke. *Atomic Data and Nuclear Data Tables* **20** (1997), p.397.

[44] E.M.Hollmann, D.S.Gray, D.G.Whyte, A.Yu.Pigarov, S.I.Krasheninnikov, and J.A.Boedo. *Phys.Plasmas* **10** (2003), p.2863.

[45] D.J.Ward, J.A.Wesson. Nucl.Fusion **32** (1992) 1117.

[46] *http://adas.phys.strath.ac.uk/*

[47] M.Z.Tokar'. *Berichte des Forschungszentrums Jülich* **2588** (1992).

[48] *http://physics.nist.gov/cgi-bin/AtData/main_asd*

[49] *http://www.ap.univie.ac.at/users/ves/cp0102/dx/node86.html*

[50] *http://www.ap.univie.ac.at/users/ves/cp0102/dx/node23.html*

[51] D.Kalupin, M.Z.Tokar, P.Dumortier, A.Messiaen, D.Reiser, S.Soldatov, B.Unterberg, G.van Wassenhove and R.Weynants. *Plasma Phys.Contr.Fusion* **43** (2001), p.945.

[52] M.Z.Tokar, H.Nordmann, J.Weiland, J.Ongena, V.Parail, B.Unterberg and contributors to the EFDA-JET Workprogramme. *Plasma Phys.Contr.Fusion* **44** (2002), p.1903.

[53] F.Salzedas, S.Hokin, F.C.Schuüller, A.A.M.Oomens, and the RTP Team. *Phys.Plasmas* **9** (2002), p.3402.

[54] A.W.Hyatt, R.L.Lee, J.W.Cuthberston, D.A.Humphreys, A.G.Kellman, C.J.Lasnier, P.L.Taylor, and the DIII-D team. *Proceedings of the 23th European Conference on Plasma Phys. and Contr.Fusion* (1996) Vol.20C, a094.

Forschungszentrum Jülich
in der Helmholtz-Gemeinschaft

Jül-4122
März 2004
ISSN 0944-2952